People's Democratic Republic of Algeria
Ministry of Higher Education and Scientific Research
Ferhat Abbas University-Sétif1
Faculty of Science
Department of Physics

Thesis presented to obtain:

DOCTORAT EN SCIENCES

In Physics

Option: Medical Physics

Title:

Development of a technique based on multivariate statistical method to enhance scanning time and lesion detectability in dynamic PET

Presented and defended by **Mr. BEZOUBIRI Fethi**

29/06/2024

In front of the jury composed of:

Prof. Belkhiat Djamel Eddine Chouaib	**Sétif 1 University**	**President**
Prof. Kharfi Fayçal	**Sétif1 University**	**Thesis Director**
Dr. Zidi Tahar	**Atomic Energy Commission COMENA**	**Thesis co-Director**
Prof. Bouchareb Yassine	**Sultan Qaboos University**	**Examiner**
Prof. Azizi Hacene	**Sétif 1 University**	**Examiner**
Dr. Ounoughi Nabil (MCA)	**Jijel University**	**Examiner**

To my beloved parents, whose encouragement is the source of my success.

To my wonderful wife, Asma. You are more than a wife.

To my beloved sons: Mohamed Ali, Samy Acil, and Riyad Hatem. Source of my happiness.

I dedicate this thesis.

Acknowledgments

The quest for knowledge is an enduring and challenging journey. It demands effort, commitment, perseverance, and significant resilience. The challenges I faced before and during the thesis period would not have been overcome without the support and encouragement of those to whom I owe immense gratitude.

First and foremost, I would like to express my deepest appreciation to my Thesis Directors, Mr. Kharfi Fayçal, Professor at Sétif1 University, and Mr. Zidi Tahar, Senior Researcher and General Secretary of Algeria Atomic Energy Commission **(**COMENA), who allowed me to carry out this thesis work under their supervision. I express my great and heartfelt gratitude to them for their support, encouragement, and trust, which have enabled me to complete this project successfully.

I would also like to extend my deepest gratitude to those who agreed to be on the jury of this thesis: Mr. Belkhiat Djamel Eddine Chouaib, Professor at Sétif 1 University, for accepting to chair the jury and the board of examiners; Mr. Azizi Hacene, Professor at Sétif 1 University; Mr. Ounoughi Nabil, Professor at Jijel University; and Mr. Bouchareb Yassine Professor at Sultan Qaboos University, for devoting their valuable time to depth reading and examining this manuscript. I would like to deeply thank them.

I am extremely grateful to Prof. Bouchareb Yassine for his encouragement, comments, and guidance about how to write good scientific papers.

I am also grateful to Ms. Houria SALAH, Senior Expert Researcher at CRNA, for her scientific and moral support. Thank you so much Houria.

This work was carried out at the Algiers Nuclear Research Center (CRNA). I would like to express my sincere thanks to the General Director for the material support provided to me during this thesis period.

I do thank my best friends, Dr. Betka Abderrahim and Mr. Ben Ali Moussa Khaled, for their moral support. Thank you, Abderrahim, for meeting me with the good man, Prof. Kharfi Fayçal. Without you, Khaled, the road from Algiers to Sétif is truly long!

To my colleague, wife, and partner, I express my great and heartfelt gratitude for her continued support. I cannot estimate your valuable help during this period. Our adventures are now

finished! Thanks to God who helped us to achieve our goals and put in our way a good people. Iron women, you are Asma.

My great and heartfelt gratitude is also expressed to my beloved parents for their support, encouragement, and prayer. Thank you for being wonderful.

Finally, I thank my beloved sons, Mohamed Ali, Samy Acil, and Riad Hatem for their patience. You are my priority forever. I love you all dearly.

Algiers, 28th of December, 2023

Table of Contents

CHAPITRE II

SIMULATION OF DYNAMIC ^{18}F-FDG PET IMAGES

CHAPITRE III

ENHANCEMENT OF LESION DETECTABILITY AND OPTIMIZATION OF SCANNING TIME

Figures

CHAPITRE I

CHAPITRE II

CHAPITRE III:

Tables

CHAPITRE I

CHAPITRE II

Abbreviation list

PET: **P**ositron **E**mission **T**omography.

dPET: **d**ynamic **PET**.

^{18}F-FDG: **F**luoro**D**eoxy**G**lucose with the positron-emitting radionuclide **F**luorine-**18**

SUV: **S**tandardized **U**ptake **V**alue.

IF: **I**nput **F**unction.

PCA: **P**rincipal **C**omponent **A**nalysis.

PCs: **P**rincipal **C**omponent axi**s**.

PCIs: **P**rincipal **C**omponent **I**mage**s**.

SUM: **SUM**med images.

TBR: **T**umor to **B**ackground **R**atio.

ALPs: **A**ctivity **L**ines **P**rofile**s**.

CT: **C**omputed **T**omography.

μ**PET**: micro**PET**.

LOR: **L**ine **O**f **R**esponse.

SPECT: **S**ingle **P**hoton **E**mission **C**omputed **T**omography.

STIR: **S**oftware **T**omographic **I**mage **R**econstruction.

NURBS: **N**on-**U**niform **R**ational **B**asis **S**plines.

MIRD: **M**edical **I**nternal **R**adiation **D**ose.

4D-XCAT: **4D** e**X**tended **CA**rdiac-**T**orso.

NCAT: **N**URBS-based **CA**rdiac-**T**orso.

MCAT: **M**athematical **CA**rdiac-**T**orso.

MOBY: **MO**use whole **B**od**Y**.

ROBY: **R**at wh**O**le **B**od**Y**.

SVD: **S**ingular **V**alue **D**ecomposition.

EVD: **E**igen**V**alue **D**ecomposition.

MRI: **M**agnetic **R**esonance **I**maging.

TAC's: **T**ime **A**ctivity **C**urves.

OSMAPOSL: **O**rdered **S**ubsets-**M**aximum **A** posteriori **P**robability-**O**ne **S**tep **L**ate.

FOV: **F**ield **O**f **V**iew.

Abstract

Dynamic PET imaging plays a key role in improving cancer diagnosis, assessing therapy response, and characterizing tumor lesions. However, dynamic PET suffers from several limitations such as noisy images and longer data acquisition time. This study aimed to enhance lesion detectability in ^{18}F-FDG PET images and shorten the total duration of the ^{18}F-FDG study using principal component analysis (PCA), while preserving the detectability of lesions. For this purpose, activity maps were generated using the 4D-XCAT anthropomorphic phantom combined with time activity curves calculated using a standard ^{18}F-FDG 3-compartment model. A 9 mm spherical liver lesion was inserted into the 4D-XACT phantom. The widely used STIR image reconstruction software was used to generate dynamic ^{18}F-FDG PET images. The PCA method was applied to the simulated dynamic ^{18}F-FDG-PET images generated at different scanning times (0-11, 0-13, 0-15, 0-20, 0-25, 0-35, 0-40, 0-45, 0-50, and 0-55 min) and at T=35-55 min. The estimated Principal Component Images (PCIs) were visually assessed and compared to the SUMmed images generated at T=35-55 min. The Tumor-to-Background Ratio (TBR) and Activity Profiles Line (APLs) were considered in the quantitative assessment. For lesion detectability, the comparison between the 3 PCIs (PCI1, PCI2 and PCI3) and SUM images showed that PCI2 could provide superior lesion detectability compared to the SUM images at T-35-55. Concerning the time acquisition reduction, the visual assessment of the 3 estimated PCIs and SUM images showed that PCI3 has better detectability of the lesion regardless of the scanning time. PCI2 showed good lesion detectability at all timing expect at 11 and 13 min, whereas PCI1 showed lower lesion detectability at all times. Quantitatively, the TBR estimated on PCI3 was similar to that on the SUM images (TBR on PCI3 was 2.49±0.72 and 3.08±0.49 on the SUM images) but higher than that on PCI1 and PCI2 from timing 11 to 35 min. The TBR on PCI1 decreased with the increase in scanning time. On PCI2, the TBR increased with scanning time (maximum of 3.87±1.11 at 55 min).

The findings of this study suggest the use of the PCI3 at 20 and 25 min to resuce the scanning time in dynamic ^{18}F-FDG PET. This study demonstrated that PCA allows enhancement lesion detectability and reduction of scanning time in dynamic ^{18}F-FDG-PET imaging, hence increasing patient comfort and minimizing motion effects.

Keywords:

Dynamic ^{18}F FDG PET images, detectability, reduction of scan time, PCA, STIR software, 4D-XCAT phantom.

Résumé

L'imagerie TEP dynamique joue un rôle clé dans l'amélioration du diagnostic du cancer, l'évaluation de la réponse thérapeutique et la caractérisation des lésions tumorales. Cependant, elle souffre de plusieurs limitations telles que des images bruitées et un temps d'acquisition de données long. Cette étude visait à améliorer la détectabilité des lésions dans les images TEP au ^{18}F-FDG et à réduire la durée totale de l'étude au ^{18}F-FDG en utilisant la méthode d'analyse en composantes principales (ACP), tout en préservant la détectabilité des lésions. Pour cela, les cartes d'activité ont été générées à l'aide du fantôme anthropomorphe 4D-XCAT combiné à des courbes d'activité temporelle calculées à l'aide d'un modèle standard à 3 compartiments ^{18}F-FDG. Une lésion hépatique sphérique de 9 mm a été insérée dans le fantôme 4D-XACT. Le logiciel de reconstruction d'images STIR a été utilisé pour générer des images TEP dynamiques au ^{18}F-FDG. La méthode ACP a été appliquée aux images ^{18}F-FDG-PET dynamiques simulées générées à différents temps de numérisation (0-11, 0-13, 0-15, 0-20, 0-25, 0-35, 0-40, 0 -45, 0-50 et 0-55 min), et à T=35-55 min. Les images en composantes principales (PCI) estimées ont été évaluées visuellement et comparées aux images SUMmed, générées à T = 35-55 min. Le rapport tumeur/fond (TBR) et les profils de d'activité (ALP) ont été pris en compte dans l'évaluation quantitative. Pour la détectabilité des lésions, la comparaison entre les images de 3 PCI et SUM montre que PCI2 pourrait fournir une détectabilité des lésions supérieure à celle des images SUM, à T-35-55. Concernant la réduction du temps d'acquisition, l'évaluation visuelle des 3 images PCI et SUM estimées montre que PCI3 a une meilleure détectabilité de la lésion tumorale quel que soit le temps de numérisation. PCI2 montre une bonne détectabilité des lésions à tous les moments, sauf à 11 et 13 minutes, tandis que PCI1 montre une détectabilité des lésions plus faible à tout moment. Quantitativement, le TBR estimé sur PCI3 est similaire aux ceux calculés dans les images SUM (TBR sur PCI3 est de 2,49 ± 0,72 et 3,08 ± 0,49 sur les images SUM) mais supérieur à celui calculé sur PCI1 et PCI2 du timing 11 à 35 min. Le TBR obtenu sur PCI1 diminue avec l'augmentation du temps de scan. Sur PCI2, le TBR augmente avec le temps de scan (maximum de 3,87 ± 1,11 à 55 minutes).

Les résultats obtenus dans cette étude suggèrent l'utilisation de PCI3 à 20 ou 25 minutes pour optimiser/réduire le temps de scan dans la TEP dynamique au ^{18}F-FDG. Cette étude montre que l'ACP pourrait améliorer la détectabilité des lésions et de réduire le temps de scan en imagerie dynamique ^{18}F-FDG PET, ce qui pourrait augmenter le confort du patient et minimiser les effets du mouvement.

Mots clés:

Images ^{18}F-FDG TEP dynamiques, détectabilité, optimisation du temps de l'acquisition des données, PCA, logiciel STIR, fantôme 4D-XCAT.

ملخص

تقنية التصوير المقطعي بالإصدار البوزيتروني الديناميكي (dPET) تلعب دوراً رئيسياً في تحسين تشخيص السرطان، تقييم الاستجابة العلاجية، وتوصيف الأورام. ومع ذلك، تعاني من عدة قيود مثل الصور المشوشة وزمن طويل لتحصيل البيانات(وقت الفحص).

هدفت هذه الدراسة إلى تحسين قابلية اكتشاف الأورام في صور dPET بالإصدار البوزيتروني للـ^{18}F FDG وتقليص مدة الدراسة الإجمالية باستخدام طريقة تحليل المكونات الرئيسية (PCA) ، مع الحفاظ على إمكانية اكتشاف الأورام. لهذا الغرض، تم إنشاء خرائط توزيع تركيز ^{18}F FDG باستخدام نموذج لجسم الإنسان رباعي الأبعاد 4D-XCAT المدمجة مع منحنيات توزيع النشاط الزمني المحسوبة باستخدام نموذج قياسي ثلاثي الأقسام للـ^{18}F FDG و تم إدراج ورم كبدي كروي بقطر 9 مم في نموذج لجسم الإنسان 4 4-D-XACT. تم استخدام برنامج إعادة بناء الصور STIR لإنشاء صور ديناميكية ^{18}F-FDG PET. ثم تم تطبيق طريقة PCA على صور الـ ^{18}F PET FDG الديناميكية المحاكاة المولدة في أوقات مختلفة للمسح (0-11، 0-13، 0-15، 0-20، 0-25، 0-35، 0-40، 0-45، 0-50 و 0-55 دقيقة)، وعند T=35-55 دقيقة.

تم تقييم الصور التي حصلنا عليها باستخدام المكونات الرئيسية (PCI) بصرياً ومقارنتها بالصور المجمعة عند T=35-55 دقيقة التي تم إنشاؤها بتطبيق طريقة (SUMmed)المستخدمة في الممارسة السريرية. ثم تم اعتبار نسبة الورم / الخلفية (TBR) وخطوط النشاط (ALP) في التقييم الكمي.

بالنسبة لقابلية اكتشاف الأورام، أظهرت المقارنة بين صور الـ PCI1, PCI2, PCI3 و SUMأن PCI2 قد يوفر قابلية اكتشاف أفضل للورم مقارنة بالصورSUM المستخدمة في الممارسة السريرية عندT=35-55.

بالنسبة لتقليل زمن الحصول على البيانات، أظهر التقييم البصري للصور الـ PCI1, PCI2, PCI3 و SUMأن PCI3لديها قابلية اكتشاف أفضل الأورام بغض النظر عن وقت المستخدم للحصول على البيانات. وأظهر التقييم أيضا ان PCI2 له قابلية اكتشاف جيدة للورم في جميع الأوقات، باستثناء 11 و 13 دقيقة، في حين أظهر PCI1 قابلية اكتشاف الورم أقل في جميع الأوقات.

من الناحية الكمية، فإن TBR المقدر على PCI3 يشبه ذلك المحسوب في صور SUM (TBR على PCI3 هو 2.49 ± 0.72 و3.08 ± 0.49 على صور SUM) ولكنه أعلى من ذلك المحسوب على PCI1 وPCI2 من التوقيت من 11 إلى 35 دقيقة. يتناقص TBR الذي تم الحصول عليه على PCI1 مع زيادة وقت تحصيل البيانات. في PCI2، يزداد TBR مع الوقت (بحد أقصى 3.87 ± 1.11 في 55 دقيقة).

تشير النتائج التي تم الحصول عليها في هذه الدراسة إلى استخدام PCI3 عند 20 أو 25 دقيقة لتقليص وقت الفحص. وتوضح هذه الدراسة أن PCA يمكن أن يحسن إمكانية اكتشاف الأورام و يقلص وقت الفحص في التصوير الديناميكي ^{18}F FDG PET ، وبالتالي زيادة راحة المريض وتقليل تأثيرات الحركة على الصور.

الكلمات الدالة:

صور ديناميكية ^{18}F-FDG PET، إمكانية اكتشاف الورم، تقليص وقت الفحص، تحليل المكونات الرئيسية، برامج لإعادة بناء الصور، نموذج لجسم الإنسان 4D-XCAT

General Introduction

GENERAL INTRODUCTION

Medical imaging is an essential diagnostic tool in oncology and an effective tool for assessing tumor extension. The primary objective of such medical technologies is the early detection of cancer to help deciding the best treatment option. It provides clinicians with precise anatomical information (e.g., CT, ultrasound, MRI, etc.) and very important functional and/or metabolic information (e.g., fMRI, PET, SPECT, dPET).

Positron Emission Tomography (PET) is a nuclear medicine imaging technique that allows early diagnosis of different types of cancer. The ^{18}F-FDG radiotracer allows lesion characterization, staging, and therapy monitoring of different types of tumors [CZE06] [GAM02]. In clinical routine use of PET imaging, data acquisition is performed 60 min after ^{18}F-FDG injection using a single static frame [BOE15]. The generated images are converted to Standardized Uptake Value (SUV) images for analysis by the oncologists. These images are normalized to the ^{18}F-FDG activity injected and the patient weight [HUA11]. Being derived from static acquisition, the SUV does not provide information about the ^{18}F-FDG kinetics that are subject to variations in uptake period, duration of the scan time, and plasma glucose level [BOE11].

Several attempts have been made to improve image quality, quantitative accuracy, and reduce radiation dose in static PET imaging [KEY95] [KUH16][TAT03][BOUC23]. Similarly, significant efforts have been undertaken in dynamic PET to improve tumors diagnosis and therapy response assessment, taking advantage, for example, of the dynamic course of the ^{18}F-FDG spatial distribution in the imaged organ to evaluate the ^{18}F-FDG metabolic rate. Dynamic PET (dPET) imaging technique had a significant impact in this regard and had aided in the initial diagnosis and characterization of tumor [ZHU19][NOZ15][RUS13][KIM09][HER88][YAO95]. On the other hand, a limited number of studies have explored lesions detectability in parametric PET and static PET images [DIM21a][DIM21b]. Moreover, compared to SUV images, parametric images have demonstrated the ability to improve tumor detectability [FAH19]. However, there is still a shortfall of studies investigating lesion detectability and dPET remains limited to research [DIM21a][DIM21b]. dPET suffers from several drawbacks such as the long time duration of data acquisition (60 min is used in ^{18}F-FDG studies), high noise of the data

(limited counts in short frames duration), and invasive procedures used in the determination of the arterial Input Function (IF) [WU95][BEN05] [DEG][CHE07][ALE20].

Several studies have been carried out to optimize the acquisition time in dPET. Grkovski et al. [GRK17] showed that the acquisition time could be reduced to 20 min in the case of head and neck cancers. The kinetic parameters obtained were rather equivalent in a comparison study carried out by Torizuka et al. [TOR00] using 30 min and 60 min acquisition protocols. The work of Visser et al. [VIS08] on 13 patients with non-small cell lung carcinoma reported an agreement between 30 min and 50 min acquisition protocols.

dPET images can be analyzed using different strategies, such as the Patlak method [PAT85], full compartmental modeling methods [BEN07], and non-compartmental [THI05], that produce parametric images to extract further information. The use of the Patlak method and compartment modeling allows the calculation of the metabolic rate of glucose and the kinetics of ^{18}F-FDG to distinguish between benign and malignant lesions. These methods require the use of an arterial sampling, which complicates and increases the study duration [BIS02]. Principal Component Analysis (PCA), which is one of non-compartmental methods, does not require IF and does not include any model-based restrictions since it is independent of any kinetic model. PCA is one of the most commonly used tools for studying brain disorders [FRI93][PED94][ZUE03] and estimating characteristic images that can be used to delineate regions of interest; these images are subsequently used to estimate radiotracer kinetics in myocardial perfusion studies [FRO01][FRO01]. However, PCA is still of limited use in oncology studies [THI03]. Moreover, PCA images have not been used to assess improvements in lesion detectability in ^{18}F-FDG-PET studies. To the knowledge of the authors and from the existing literature, the PCA method has not been used specifically to investigate the shortening of the acquisition time in ^{18}F-FDG PET/CT tumor imaging.

Therefore, this study aimed to enhance the quality of ^{18}F-FDG PET images and shorten the total duration of ^{18}F-FDG while preserving the detectability of lesions using the PCA method. This was investigated by means of estimating relevant images from dynamic imaging sequences that provided a lesion detectability level similar to that of the usual static images acquired at 35 to 55 mins post-injection. Full-length and shorter dynamic sequences were assessed both qualitatively and quantitatively to demonstrate the potential of the proposed methodology. To do

so, a realistic 4D XCAT human torso phantom with the standard 3-compartment model was utilized to generate time-dependent activity and 511 keV attenuation maps. Open-source Software for Tomographic Image Reconstruction (STIR) [THI12] was employed to reconstruct the dynamic ^{18}F-FDG-PET images from the series of activities. The PCA method was implemented and applied to the dynamic ^{18}FDG-PET reconstructed images at different scanning times (11, 13, 15, 20, 25, 35, 40, 45, 50, and 55 min), producing Principal Component Images (PCIs). The PCIs were visually assessed and compared to the SUMmed images obtained at t=35-55 min. The Tumor-to-Background Ratio (TBR) and Activity Lines Profiles (ALPs) were considered for the quantitative assessment.

This thesis manuscript was structured as follows:

Chapter I, firstly, provides an overview about PET technique and the general principle of PET imaging. Then, it gives details about the physics behind PET imaging and summarizes some algorithms used in medical image reconstruction and software used for the visualization and analysis of medical images. It also discusses the different types of numerical phantoms used in medical imaging and ^{18}F-FDG compartment models. Finally, it gives a brief review on simulation in PET and the theoretical basis of PCA method.

Chapter II details the methodology adopted and tools used to simulate dynamic ^{18}F-FDG PET images. It also presents and discusses the achieved results. The methodology section describes how to generate activity maps and calculate time-activity curves using the ^{18}F-FDG three-compartments model. It details also the reconstruction procedure followed, using STIR software.

Chapter III presents the methodology and results of using the proposed PCA approach to enhance lesion detectability and reduce the data acquisition time. The procedures used to generate PCIs and SUM images were described in detail. The quantitative and qualitative comparisons of the images generated for lesion detectability assessment and scanning time optimization are discussed in separate sections.

At the end of this manuscript, we present a general conclusion and perspectives of the work.

Chapter I:
PET imaging

Introduction

This chapter serves as an introduction, offering a comprehensive overview of the fundamental principles, historical development, and widespread applications of PET imaging. In this chapter, we outline several key points, such as the general principles of PET imaging and the physics behind PET imaging, including the decay of the radionuclide, annihilation of the positron, radiation interactions with matter, instrumentation and different coincidence events that can destroy the quality of PET images.

I.1 PET overview

PET, or Positron Emission Tomography, is a nuclear medicine imaging technique that uses a radioactive tracer to produce a three-dimensional image or map of functional processes in the body. The images are obtained by gamma camera scanner (Figure I.1). PET scans are used to observe metabolic processes and can be used to study various conditions, such as cancer, heart diseases, and neurological disorders. It is considered as a complementary technique of medical imaging called anatomical, such as radiography, ultrasound, computed tomography (CT, usually called "X-ray scanner", or magnetic resonance imaging (MRI), which provide information on the structure of organs, their shapes, their limits, and, in some cases, their contents (bone structures, bladder stones, etc.).

Figure I.1: A PET/CT scanner, Discovery 710, General Electric (GE) [WWW01]

The idea of using short-lived positron emitters for physiological studies was born in the 1950s. The first tomographic instruments used in research appeared in the 1960s [KUH62] when the feasibility of a PET scan using two detectors was demonstrated [BRO69]. In the 1970s, the first prototype PET system was developed by Edward J. Hoffman and Michael

Phelps at the University of Washington (Saint Louis) [PHE75]. The first images of patients quickly followed [HOF76], marking the arrival of PET imaging in clinical use.

However, the quality of the images obtained was poor because of low computing power and the lack of development of efficient image reconstruction algorithms.

In the early 1990s, the first whole-body PET system was described [DAH92], and the first PET system was dedicated to small animal studies [CUL92]. In the 1990s and early 2000s, the first PET systems coupled with computed tomography (PET-CT) were developed and introduced, allowing anatomical information to be obtained along with metabolic information. In the 2010s, the first PET systems coupled with MRI (PET-MRI) were introduced.

This diagnostic tool is now increasingly used worldwide. In Algeria, there are, at present, 4 PET scanners in state and private hospitals. In addition, almost all PET systems currently in service worldwide are PET-CT systems.

The clinical applications of PET imaging include oncology (diagnosis, characterization and monitoring of tumor evolution, etc.), cardiology (myocardial viability and perfusion study) and neurology (Alzheimer's disease, Parkinson's disease, epilepsy, cerebral vascular pathologies).

In the preclinical field, PET imaging of small animals, called microTEP (μTEP) imaging, is used for the development of new drugs as well as for the study of new therapeutic strategies, such as vectorized internal radiotherapy β or α.

I.2 General Principle of PET Imaging

PET requires injecting the patient with a radiopharmaceutical (or radiotracer). This drug involves coupling between a vector molecule (single molecule, group of molecules, proteins, or antibodies), also called a tracer or vector, and a radioactive isotope (or radioisotope), called a marker (Figure I.2).

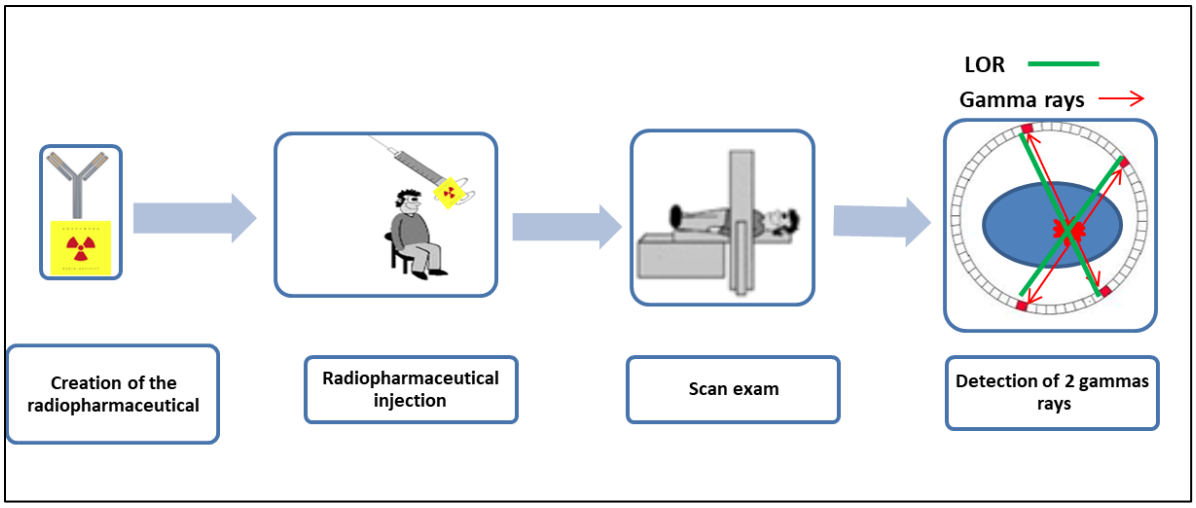

Figure I.2: Diagram representing the principle of a PET

The tracer allows fixation of the compound in the body and is adapted to the biological process studied. The marker makes it possible to identify the place of attachment of the radiopharmaceutical via the emission of ionizing radiation that passes through the patient. The main radiopharmaceutical used in PET is fluorodeoxyglucose combined with 18-fluorine (^{18}F-FDG). Indeed, this ^{18}F-labeled glucose analog allows visualization of cells with high carbohydrate metabolism, such as tumor cells.

Radioisotopes used in PET are positron emitters (β+). The positrons (β+) created during the decay of the radioisotope annihilate with an electron of the medium after a brief course in the tissues, thus giving rise to two photons, γ, of the same energy (511 keV) emitted simultaneously, in almost opposite directions.

These two photons are detected via a set of detectors arranged in rings inside which the patient is positioned. These rings are made of crystals and are coupled to electronic modules, allowing preprocessing of the signal before it is directed to a computer.

The position of the radiopharmaceutical in the patient's body is estimated via temporal coincidence detection of the pairs of photons created from the measured annihilation position. The projection of their detection location on a couple of crystals is called the response line (LOR). During the acquisition, the camera records the number of events detected for each LOR, as well as some physical parameters of interest (the time of flight of the two photons, their energy, etc.). The information contained in each LOR is called a projection, and all these projections constitute the measured "raw" signal. The conversion of these projections to the final medical image is called tomographic reconstruction.

Two types of acquisition data are commonly used: static and dynamic.

The static mode refers to acquiring images at a single time point after the radiotracer injection has reached a relatively stable distribution within the body. The dynamic mode aims to evaluate the distribution of tracer concentrations within organs over a period of time. It serves as a crucial method for investigating the temporal functionality of organs within live (in vivo) settings. It is used in many applications, ranging from cancer to neuroinflammation [MUZ12][LAV15].

Dynamic PET imaging consists of acquiring a sequence of static PET images in frames at varying intervals after administering the radiopharmaceutical agent. The duration of each frame may vary according to the particular study being conducted. These time frames can be too short to detect/capture quick variations in radiotracer concentration uptake post injection or can be extended when less noisy images are needed. Figure I.3 shows an illustration of a 4D dynamic PET image scans.

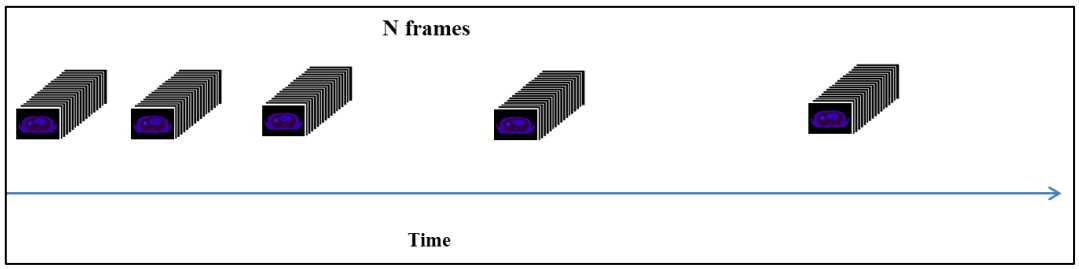

Figure I.3: Illustration of a 4D dynamic PET images scans.

The dynamic PET data can be acquired using two general approaches:

- List mode acquisitions (not all PET scanners allow for this mode): This mode permits the storage of every occurred event including: the instant of detection, the energy of the photon detected, and the number of the corresponding LOR. In this mode, the N frames and their durations are determined by the user after the acquisition process. In this case, the sinogram is divided into N frames, followed by an individual reconstruction of each frame.
- Standard dynamic acquisition: In this mode, time intervals for each frame are established before the scanning process. Every detected event during these intervals is recorded in the respective sinogram for that specific time point. Then, individual reconstructions are conducted for each of these sinograms separately [RAH09].

I.4 The physics behind PET imaging

PET imaging is based on positron emission. These positrons are emitted by atoms of a radioisotope in an unstable state. Radioisotopes are usually produced artificially by cyclotrons or generators. These radioisotopes are partly characterized by their half-life, $T_{1/2}$.

A positron emitter must have some physical characteristics to be used in nuclear medicine. Indeed, the half-life time $T_{1/2}$ must be long enough to allow the transport from the cyclotron radiopharmaceutical to the hospital, administration and the observation time of the physiological phenomenon of interest. In parallel, this time must also be relatively short to avoid prolonged irradiation of patients and/or care personnel. It is also necessary to take into account the additional radiation potentially emitted by the isotope: it is preferable to choose isotopes whose ratio of branching (i.e. probability of emission) of the positrons is as high as possible. Finally, the energy of the positrons must be as low as possible to minimize their path before annihilation.

TABLE I.1 Characteristics of the main radioisotopes used in PET.

Table I.1: Characteristics of the main isotopes used in clinical and preclinical PET [CHER05]. The average course of β+ represents the thickness necessary to absorb half of the β+.

Radioisotopes	**^{11}C**	**^{13}N**	**^{15}O**	**^{18}F**
Period (minutes)	20,3	10	2,1	109,8
Branching ratio of + (%)	99,8	100	99,9	96,7
Mean kinetic energy of β+ (MeV)	0,39	0,49	0,73	0,25
Maximum kinetic energy of β+ (MeV)	0,96	1,19	1,72	0,64
Mean range β+ in water (mm)	1,1	1,3	2	0,6
Maximum range β+ in water (mm)	3,9	5,1	8	2,3

I.4.1 Decay of the radionuclide: positron emission

A positron-emitting radioisotope is an isotope made unstable by an excess of protons. During the decay process, a proton (p) of the nucleus is converted into a neutron (n) via the weak nuclear force. A positron (β+) and an electron neutrino (η) are then emitted to balance the process, as shown in equation (**I.1**):

$$p \rightarrow n + \beta^{+} + \eta \qquad \textbf{(I.1)}$$

The β+ emission is not mono-energetic. The positron is emitted with an excess of kinetic energy that allows it to move in the surrounding environment (Figure I.4).

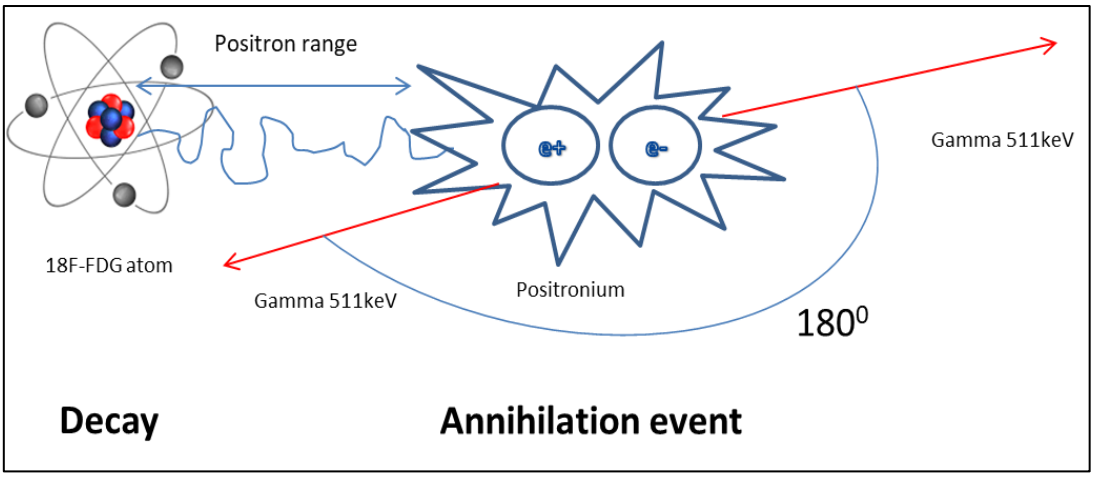

Figure I.4: Diagram showing the different steps from decay to generation of γ-511 keV photons: 1) decay and path of the positron until the encounter with an electron of the medium; 2) creation of the positronium; 3) positronium annihilation and creation of γ-511 keV photons.

I.4.2. Annihilation of the positron

The positron emitted will then interact with the surrounding environment, undergoing a series of collisions with the electrons of matter. Each of these collisions causes a loss of its initial kinetic energy via ionization or excitation. When a positron loses almost all of its kinetic energy, it combines with an electron of the medium, forming a quasistable system called a positronium. The half-life of this atom is a hundred nanosecond maximum. The positronium disappears by producing two photons, γ, of approximately 511 keV, which are emitted simultaneously and in quasicollinearity. Indeed, before annihilation, the positron has residual kinetic energy and a nonnull amount of movement. Due to the principle of conservation of energy and momentum, the energy of the two γ photons is actually slightly different from 511 keV, and there is a noncollinearity effect between them. The distribution of the angles between the two annihilation photons is estimated by a Gaussian function. The mid-height width (FWHM) was 0.58 ± 0.25 [BAI05]. The energy difference between the two γ photons is related to this noncollinearity and is also expressed by a Gaussian function. The relationship between the FWHM of the noncollinearity angle θ and the FWHM of the E energy difference of the two γ photons is given by the following equation (I.2):

$$\Delta\theta(rad) = \frac{2\Delta E}{511(KeV)} \qquad \textbf{(I.2)}$$

By applying the formula (I.2) with an angle of 0.25, we find an energy difference of approximately 2.6 keV between the two annihilation photons, or 0.5% of the average energy (511 keV).

I.4.3 Radiation interactions with matter

The γ-511 keV photons, which result from annihilation, propagate and interact with the surrounding environment and the detection elements of the PET camera. In the energy ranges for PET imaging, the following three main interactions are generally considered: the photoelectric effect, Compton scattering and, to a lesser extent, Rayleigh scattering. The absorption of γ-511 keV photons during these interactions follows an exponential law and can be expressed as:

$$I(x) = I_0 . e^{-\int_0^x \mu(E,x)dx} \qquad \textbf{(I.3)}$$

where $I(x)$ represents the number of photons transmitted without any interaction after path x in matter and I_0 is the initial number of photons considered. μ(E, x) (cm-1) represent the contribution of all linear attenuation coefficients of each type of interaction to a given energy E. Therefore, we have:

$$\mu(E) = \mu_{\text{photoelectric}}(E) + \mu_{\text{Compton}}(E) + \mu_{\text{Rayleigh}}(E) \qquad \textbf{(I.4)}$$

Each of these coefficients is related to the effective section σ_i (cm2 per atom), which reflects the probability of each interaction i, by the following relationship:

$$\mu_i(E) = \frac{N_A \rho}{A} \sigma_i(E) \qquad \textbf{(I.5)}$$

where N_A (mol^{-1}) is the Avogadro constant, A(g) is the atomic mass of the medium and ρ (g/cm3) is its density.

I.4.3.a Photoelectric effect

The photoelectric effect corresponds to the total transfer of energy from the γ-511 keV photon to an electron in a deep atomic layer strongly bound to the atom. The photon disappears completely, and the lost kinetic energy is entirely attributed to the electron, which is subsequently ejected from the atom. The energy of the Eγ incident photon given to the electron contributes in part to the release of the electron from its atomic layer, and the rest is recovered as kinetic energy.

The cross section of the photoelectric effect [KNO99] is given by the following relation:

$$\sigma_{\text{photoelectric}}(E) \propto \frac{Z^n}{E^{3.5}} \qquad n \in [4;5] \qquad \textbf{(I.6)}$$

From equation **(I.6),** we can observe that the photoelectric effect is more likely when the energy of the photon is low and the atomic number Z of the medium is high. For detection purposes, it will be interesting to choose materials with a high Z.

I.4.3.b Compton scattering

Compton scattering is an inelastic process, which means that the incident photon at γ-511 keV loses some of its energy. During this process, a photon γ provides part of its energy to an electron weakly bound to its nucleus. This electron is extracted from the atom with E_e kinetic energy, and a scattered photon is created with E_c energy.

The E_c energy of the scattered photon as a function of the scattering angle is given according to the following formula:

$$E_c = \frac{E_\gamma}{1+\frac{E_\gamma}{m_e+c^2}(1-cos\theta)} \qquad \textbf{(I.7)}$$

where m_e is the electron mass, c is the speed of light and θ is the scattering angle.

The cross section of this interaction is given by the Klein–Nishina relationship [KLE19]. This indicates that the Compton effect is greater when the material is dense. Compton diffusion is the dominant interaction in soft tissues (major tissues of the body) for energies between 40 keV and 10 MeV [GAG92].

$$\sigma_{\text{Compton}}(E) \propto \frac{\rho}{E_\gamma} \quad E > 100\ KeV \qquad \textbf{(I.8)}$$

I.4.3.c Rayleigh scattering

Rayleigh scattering is a coherent (elastic) process, which means that the incident photon is deflected without energy loss. This effect concerns photons of low energies that pass near electrons strongly bound to the atom. In this case, the electron is not ejected from the atom, and the energy transfer to the atom is negligible.

The cross-section of this interaction increases with the square of the atomic number Z and the density of the medium. However, this decreases the energy of the incident photon (equation (1.10)). In the energy ranges around the photons at γ-511 keV, this effect is negligible in biological tissues and detection systems compared to the photoelectric effect and Compton diffusion.

$$\sigma_{\text{Rayleigh}}(E) \propto \frac{\rho z^2}{E_\gamma} \qquad \textbf{(I.9)}$$

Table I.2 gives the linear attenuation coefficients at 511 keV for photoelectric and Compton scattering effects for three of the main detection crystals used in PET (BGO, LSO, GSO) and for the main biological tissues.

Table I.2: Table showing linear attenuation coefficients at 511 keV for each of the photoelectric and Compton interactions for the main biological tissues and the three main detection crystals used in PET: bismuth germanate (BGO), lutetium oxyorthosilicate (LSO) and gadolinium oxyorthosilicate (GSO) [PHE06][KNO08].

Materials	**Soft tissue**	**Bone**	**BGO**	**LSO**	**GSO**
$\mu_{\text{Photoelectric}}$ **(cm^{-1})**	0,00002	0,001	0,4	0,3	0,18
μ_{Compton} **(cm^{-1})**	0,096	0,169	0,51	0,58	0,46
μ_{Total} **(cm^{-1})**	~ 0,096	0,17	0,96	0,88	0,7

I.4.4 Detection process

The role of a PET system is to detect γ-511 keV photons that have left the patient or phantom. The material used at the entrance of the detection chain must therefore have the ability to stop γ photons while maintaining an energy of approximately 511 keV. It is preferable that the photoelectric µP ratio/µCompton is also as high as possible. Indeed, the photoelectric effect corresponds to a complete local energy deposit, while Compton scattering can generate multiple interactions with neighboring detection elements, leading to difficulties in locating the interaction [CHE12]. Figure I.5 illustrates all the elements that make up the conventional detection chain used in PET.

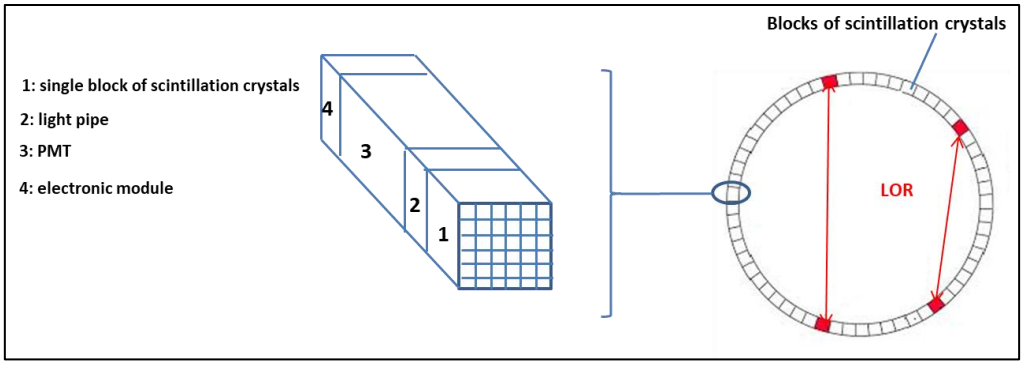

Figure I.5: Diagram showing the main components of the detection chain of a standard PET scanner.

I.4.4.a Detection crystals: scintillator

The scintillation crystals constitute the first element in the detection chain. These scintillators are usually arranged in crystals of small dimensions and aim to convert incident gamma photons into luminous photons. The emission of these luminous photons is isotropic and directly proportional to the amount of energy deposited by incident photons at γ-511 keV [KNO99]. The shape of a crystal is most often a parallelepiped with an entrance face of square section and small dimensions (in the order of a millimeter in preclinical PET). These geometric characteristics aim to optimize the detection sensitivity while preserving good spatial resolution. The luminous photons are then captured by photomultiplier tubes, the second element of the detection chain.

Scintillators are characterized mainly by their density ρ (directly related to the stopping power of photons at γ-511 keV), their conversion efficiency η of photons at γ-511 keV into luminous photons, the time τ necessary for the emission of light photons after the energy deposition of γ-511 keV photons, the wavelength range of the emitted light and the transparency of the scintillating crystal. Table 1.3 summarizes the characteristics of the major crystals currently used in PET imaging.

Table 1.3: The main characteristics and parameters associated with three of the main scintillating crystals used today in clinical and preclinical PET [KNO99]. Some parameters may vary depending on the crystal purity, temperature, pressure, and ambient humidity.

Crystals scintillators	**BGO**	**LSO**	**GSO**
Density ρ ($g.cm^{-3}$)	7,13	7,4	6,71
Efficiency η (photons/511 keV)	4200	13000	4600
Decay τ (ns)	300	~ 40-50	~60
Linear attenuation μ(511 keV) (cm^{-1})	0,96	0,88	0,7
Ratio Photoélectric/Compton	0,78	0,52	0,35

I.4.4.b Light guide

After interactions occurred within the crystals, the light signal must be transported to PhotoMultiplier Tubes (PMTs), the next step in the detection chain. An optical guide for a refractive index close to that of the crystals is interposed between the crystals and the PMT. The dimensions of this guide are carefully chosen to fit the shape of the PMT input interface.

I.4.4.c Photomultiplier tubes

The majority of PET systems use photomultiplier tubes (PMTs) (Figure I.6) as converters of light photons into electric current [HAM94], although there are now other systems, such as SiPM modules from APD technologies ("Avalanche PhotoDiode", [REN02]) [SCH08]. The light from the optical guide is transmitted through the entrance window of the TPM, and the photocathode is excited (Figure I.6). The photocathode consists of a very fine material capable of releasing the maximum number of electrons via the photoelectric effect from the incident light energy. The probability that a bright photon releases an electron, called the quantum efficiency, is related to the overall sensitivity of the PMT.

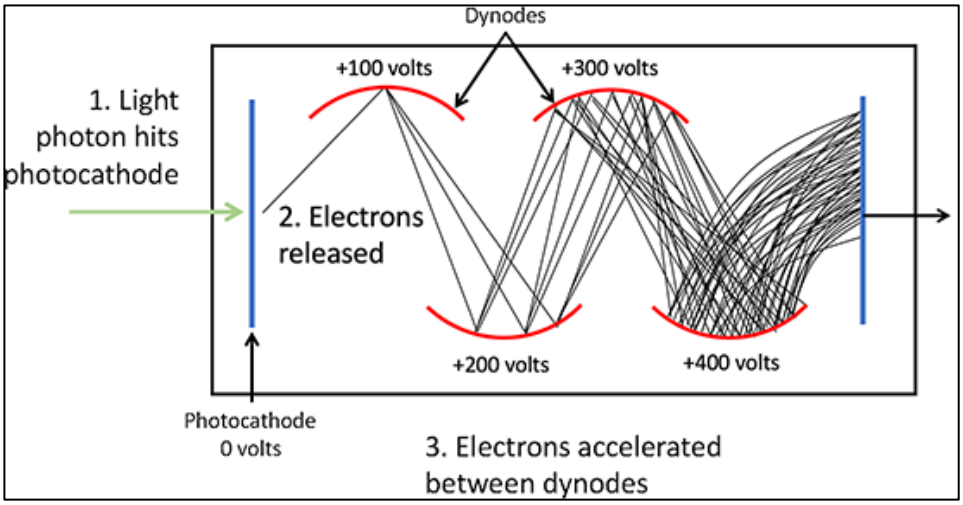

Figure I.6: Diagram of a photomultiplier tube (PMT).

A strong difference in potential accelerates the electrons thus formed on the photocathode and directs them to the first dynode after focusing. The electrons deposit their energy on this dynode, which in turn generates some electrons (from 3 to 5 secondary electrons per incident electron). The ratio between the number of secondary electrons emitted and the number of incident electrons is called the secondary emission coefficientρ. These secondary electrons are directed to another dynode, where they in turn generate new secondary electrons. This process continues through the application of increasing electrical potential between subsequent dynodes. Generally, a PMT consists of 10 to 15 dynodes, and the last step is repeated 10 to 15 times. The set of electrons leaving the last dynode is collected by the anode, and a measurable electrical signal proportional to the number of incident light photons is thus created. The gain G (or amplification) of the PMT is given by the following relation (1.12):

$$G = \rho^n \qquad \textbf{(1.10)}$$

where n is the number of dynodes. Typically, the gain of a TPM is between 10^5 and 10^8.

After processing and corrections (calculation of the energy of incident photons, elimination of low-energy photos, etc.), the signal leaving the PMT is stored as a digital signal.

I.4.5 Coincidence events

The first step is to apply an energy window with low and high thresholds to eliminate the maximum number of scattered photons and high-energy photons. The high threshold also eliminates stack-up effects, during which several photons deposit energy almost simultaneously in the same block of crystals, leading to a detection greater than 511 keV.

Each of the photons-γ thus discriminated is called a single event.

The temporal coincidence then consists of matching the detected photons. When a photon (1st single event) is recorded by the system, a window of a few nanoseconds is opened. If a photon is detected in this time interval (2nd single event), it is considered that it is the second photon related to annihilation; thus, a coincidence is recorded within the LOR associated with the crystal couple involved.

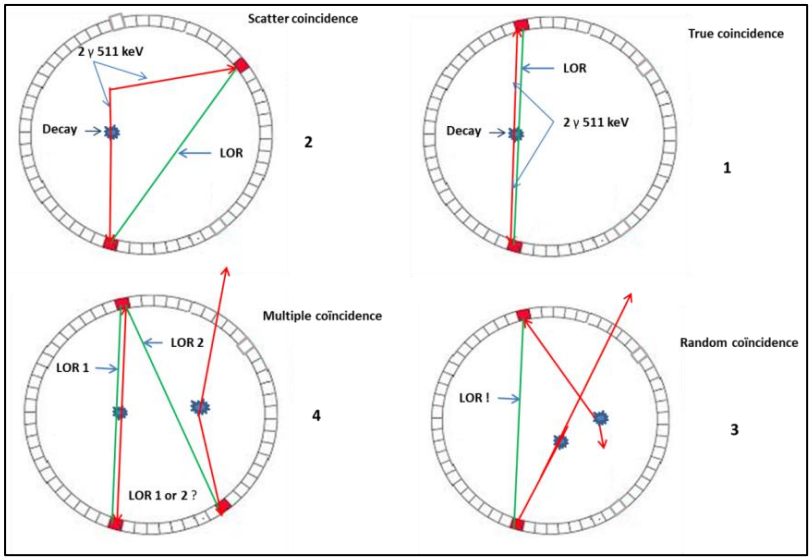

FIGURE I.7: Different types of coincidences.

The following different types of coincidences could be recorded:

I.4.5.a True coincidences

A true coincidence corresponds to the detection of the two photons-γ of annihilation, which has undergone no diffusion in the object medium (Figure I.7.1). The LOR is overlaid with the direction of the annihilation photons and thus provides relevant information on the localization of the radiopharmaceutical. True coincidences are the signals to be reconstructed.

The number of true coincidences N_T is proportional to the activity A_0 of the source:

I.4.5.b Scatter coincidences

A scattered coincidence corresponds to a coincidence of the two photons-γ of an annihilation in which at least one has undergone one or more successive Compton diffusions in the object medium (Figure I.7.2). The energy of these photons is therefore less than 511 keV, and their trajectory is modified. The scattered coincidence rate recorded during a scan is proportional to the activity and depends on the energy resolution of the detectors, the energy window and the external shielding of the PET system.

In this case, the LOR is no longer overlaid with the place of annihilation, and the location information of the radiopharmaceutical is incorrect. An overestimation of the activity in the imaged volumes (especially in the regions without or low activity), a decrease in the contrast in the image and a decrease in spatial resolution were observed in this case.

I.4.5.c Random coincidences

Random coincidences correspond to the coincidence of photons-γ from two different annihilations (Figure I.7.3) without considering any scattering.

In this case, there are two distinct decays, and the associated LOR has no connection with the actual location of annihilation. The location information of the radiopharmaceutical is also erroneous, resulting in an increase in the general background noise that degrades the restitution of the different contrasts.

The number of random coincidences N_{Random} for a source activity A_0 is estimated by the relationship:

$$N_{Random} = 2\tau * \left(N_{single}^{A}.N_{single}^{B}\right) \propto A_0^2 \qquad \text{(I.11)}$$

With:

$$N_{single}^{A} = A_0.\Omega_A.\varepsilon_A \text{ and } N_{single}^{B} = A_0.\Omega_B.\varepsilon_B \quad \text{(I.12)}$$

With:

- ✓ 2τ is the duration of the time window in seconds.
- ✓ $N_{single}^{A}$and $N_{single}^{B}$are the single events recorded in detectors A and B, respectively.
- ✓ $\Omega_{A/B}$ are the solid angles of detectors A and B, respectively.
- ✓ $\varepsilon_{A/B}$ are the efficacies of detectors A and B, respectively.

To minimize the random coincidence rate, we try to decrease the size of the time window. In practice, efforts will also be made to minimize the activity of the radiopharmaceutical while preserving metabolic information.

I.4.5.d Multiple coincidences

A multiple coincidence corresponds to a coincidence of more than two annihilation photons-γ (Figure I.7.4). There are therefore at least two distinct decays, and no LOR can be directly obtained.

A first solution to treat this type of coincidence is to not take into account any of the detections and therefore not consider this type of event. Conversely, all detections can be taken into account to form all possible coincidences. In the case of three-photon detection, as in our example, there will be three distinct coincidences, of which at least two will be associated with coincidences. Finally, it is also possible to keep only the two detections associated with the most energetic radiation and thus form a single coincidence.

I.4.6 Data storage

Events detected coincidentally were recorded in binary format on a computer connected to the PET system. There are three storage formats: list mode, full histogram, and sinogram [CHER12].

I.4.6.a List-mode

This format contains all the information accessible from the detection chain, without any compression. We can generally find the energies, times and indices of the detection crystals associated with the two photons γ relative to the LOR considered. Each line of this

binary contains information about coincidence events. In practice, several tens of gigabytes (GB) can be exceeded for acquisitions with very high statistics. With this format, the user has all the information accessible from the measurement and can thus use all types of reconstructions offered by the machine or even use its own reconstruction algorithms.

I.4.6.b Full histogram

The full histogram format is a compressed format that contains only the number of coincidences detected in the LOR. In practice, the binary file associated with this format is of constant size and depends only on the total number of possible theoretical LORs of the PET system under consideration.

I.4.6.c Sinogram

A sinogram is a compressed format of the data that allows visualization of all the coincidences recorded as image matrices (2D or 3D). It is defined as a regular sampling of space according to a coordinate system dependent on the angle and distance of the LOR from the center of the tomograph (Figure I.8).

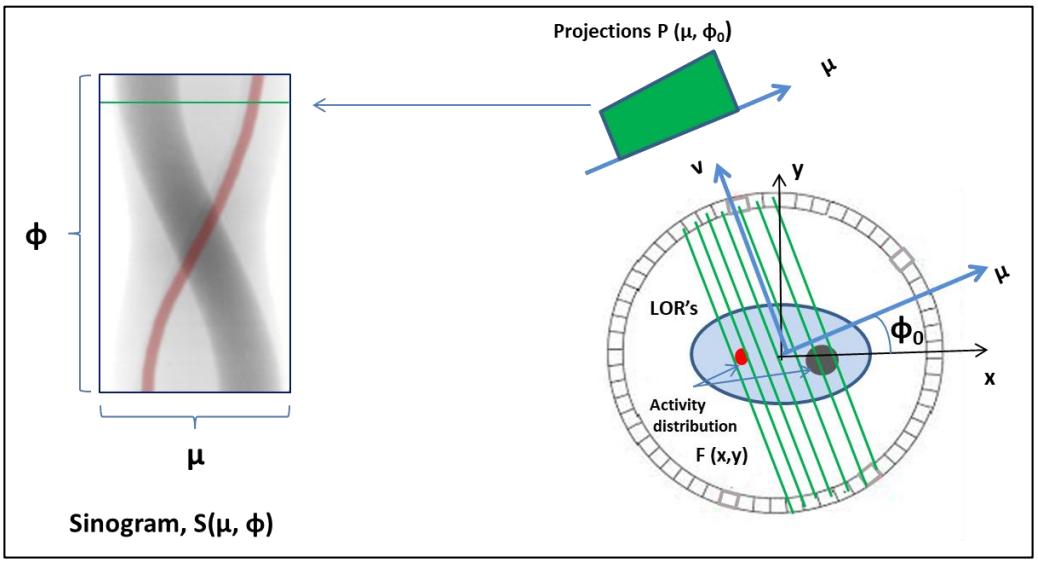

Figure I.8: Schema explaining the creation of a sinogram [MOR19].

Let us consider an activity distribution f(x, y) in a two-dimensional object and the 2D graph s(u, Φ) associated with the transverse plane perpendicular to the detector axis, called the slice. To locate an LOR in this plane, the cylindrical coordinates u and Φ correspond to the distance of the LOR from the center of the tomograph and the angulation angle from the horizontal axis x (azimuth angle), respectively.

The projections p (u, Φ_0) are expressed according to equation (1.13):

$$p(\mu, \Phi_0) = \int_{-\infty}^{+\infty} f(x,y)dv = \int_{-\infty}^{+\infty} f(u.\cos\Phi_0 - v.sin\Phi_0,\ u.sin\Phi_0 + v.cos\Phi_0)dv \qquad (1.13)$$

Each line of a sinogram represents the entire LOR associated with the same azimuth angle Φ, and the position on this line corresponds to the distance u of the LOR considered. The total of the projections according to the set of angles Φ then represents the sinogram s(u, Φ) of the considered section.

A pixel of the sinogram corresponds to an LOR between two pairs of elementary detectors, and each event is detected in coincidence increments by one unit of the value of this pixel.

A PET system with N detection rings can generate N direct sinograms in 2D mode, one sinogram for each ring and N^2 sinograms in 3D mode.

In practice, the sinogram is the most commonly used tool in clinical and preclinical practice because it allows simplified visualization of the data before the reconstruction step. However, its use is less flexible than that of the list-mode format or the full histogram because irreversible approximations are made before reconstruction.

I.5 Algorithms used in medical image reconstruction

Medical image reconstruction algorithms play a crucial role in transforming raw imaging data into meaningful diagnostic images. The choice of algorithm depends on the imaging modality, the specific application, and the trade-offs between speed and image quality. The following are some commonly used algorithms in medical image reconstruction:

- **Filtered Back Projection (FBP):** FBP is a traditional algorithm used in X-ray computed tomography (CT) and single-photon emission computed tomography (SPECT). It works by applying a filter to the projections and then back-projecting them to reconstruct the image. However, because of its speed, FBP may not handle complex data such as MRI or PET scans well [KAK01].
- **Iterative Reconstruction:** These methods iteratively update an initial estimate of the image until it converges to a solution. Variants include the Expectation-Maximization (EM) algorithm and Maximum Likelihood (ML) algorithms. Iterative reconstruction is commonly used in PET and SPECT imaging [ZEN10].

- **Radon Transform**: The Radon transform is central to CT image reconstruction. It mathematically describes how X-ray projections relate to the original image, forming the basis for FBP and iterative methods in CT reconstruction [KAK01].
- **Filtered Iterative Reconstruction:** Combining FBP and iterative techniques, these algorithms filter projection data before using an iterative approach. They aim to improve image quality, particularly on CT images [ZEN10].
- **Algebraic Reconstruction Techniques (ART):** ART is an iterative reconstruction technique used in CT and emission tomography. Image pixels are updated in parallel based on the discrepancies between the measured and estimated projection data [KAK01].
- **Statistical reconstruction:** In emission tomography (such as PET and SPECT), statistical reconstruction algorithms take into account the Poisson statistics of the photon counts. Maximum Likelihood Estimation (MLE) and Ordered Subsets Expectation Maximization (OSEM) are commonly used in this context [SHE82] [ZEN10].
- **Model-Based Reconstruction:** These methods use mathematical models to describe the physics of the imaging process. They are used in various modalities, including MRI and PET, to account for artifacts and improve image quality [FES20].
- **Dictionary Learning:** In MRI reconstruction, dictionary learning techniques aim to find sparse representations of images in a dictionary. These methods can lead to compressed sensing and accelerated MRI acquisition [ELA10].
- **Machine Learning-Based Reconstruction:** Deep learning techniques, including Convolutional Neural Networks (CNNs), have been applied to medical image reconstruction tasks, showing promise in tasks such as denoising, artifact reduction, and superresolution [ZHU18].
- **Filtered Sinogram Reconstruction:** Used in various modalities, including CT, this approach applies filtering in the sinogram domain before backprojection, aiming to reduce artifacts and improve image quality [FES20] [KAK01].

The choice of algorithm depends on the specific imaging modality, the type of data acquired, and the trade-offs between speed, image quality, and computational resources. Advances in computer technology and the adoption of machine learning techniques have led to significant improvements in medical image reconstruction in recent years.

Several open-source software tools and libraries are available for PET image reconstruction. These tools can be valuable for researchers and institutions looking to develop and customize PET reconstruction algorithms. Some of these open-source PET reconstruction software programs include the following:

- **STIR (Software for Tomographic Image Reconstruction):** STIR is an open-source reconstruction toolkit designed for PET and SPECT. It offers a range of reconstruction algorithms, including filtered back projection, expectation-maximization, and OSEM (Ordered Subsets Expectation-Maximization). STIR is widely used in the PET community and provides flexibility for algorithm development.
- **PETPVC:** PETPVC is an open-source software package for partial volume correction (PVC) in PET imaging. It is designed to improve the quantitative accuracy of PET data by correcting for partial volume effects. PVC is an important step in the image reconstruction process for PET.
- **OSEM++:** OSEM++ is an open-source software tool for PET image reconstruction that focuses on the OSEM algorithm. It was developed as a research project and can be used to implement and experiment variations of the OSEM algorithm.
- **PyPET: Python for PET image reconstruction:** PyPET is an open-source Python library that provides tools for PET image reconstruction and analysis. It offers various reconstruction algorithms, including MLEM (Maximum Likelihood Expectation-Maximization) and OSEM, along with image analysis capabilities.

These open-source tools and libraries offer flexibility and customization options for PET image reconstruction, making them valuable resources for researchers and institutions working in the field of medical imaging. You can explore and choose the one that best fits your specific needs and research objectives.

STIR is one of the most common software programs used by the scientific community. Below, we provide some details about this software.

I.5.1 STIR software

STIR, software for tomographic image reconstruction, is an open-source software library used for reconstructing tomographic images in various fields, primarily in the medical imaging domain. It is widely used for positron emission tomography (PET) and single-photon

emission computed tomography (SPECT) image reconstruction, but it can also be applied to other tomographic imaging modalities [THI12].

The following are some key points about STIR:

- Open-Source: STIR is an open-source project, which means that the source code is freely available to the public. This encourages collaboration and development by the user community.
- Purpose: STIR is designed for the reconstruction of 2D and 3D images from projection data acquired through various imaging techniques, with a primary focus on positron emission tomography (PET) and single-photon emission computed tomography (SPECT).
- Functionality**:** A range of reconstruction algorithms, including analytical methods such as filtered back-projection, as well as iterative algorithms such as OSEM (ordered subset expectation maximization) and MLEM (maximum likelihood expectation maximization), are available.
- Applications**:** STIR is utilized primarily in the field of nuclear medicine, specifically for the reconstruction and analysis of PET and SPECT images. It facilitates the accurate visualization and quantification of biological processes within the human body, aiding in the diagnosis and treatment of various diseases.
- Data Processing: Data processing provides tools for calibrating and performing corrections on acquired data, such as normalization, attenuation correction, scatter correction, and random estimation.
- Data Formats: STIR supports various data formats commonly used in medical imaging, including Interfile, ECAT, and DICOM formats.
- Platform compatibility: STIR is typically available for Unix-based systems (Linux, mac, OS) and can also be compiled on Windows with some effort.
- Community and Documentation: STIR has an active user and developer community. Comprehensive documentation, including user guides and API (Application Programming Interface) references, is available to help users understand and utilize the software effectively.

- Other applications: Beyond medical imaging, STIR can be adapted for other tomographic imaging techniques, such as industrial nondestructive testing, geophysics, and materials science.

The STIR is a versatile and powerful tool for researchers, physicists, and engineers working with tomographic image reconstruction. It offers a flexible framework for experimenting with different algorithms and techniques to obtain high-quality reconstructed images from raw projection data [WWW03].

Below is how STIR is typically used:

- **Data Acquisition:** STIR is used to acquire projection data from images. It can also be employed when projection data are acquired using a tomographic imaging system. These data consist of multiple 2D views or projections taken from different angles around the object of interest.
- **Data Preprocessing:** Before reconstruction, the acquired projection data may require preprocessing, which includes normalization, correction for attenuation (the absorption of radiation in tissues), scatter correction (accounting for scattered radiation), and random estimation (to correct for random coincidence events in PET).
- **Image reconstruction:** STIR is subsequently used to reconstruct a 2D or 3D image from the preprocessed projection data. It employs various algorithms, including iterative methods such as ordered subset expectation maximization (OSEM) or maximum likelihood expectation maximization (MLEM), to generate the reconstructed image.
- **Image** quality improvement: Reconstructed images may require postprocessing to enhance image quality, remove noise, and apply filters or other techniques for optimal visualization and interpretation.
- **Clinical and Research Applications:** The reconstructed images have applications in both clinical and research settings. In clinical practice, they are used by physicians for diagnosis and treatment planning. In research, these images can be analyzed for scientific investigations, and new algorithms can be developed and tested.
- **Software Development:** STIR also serves as a valuable resource for software developers and researchers who wish to develop image reconstruction algorithms, as it provides an open-source platform for experimentation and testing.

- **Educational and Training Purposes:** Educational institutions and medical facilities often use STIR as a teaching tool to instruct students and train professionals in the principles of tomographic image reconstruction.
- **Collaboration and customization: The** STIR can be customized and adapted for specific research and clinical requirements. It also allows for collaboration between researchers and developers in the field of tomographic imaging.

  In summary, STIR is used to process raw projection data from various tomographic imaging modalities, apply corrections and normalization, and reconstruct high-quality 2D or 3D images. These reconstructed images are vital for clinical diagnosis, treatment planning, and medical research, making STIR an essential tool in the field of medical imaging.

I.6 Softwares used for visualizing and analyzing medical images

There are several software options available for visualizing medical images, and the choice of software often depends on the specific type of medical image data and the desired functionality. The following are some popular software tools for medical image visualization:

3D Slicer: As mentioned earlier, 3D Slicer is an open-source platform designed for medical image analysis, visualization, and 3D reconstruction. It is a versatile tool for various imaging modalities.

- **OsiriX**: OsiriX is a popular medical image viewer and postprocessing software primarily used in the field of radiology. It offers advanced features for viewing and analyzing DICOM images.
- **MITK (Medical Imaging Interaction Toolkit)**: MITK is an open-source platform for the development of medical image analysis applications. It provides visualization and processing tools for various imaging modalities.
- **ImageJ**: ImageJ is a widely used open-source image processing program that can be extended with plugins to support various medical image formats and analyses.
- **ITK-SNAP:** ITK-SNAP is an open-source software application for segmenting and visualizing 3D medical images. It is particularly useful for tasks such as image segmentation and region-of-interest analysis.
- **Mango:** Mango is a simple, free software tool for viewing and working with medical images, particularly for brain imaging studies. It supports various file formats and basic image manipulation.

- **Horos:** Horos is an open-source DICOM viewer for medical images, and it is an offshoot of OsiriX. It is known for its user-friendly interface and broad platform support.
- **Aeskulap:** Aeskulap is an open-source DICOM viewer that offers basic image viewing and manipulation features.
- **MIPAV (Medical Image Processing, Analysis, and Visualization):** MIPAV is an open-source image analysis and visualization software developed by the National Institutes of Health (NIH). It supports various medical image formats and provides tools for image processing.
- **3D-DOCTOR:** 3D-DOCTOR is a commercial medical imaging software that offers advanced tools for image processing, 3D rendering, and visualization.

These software tools vary in terms of their capabilities, complexity, and intended use cases. It is important to select the one that best suits your needs, considering factors such as the type of medical imaging data you work with and the specific analysis and visualization tasks you want to perform.

Below, we provide the detailed features of the 3D slice software used in this study.

I.6.1 3D slicer software

3D Slicer is a free, open-source software platform used for medical image analysis, visualization, and 3D image reconstruction. It is primarily designed for the healthcare and medical research communities and provides a wide range of tools and features for working with medical imaging data (Figure I.9) [FED12].

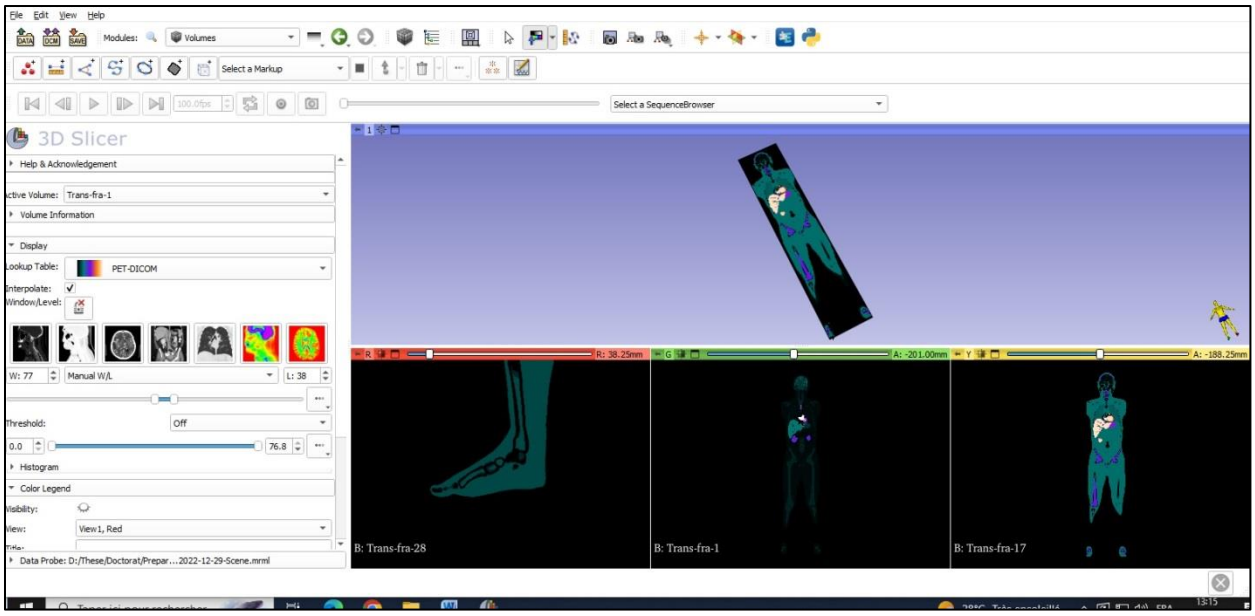

Figure I.9: General view of a 3D slicer.

The following are some key aspects and features of 3D Slicer:

- **Image analysis:** 3D Slicer can load and manipulate various types of medical imaging data, such as MRI, CT, ultrasound, and PET scans. It offers tools for image registration, segmentation, and visualization.
- **3D Visualization:** The software allows users to create 3D visualizations of medical images, making it particularly useful for surgical planning, anatomical studies, and education.
- **Image Registration:** 3D Slicer can align and register multiple medical images or image volumes, which is essential for tasks such as fusing MRI and CT scans.
- **Segmentation:** Users can perform manual or automated segmentation of structures and regions within medical images. This approach is valuable for defining regions of interest and conducting quantitative analyses.
- **Volume Rendering:** The software offers volume rendering capabilities to visualize medical data in 3D, providing detailed, anatomical context.
- **Extension Support:** 3D Slicer is highly extensible, and users can enhance its functionality by installing various extensions and plugins, which cover a wide range of medical image analysis tasks.
- **Research and Clinical Applications:** 3D Slicer is widely used in both research and clinical applications, such as image-guided surgery, radiation therapy planning, and neuroimaging studies.

- **Community and Support:** It has an active and supportive user community, making it a valuable resource for those working with medical image data. There are user forums, documentation, and tutorials available to assist users.
- **Open Source:** 3D Slicer is open-source, which means it is freely available for anyone to use, modify, and distribute. This open nature has contributed to its popularity in the medical imaging field.

3D Slicer is widely used in medical research, healthcare institutions, and educational settings. It provides a versatile platform for a wide range of medical image analysis tasks, from basic image viewing to advanced research applications.

I.7 Phantoms

There are two types of phantoms, physical phantoms, which can be used for experimental measurements, and digital phantoms, which can be used in calculation codes.

I.7.1. Physical phantom

The phantoms used in these measurements are generally composed of tissue-equivalent materials and are often equipped with dosimeters for performing measurements. More than 27 physical phantoms exist; the Rando-Alderson phantom is one of the most frequently used phantom in medical applications. It consists of three types of tissue: soft tissue, bone and lungs [XU14].

I.7.2. Numerical phantoms

Digital phantoms are essentially geometric models that present the internal and external anatomical characteristics of the human body. Since 1960, approximately 121 mathematical phantoms [XU14] have been reported in the literature for studies involving ionizing and nonionizing radiation. An important part of the literature on medical imaging is related to the development and application of these phantoms. The organs and surfaces of digital phantoms are defined by several geometric modeling techniques, quadric equations, voxels, and deformable surfaces called NURBS (non-Uniform rational basis splines), to adjust the shape of each organ in the desired way (respiratory movement, etc.).

I.7.3 Geometric modeling techniques for numerical phantoms

For radiation imaging and dosimetry, a phantom must define the surface of an organ in which radiation interactions and energy deposits must be calculated. Clearly, the construction of such phantoms must take into account several factors, such as anatomy, radiosensitivity, computational efficiency and geometric compatibility, with a Monte Carlo code [XU14].

Two general methods of solid geometry modeling have been widely developed by the computer graphics community (CAD): constructive solid geometry (CSG) and Boundary REPresentation (BREP) [XU14].

CSG: Creates a solid object using Boolean operators to combine very simple objects called primitives. Examples of these primitives include cubes, cylinders, prisms, pyramids, spheres, cones and ellipsoids, which are surfaces that are easily described by quadric equations. Moreover, CSG representations are easy to adopt and can work well when objects are relatively simple in shape**.**

In BREP, there are two types of information: topological and geometric. Topological information provides relationships between vertices, edges, and faces. In addition to connectivity, topological information also includes edge and face orientations. There is more advanced modern BREP-based software where information outside of an object is defined as NURBS. For these models, the surfaces are very smooth, and the faces are represented as polygons with vertices defined by a set of values of coordinates x, y and z. A polygonal mesh or unstructured grid is a collection of vertices and polygons that define the geometric shape of a polyhedral object. In principle, NURBS and polygonal meshes are interchangeable BREP data structures.

Unlike the CSG representation, the BREP representation is much more flexible because a better set of operating tools is available. These features allow BREP-based phantoms to include very complex anatomical features. In addition, the BREP technique is ideal for determining the extent of surface deformation, which is necessary for adjusting organ size and for simulating organ movements [XU14].

For example, in Figure I.10 below, the left lung can be represented in the CSG method as "half an ellipsoid with a section removed". These surface equations are computationally efficient and are accepted by almost all Monte Carlo codes. However, even with complicated

and carefully designed Boolean operations such as this, phantoms based on quadric surfaces are not anatomically realistic in terms of geometry.

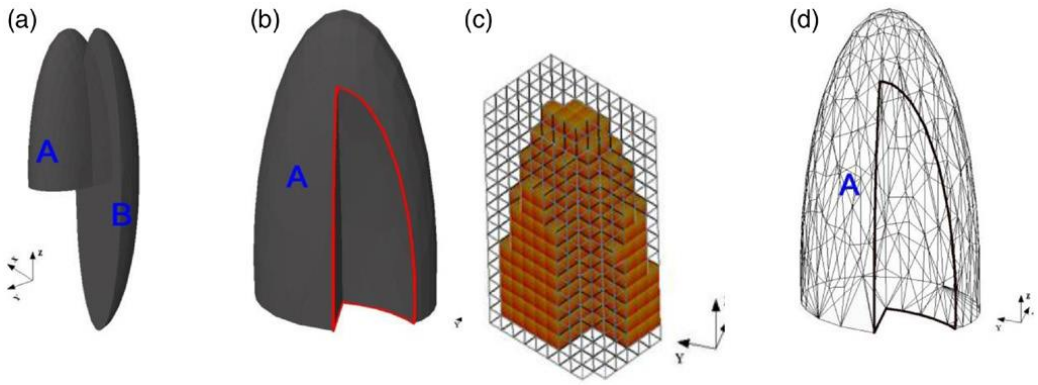

Figure I.10 The left lung was defined by different modeling techniques. (a) A mathematical lung model using the CSG method before and after a Boolean operation is performed to remove a section of ellipsoid B from A. (b) A CSG method involving a group of rigid voxels with anatomical detail dependent on voxel size. (c) Representation of the lung based on voxels. (d) A type of BREP method involving a polygonal mesh that is easy to deform anatomically accurately [XU14].

I.7.4. Different Digital Phantoms

I.7.4.a. Analytical phantoms

Analytical phantoms are modeled by the CSG method, which represents human anatomy by simple geometric shapes. An example of these phantoms most commonly used in dosimetry is the one described in [CRI87], which developed the ORNL series (Oak Ridge National Laboratory). This series or "family" of phantoms consisted of an adult male; a newborn; and individuals aged 1, 5, 10 and 15 years and adults. These phantoms also represented an adult woman with additional anatomical characteristics. Each phantom is composed of three types of tissue with distinct densities: bone, soft tissues and lungs. They were defined analytically in three main geometric sections, as illustrated in Figure (1.11.a): an elliptical cylinder representing the arms, chest and hips; a truncated elliptical cone representing the legs and feet; and an elliptical cylinder representing the head and neck. Figure (I.11.b) shows the skeleton, internal organs and tissues. An image of the "family" is shown in Figure I.11.c.

The simple geometry of these phantoms makes Monte Carlo calculations faster than with more complex phantoms. Mathematical phantoms have been used for applications in medical imaging, nuclear medicine and radiation protection [NCR96][ICR92].

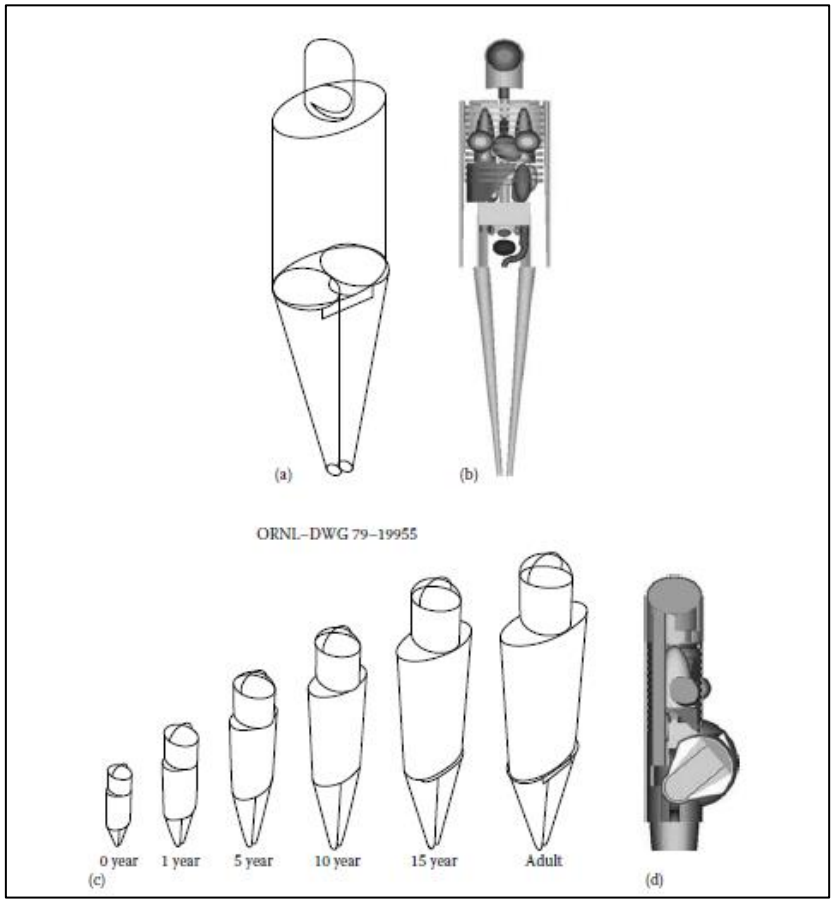

Figure I.11: Analytical phantom. (a) External view of an adult male. (b) Skeleton and internal organs. (c) Representation of individuals of both sexes and different ages. (d) Cross-sectional view of the phantom for a 9-month pregnant woman [XU14].

I.7.4.b Voxelized phantoms

Voxelized phantoms are fundamentally different from analytical phantoms. A tomographic image dataset consists of several slices, each displaying a two-dimensional (2D) pixel map of the anatomy. The 3D volume of a voxel is measured by multiplying the pixel size by the thickness of an image slice. Unlike analytical phantoms, which are based on quadratic surface equations, a voxelized phantom contains a large number of small cubes grouped together to represent different anatomical structures. However, quadratic surface equations and voxels belong to the same class of geometries.

Creating a voxelized phantom involves four general steps:

- Acquire a set of tomographic images (e.g., CT, MR, or anatomical photograph) that cover the entire body volume;
- Identify organs or tissues of interest (e.g., lungs, liver, skin, etc.) from the original image by assigning each pixel an identification number;
- Specify density (for example, soft tissue, hard bone, air, etc.);
- Save segmented image slices in a 3D volume that can be used for 3D visualization (for anatomical structure verification) and Monte Carlo calculations.

[LEE06] analyses the difference in results between the use of mathematical phantoms and voxelized phantoms: dose differences of up to 115% for some organs were observed. These parameters are explained by geometric approximations in mathematical phantoms as relative positions of organs and geometric shape. Several types of voxelized phantoms have been created, such as the phantoms developed by [ZUB92] (phantom ZUBAL), [KRA03] (phantom MAX and FAX), [XU00][XU05] (VIP-MAN phantom), [LEE05] (pediatric VIP series: 9 months, 4, 8, 11 and 14 years), and [ZHA03] (VCH phantom).

For these phantoms, the reference values given by the International Commission on Radiological Protection publications 89 [ICR02] and [ICR93] are used to define the mass, dimensions and materials of these phantoms.

I.7.4.c Hybrid phantoms

Voxelized phantoms and their posture and size are difficult to modify. These phantoms are modeled by the BREP technique [XU14], which is why hybrid phantoms have been developed. In these phantoms, the contours of the organs are expressed by the NURBS surfaces. Once the desired geometry is obtained, the phantom can be voxelized into its new shape.

Paul Segars of Duke University used NURBS-based techniques to create the first hybrid phantom. The well-known NCAT phantom was developed from CT images and was subsequently extended into the 4th dimension to model cardiac and respiratory movements [SEG01]. The 4D NCAT phantom offers a more realistic model of anatomy, the cardiac system, and respiratory motion [SEG02]. 4D NCAT has been widely used in nuclear medicine imaging research. The NCAT phantom design also served as the basis for the development of a 4D digital mouse phantom named MOBY [SEG04] and, ultimately, the 4D XCAT whole-

body hybrid phantom [SEG10]. This phantom was used in our study; it will be described in more detail in chapter II.

Figure I.12 shows the original phantom of MIRD with the phantoms MCAT, NCAT, XCAT, MOBY and ROBY provided by Paul Segars.

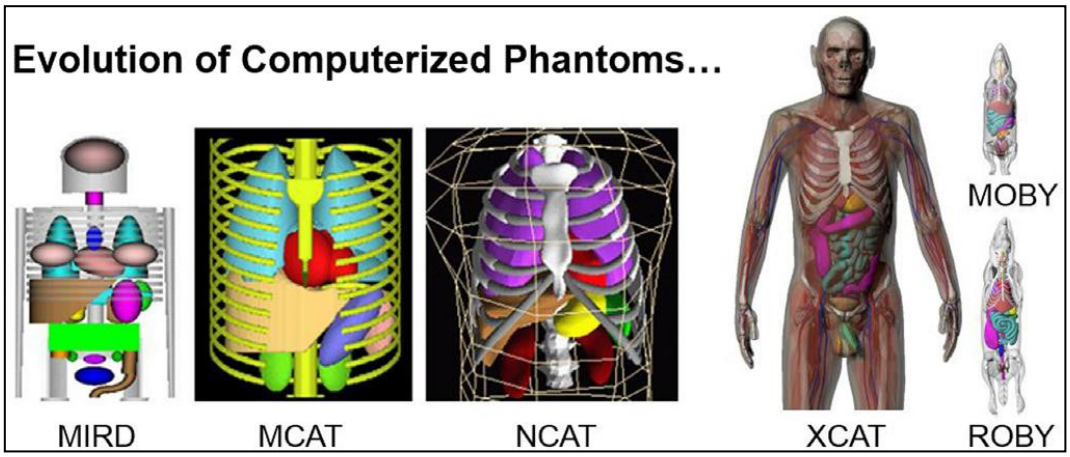

Figure I.12: Comparison between the first-generation MIRD analytical phantom and the MCAT, NCAT, XCAT, MOBY and ROBY hybrid phantoms provided by Paul Segars [XU14]**.**

I.8 Principal component analysis

In the medical diagnosis process, digital medical images are processed and analyzed to provide meaningful and reliable information to physicians. These images can be analyzed using different methods, such as principal component analysis (PCA), which is considered an efficient method. PCA is a statistical method that has been identified as one of the most powerful techniques for image recognition and compression. Its main goal is to reduce the large dimensionality of the data space (observed variables) to a smaller essential dimensionality of the feature space (independent variables). The method is based on a mathematical procedure for extracting relevant information by calculating the eigenvalue decomposition (EVD) of a data covariance matrix or singular value decomposition (SVD) of a data matrix.

Historically, the use of PCA dates back to the beginning of the last century through the work of Pearson [PEA01]. It was originally used as a tool for detecting outliers by projecting the data on the different factorial axes and calculating the distances from these axes. The use of PCA in this way is not very practical since an operator must view the projections to make a

decision on the presence of outliers. In 1933, PCA was developed by Harold Hotelling and named the Hotelling transform [HOT33].

Depending on the application domain, PCA is also known as the Hotelling transform or discrete Karhunen–Loève transform (KLT) in signal processing [GHA91] and Singular Value/EigenValue Decomposition (SVD/EVD) in numerical analysis.

Since PCA is a well-known and powerful technique for feature extraction and dimension reduction, it has been widely used in data analysis and data compression. In the medical image domain, it is used in a wide range of applications, such as image fusion, segmentation, image registration, feature extraction, compression and classification. In the following paragraph, we will cite some works about the applications of PCA in the area of nuclear medicine.

In nuclear medicine, PCA has proven to be useful for discriminating between patients with dementia of Alzheimer type and asymptomatic controls [FRI93][HAB08][SCA04]. It has also been used to perform the fusion of CT-MRI and MRI images through the works of Vijayarajan & Muttan [VIJ15].

I.8.1 Definition

Principal component analysis (PCA) is a multivariate statistical method aimed at structuring and summarizing information. This method consists in transforming variables correlated to each other into uncorrelated variables called principal components. In dynamic image sequences, PCA allows to summarize and transform the content of a sequence of images indexed by time into a small number of images. The first images obtained represent the linear transformation of the original variables which contains the highest variance. The second images are also linear combinations of the original data which contains as much of the remaining variance as possible, and so on [PEA01].

Numerically, the data of the dynamic frames could be represented in the matrix Z, where each line contains the values of the pixels of each frame taken over the time.

$$Z = \begin{bmatrix} z_{1,1} & \cdots & z_{1,n} \\ \vdots & \ddots & \vdots \\ z_{m,1} & \cdots & z_{m,n} \end{bmatrix} \tag{I.14}$$

Before applying the PCA, we transform the matrix Z using the following pretreatment procedure:

$$x_{ij} = (z_{ij} - \overline{z}_j)/s_j \quad \text{(I.15)}$$

where

- z_{ij} and x_{ij} are the original and final values, respectively, of pixel i (i=1...n) of frame j (j=1...,m).
- $\overline{x_j}$and S_j are the mean and the standard deviation of the jth row of the original data Z matrix, respectively.

Once the data are transformed, the *i*th principal component is calculated as follows:

$$Y_i = X'e_i = x_{i1}e_{1i} + x_{i2}e_{2i} + \cdots + x_{im}e_{mi} \ (i = 1,2, \dots, m) \quad \text{(I.16)}$$

With:

$$Var\ (Y_i) = \lambda_i \text{ and } \mathrm{Cov}\left(Y_i, Y_j\right) = 0, i \neq j \quad \text{(I.17)}$$

e_i and λ_i are the eigenvector and eigenvalue, respectively, and $\lambda_1 > \lambda_2 > \cdots > \lambda_2 > 0$. The values of e_i and λ_i were calculated using the SVD function.

Approximately 80-90% of the total variance in the data can be attributed to the first few components. These components can replace the original *m* variables without much loss of information.

I.9 ^{18}F-FDG Compartment Models

Compartmental models for ^{18}F-FDG (fluorodeoxyglucose) are mathematical representations of the distribution and kinetics of ^{18}F-FDG in the human body. These models help researchers and clinicians understand how ^{18}F-FDG is taken up, distributed, and cleared within tissues, which is crucial for interpreting PET images and extracting quantitative information about tissue metabolism. They can be used to estimate important parameters, such as the rate of FDG uptake in different tissues, the rate of FDG clearance from the bloodstream, and the metabolic activity of specific organs or tissues. This information can be crucial for diagnosing and monitoring various diseases, particularly cancer and neurological disorders.

In a compartmental model for ^{18}F FDG, the body is divided into compartments, each representing a specific tissue or organ or state. The model describes the movement of FDG between these compartments over time. The basic idea is to use a system of differential equations to simulate how FDG is taken up by tissues, distributed throughout the body, and eventually cleared from the body. Different compartments may correspond to the blood, various organs, and other tissues of interest.

Typically, the model includes compartments such as the following:

1. Blood compartment: This compartment represents the FDG in the bloodstream and may include an arterial compartment to account for the arterial input function (AIF), which represents the FDG concentration in the arterial blood.
2. Tissue compartments: These compartments represent the various tissues or organs under investigation, such as the brain, heart, liver, or tumors. Each tissue compartment has parameters that describe the uptake and clearance of FDG in that tissue.
3. A compartment for excretion: This accounts for the elimination of FDG from the body, typically via the urinary system.

The specific structure of the compartmental model can vary depending on the study and the complexity needed to accurately represent the biological processes in question. The model parameters are estimated from dynamic PET data, and various analysis techniques are used to derive meaningful information about glucose metabolism in different tissues.

Several compartment models are used for PET imaging, including the following:

I.9.1 Two-compartment model (one-tissue compartment model)

The two-compartment model, or one-tissue compartment model, is a simpler version of the compartment models used in positron emission tomography (PET) imaging. This model is used to describe the distribution and kinetics of a tracer within the body. The one-tissue compartment model assumes a single compartment for the tissue of interest.

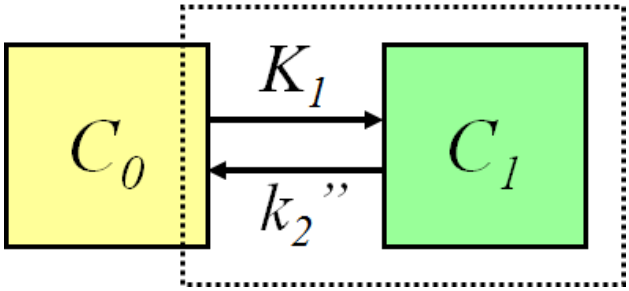

Figure I.13: Diagram showing the two-compartments model of ^{18}F-FDG uptake [WWW02].

In the context of ^{18}F-FDG PET imaging, the one-tissue compartment model consists of two main compartments:

Plasma Compartment: The plasma compartment represents the concentration of ^{18}F-FDG in the blood.

Tissue Compartment: In this model, there is only one tissue compartment, which represents the concentration of the tracer within the tissue of interest. This compartment accounts for both the uptake and clearance of the tracer in the tissue.

The one-tissue compartment model describes the transfer of ^{18}F-FDG from the plasma compartment to the tissue compartment and its subsequent clearance from the tissue. The compartments are connected by two rate constants, *K1* and *k2*. This model is governed by a differential equation that describes these processes.

The basic equation for a one-tissue compartment model is as follows:

$$\frac{dC_1(t)}{dt} = K_1 C_0(t) - K_2 C_1(t) \qquad \text{(I.18)}$$

- $\frac{dC_1(t)}{dt}$ represents the rate of change of ^{18}F-FDG concentration in the tissue compartment.
- $C_0(t)$ is the concentration of the tracer in the plasma compartment (blood).
- $C_1(t)$ is the concentration of the tracer in the tissue compartment.
- K_1: represents the rate of tracer transfer from the plasma compartment to the tissue compartment. It characterizes the rate of tracer uptake into the tissue.

- K_2**:** represents the rate of tracer clearance from the tissue compartment back to the plasma compartment. It characterizes the rate of ^{18}F-FDG leaving the tissue.

These parameters help describe the dynamics of ^{18}F-FDG uptake and clearance in the tissue of interest. Estimating these parameters from PET imaging data and plasma input function data allows for quantitative assessment of glucose metabolism in the tissue, in the case of ^{18}F-FDG. The one-tissue compartment model provides a simplified way to assess tissue metabolic activity, making it a useful tool for various clinical and research applications, especially in oncology for tumor characterization and monitoring treatment response.

I.9.2 Three-compartment model (two-tissue compartment model)

The two-tissue compartment model is a mathematical model commonly used in the analysis of ^{18}F-FDG PET images. This model is used to describe the distribution and kinetics of a tracer within the body and provides a more detailed understanding of the dynamics of tracer uptake and clearance compared to the one-tissue compartment model.

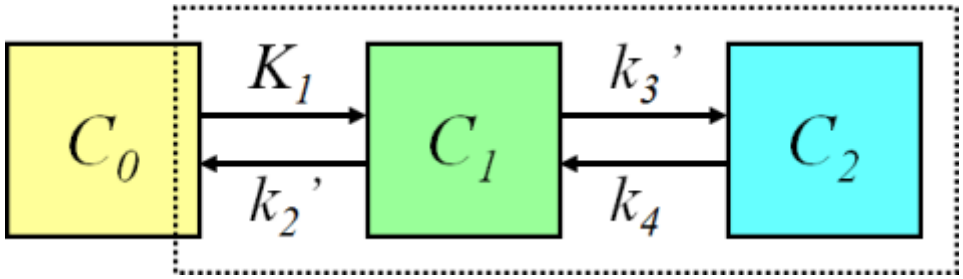

Figure I.14: Diagram showing the three-compartment model of ^{18}F-FDG uptake [WWW02].

In the context of ^{18}F-FDG PET imaging, the two-tissue compartment model consists of the following compartments:

- **Plasma Compartment:** This compartment represents the concentration of ^{18}F-FDG in the blood.
- **First Tissue Compartment (Free or Reversible Compartment):** This compartment represents the concentration of ^{18}F-FDG within the tissue of interest, accounting for the reversible uptake and release of the tracer.

- **Second Tissue Compartment (Irreversible or Trapped Compartment):** This compartment accounts for the irreversible trapping of ^{18}F-FDG within the tissue, representing the phosphorylated form of the tracer that cannot easily return to the blood.

The two-tissue compartment model describes the transfer of ^{18}F-FDG between the plasma compartment and the two tissue compartments, as well as the clearance of ^{18}F-FDG from both compartments. This model is governed by a set of differential equations that represent these dynamic processes.

$$\frac{dC_1(t)}{dt} = K_1C_0(t) - (K_2+K_3)C_1(t) + K_4C_2(t) \qquad \text{(I.19)}$$

$$\frac{dC_2(t)}{dt} = K_3C_1(t) - K_4C_2(t) \qquad \text{(I.20)}$$

where

- $\boldsymbol{C_0(t)}$ is the concentration of the tracer in the plasma compartment (blood).
- $\boldsymbol{C_1(t)}$ is the concentration of the tracer in the reversible compartment.
- $\boldsymbol{C_2(t)}$ is the concentration of the tracer in the irreversible compartment.
- **K_1 (influx rate constant):** This parameter represents the rate of ^{18}F-FDG transfer from the plasma compartment to the first tissue compartment.
- **K_2 (efflux rate constant):** This parameter represents the rate of ^{18}F-FDG transfer from the first tissue compartment back to the plasma compartment.
- **K_3 (phosphorylation rate constant):** This parameter represents the rate of conversion of ^{18}F-FDG in the reversible compartment to the irreversible compartment.
- **K_4 (dephosphorylation rate constant):** This parameter represents the rate of dephosphorylation of ^{18}F-FDG in the irreversible compartment.

Estimating these parameters from PET imaging data and plasma input function data allows for quantitative assessment of glucose metabolism in the tissue. The two-tissue compartment model provides a more comprehensive understanding of the dynamics of tracer uptake and retention within the tissue, making it a valuable tool for various clinical and

research applications, especially in the field of oncology for the assessment of tumor metabolism and treatment response.

I.9.3 Four-compartment model (three-tissue compartment model)

The three-tissue compartment model is an advanced mathematical model used in positron emission tomography (PET) imaging, particularly for studying the uptake and kinetics of radiolabeled tracers such as ^{18}F-fluorodeoxyglucose (^{18}F-FDG). This model, in which two tissue compartments are in parallel, is more complex and detailed than the one-tissue and two-tissue compartment models. It provides a deeper understanding of the dynamics of tracer distribution, binding, and clearance within the body.

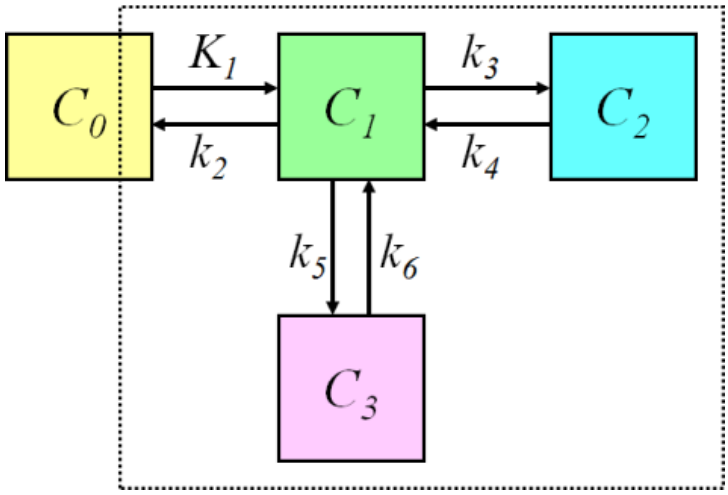

Figure I.15: Diagram showing the four-compartment model of ^{18}F-FDG uptake [WWW02].

In the context of ^{18}F-FDG PET imaging, the three-tissue compartment model involves three main compartments:

- **Plasma Compartment (Vascular Compartment):** This compartment represents the concentration of ^{18}F-FDG in the blood.
- **First Tissue Compartment (Free Compartment):** This compartment accounts for the reversible uptake and release of ^{18}F-FDG in the tissue. It represents the fraction of ^{18}F-FDG that can freely exchange between the tissue and plasma.
- **Second Tissue Compartment (Specific Binding Compartment):** This compartment represents the specific binding of ^{18}F-FDG to receptors or targets

within the tissue, such as cell membranes or cellular structures. It accounts for the fraction of ^{18}F-FDG that is specifically bound and retained within the tissue.

- **Third Tissue Compartment (Nonspecific Binding Compartment):** This compartment accounts for the nonspecific binding of ^{18}F-FDG in the tissue, which may include interactions with cellular components other than specific targets.

The three-tissue compartment model describes the transfer of ^{18}F-FDG between the plasma compartment and the three tissue compartments, as well as the clearance of ^{18}F-FDG from these compartments. This model is governed by a set of differential equations that describe the complex dynamics of tracer uptake, binding, and clearance within the tissue.

$$\frac{dC_1(t)}{dt} = K_1C_0(t) - (K_2+K_3 + K_5)C_1(t) + K_4C_2(t) + K_6C_3(t) \quad \text{(I.21)}$$

$$\frac{dC_2(t)}{dt} = K_3C_1(t) - K_4C_2(t) \quad \text{(I.22)}$$

$$\frac{dC_3(t)}{dt} = K_5C_1(t) - K_6C_3(t) \quad \text{(I.23)}$$

where

- $\boldsymbol{C_0(t)}$ is the concentration of the tracer in the plasma compartment (blood).
- $\boldsymbol{C_1(t)}$ is the concentration of the tracer in the free compartment.
- $\boldsymbol{C_2(t)}$ is the concentration of the tracer in the specific binding compartment.
- $\boldsymbol{C_3(t)}$ is the concentration of the tracer in the nonspecific binding compartment.
- **K1 (influx rate constant):** The rate of ^{18}F-FDG transfer from the plasma compartment to the free compartment.
- **K2 (efflux rate constant):** The rate of ^{18}F-FDG transfer from the free compartment back to the plasma compartment.
- **k3 (specific binding rate constant):** The rate of binding of ^{18}F-FDG to specific targets in the tissue.
- **k4 (specific unbinding rate constant):** The rate of release of specifically bound ^{18}F-FDG from the tissue to the plasma.

- **k5 (nonspecific binding rate constant):** The rate of nonspecific binding of ^{18}F-FDG in the tissue.
- **k6 (nonspecific unbinding rate constant):** The rate of release of nonspecifically bound ^{18}F-FDG from the tissue to the plasma.

Estimating these parameters from PET imaging data and plasma input function data allows for a comprehensive quantitative assessment of glucose metabolism and tracer binding within the tissue of interest. The three-tissue compartment model is particularly valuable for research and clinical applications that require a detailed characterization of tissue-specific interactions of radiolabeled tracers with biological targets.

I.10 Simulation in PET

Simulations can be used in PET to model and optimize various aspects of the imaging process. One common application is Monte Carlo simulations, which are used to predict the behavior of particles as they interact with matter. In PET, this can be used to simulate the interaction of the emitted positrons with the surrounding tissue, as well as the subsequent gamma rays that are produced during the annihilation process.

These simulations are valuable for understanding the behavior of radiation within the body, optimizing the design of PET scanners, and developing new image reconstruction algorithms to improve the quality and accuracy of PET images. Additionally, simulations can aid in the development and testing of new radiotracers for specific applications.

Here are a few areas where simulations are used in PET:

- **Image Reconstruction Algorithms**: Simulations are often used to develop and test image reconstruction algorithms. These algorithms process the raw data collected by PET scanners to create detailed 3D images. Researchers simulate the data acquisition process to optimize and refine these algorithms.
- **Detector simulation**: PET scanners use detectors to capture the radiation emitted by a radioactive tracer. Simulations can model how these detectors interact with radiation to improve their design and performance.
- **Monte Carlo simulations**: Monte Carlo simulations are frequently used to model the behavior of radiation in the human body and the detectors. These simulations can help in estimating the accuracy and quality of PET images.

- **Radiation Dose Simulation**: In a clinical setting, it's important to understand the radiation dose delivered to the patient during a PET scan. Simulations can help estimate and optimize the dose to minimize risks while maintaining image quality.
- **Patient-Specific Simulations**: Simulations can be used to create virtual patient models based on medical imaging data (e.g., CT scans) and simulate the entire process of a PET scan for specific patients. This is particularly useful for treatment planning and assessing the expected image quality in personalized medicine.
- **Phantom studies**: Simulations using phantoms (specially designed objects with known properties) are often performed to calibrate PET scanners and validate their performance.
- **Motion Correction**: PET scans can be affected by patient motion, especially in dynamic studies. Simulations can help develop and test motion correction techniques to improve image quality.

These simulations are crucial for improving the accuracy and reliability of PET imaging, optimizing scan protocols, and reducing radiation exposure while maintaining diagnostic quality. They also play a role in the development of new PET technologies and applications.

Conclusion:

This chapter has provided a broad and foundational understanding of PET imaging, exploring its principles, historical evolution, physics, instrumentation, radiotracers, and algorithms that make PET imaging possible.

Chapter II:
Simulation of dynamic ^{18}F-FDG PET images

Introduction

In this chapter, we present the methodology employed and the results obtained from the simulation of dynamic ^{18}F-FDG PET images. The simulation process involves several steps, which are summarized in Figure II.1.

In the following sections, we delve into the details of these steps, from the calculation of the input function to the generation of the ^{18}F-FDG PET images.

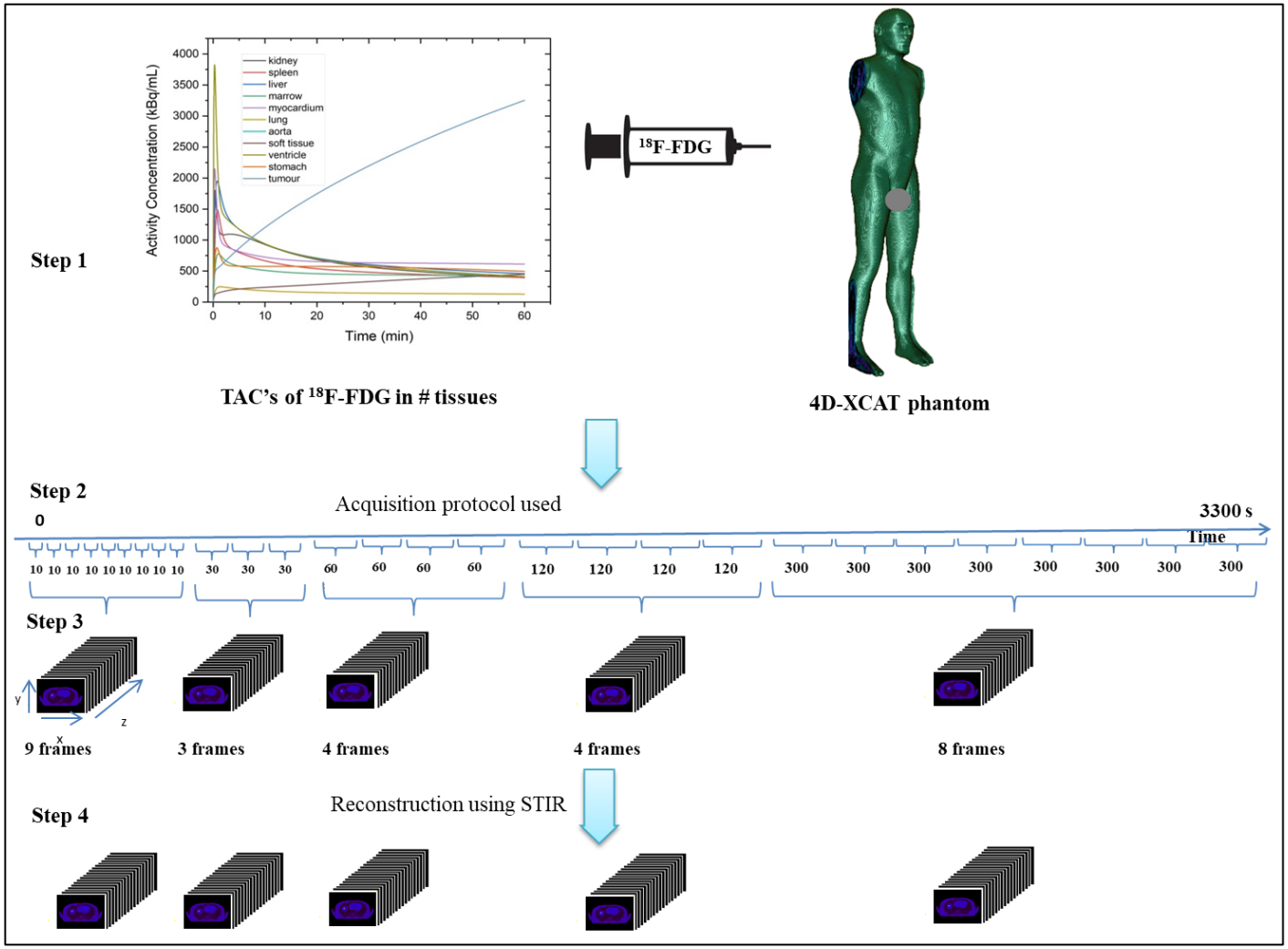

Figure II.1. Flowchart illustrating the steps involved in simulating the ^{18}F-FDG PET images. 1) The TACs of different tissues were calculated and combined with the 4D-XCAT phantom. 2) A real acquisition protocol was adopted to generate 28 frames of activity maps. 3) Calculation of 18F-FDG concentration, according to each time frame, and generation of activity maps. 4) Reconstruction of the ^{18}F-FDG PET images using the STIR reconstruction software.

II.1 Methodology used in the simulation of dynamic ^{18}F-FDG PET images

II.1.1 Activity maps generation

II.1.1.a Numerical phantom

In this study, we used the realistic 4D-XCAT human torso phantom to model the patient body [SEG09][SEG10]. The phantom was used to create time-dependent activity and 511-keV attenuation maps for different tissues. This phantom was acquired from Duke University. The numerical voxelzed phantom includes highly detailed whole-body anatomies for adult males and females. The organs of this phantom were created using the Non-Uniform Rational Basis Spline (NURBS) technique. The 4D-XCAT phantom is provided as software written in the C programming language. Figure II.2 shows the anatomy of the 4D-XCAT phantom of males and females.

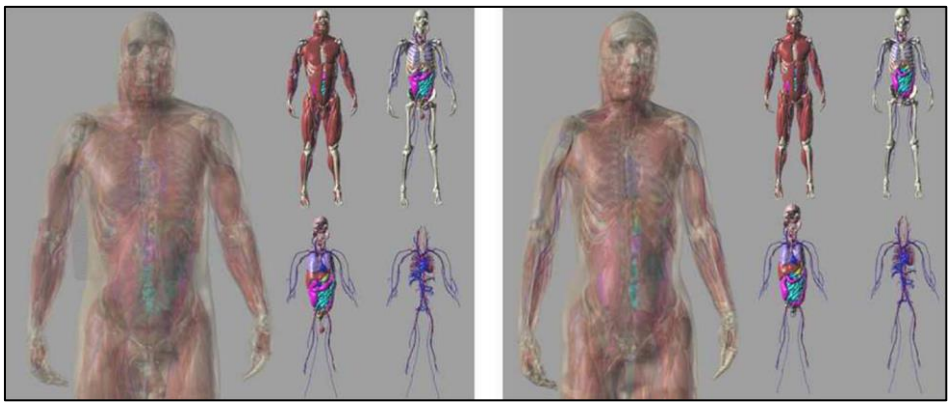

a **b**

Figure II.2: XCAT phantom anatomy at different levels of details: a. Male. b. Female [SEG 09].

Main phantom (body)

To produce the numerical phantom of the body, we ran the 4D-XCAT application with a parfile containing numerous parameters. These included parameters to define the sex, image and voxel size; photon energy used to define the attenuation coefficient; radionuclide activity concentrations for each organ for the activity phantom; and the start slice with the end slice defining the part of the body that we wanted to select for the study. In our study, we created a male XCAT phantom with an image matrix size of 256 × 256 pixels and 1200 slices. The voxel size was set to 2.5 × 2.5 × 2.5 mm^3. The radiotracer considered in this study was ^{18}F-FDG. The photon energy was set to 511 keV, which is the gamma energy of the photon emitted during the annihilation of the ^{18}FDG positron. The radionuclide activity concentrations for each organ were set to the values derived from the time activity curves

(TACS). Details of the calculation of these TACs are given in section (b). At the end, two types of body phantoms were created: activity and attenuation phantoms. While the activity phantom contains activity concentrations of ^{18}FDG, the attenuation phantom contains the attenuation coefficients of each tissue for an energy of 511 keV. These attenuation coefficients are determined based on the elemental composition of the tissues and the photon energy. We assigned a value ranging from 1 to 106 to each organ in the parameter file to identify organs in the phantom and facilitate the insertion of the activity concentrations in the organ voxels. In Figure II.3, we show the phantom generated without activity concentrations.

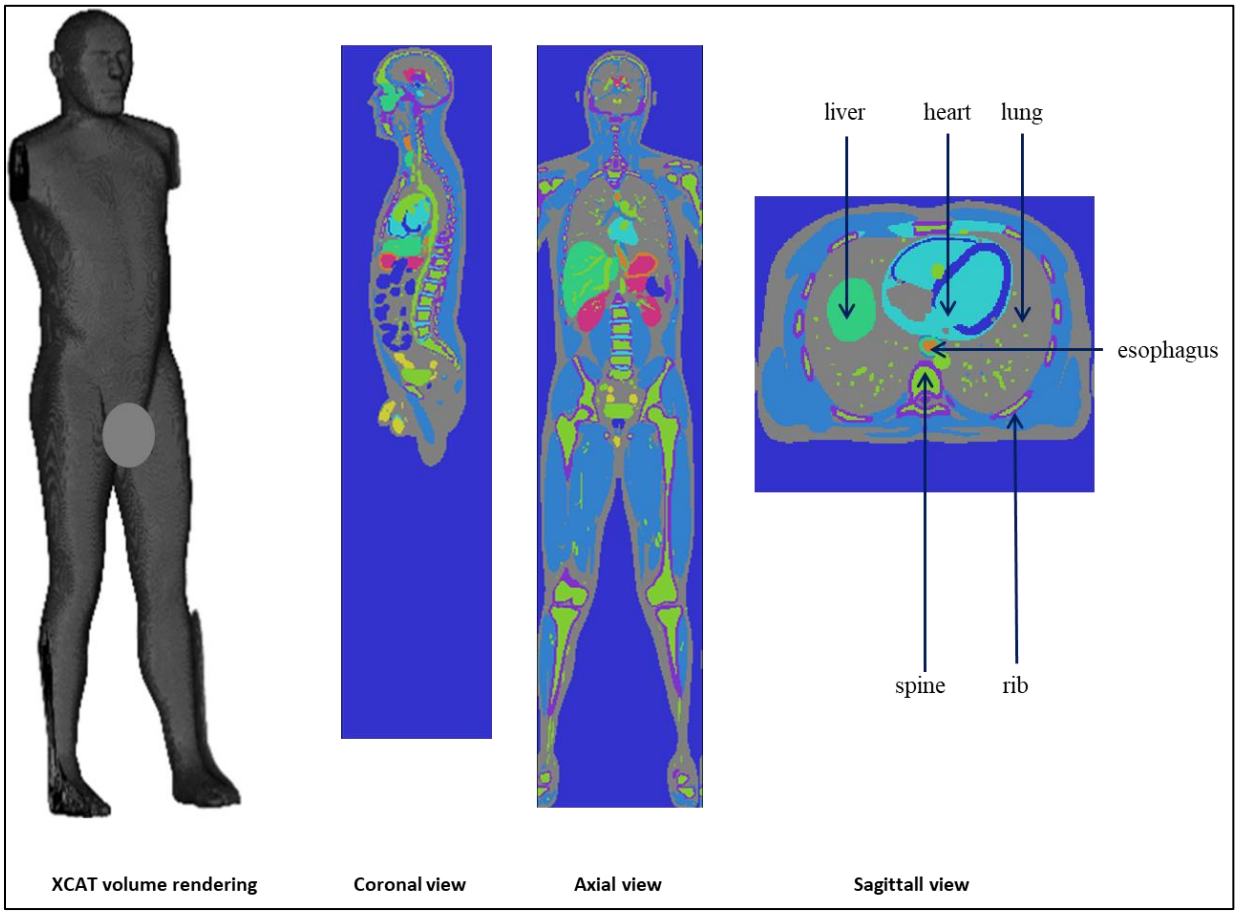

Figure II.3: XCAT phantom generated without activity concentrations.

Lesion

Concerning the creation of the lesion, we used the same parfile used to create the activity and attenuation phantoms of the body but with another mode. This mode allows the generation of the activity and attenuation phantom of the lesion. In the parfile, we defined the location and size of the lesion. With this version of the XCAT, lesions in the body can be modeled only as simple spheres (Figure II.4). In this study, we created a lesion 9 mm in

diameter in the liver. To do so, we selected the coordinates of a pixel belonging to the liver in the body phantom and set these coordinates to the location parameter of the lesion in the parfile.

Figure II.4: Model of the lesion used in this study.

The lesion created was added to the main phantom (body) in the liver. In Figure II.5, we illustrate transverse slices showing the liver before and after insertion of the lesion.

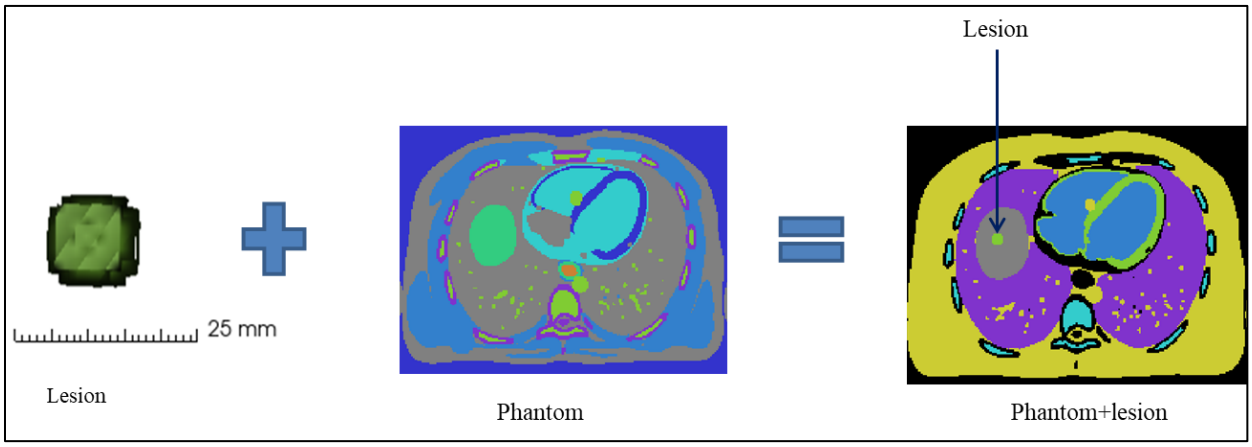

Figure II.5: Insertion of the lesion in the liver.

To facilitate the use of XCAT software for phantom production, lesion insertion and manipulation of all the data, we used a script developed in house in the MATLAB environment.

In the section below, we will detail the calculation of the TAC's and how the insertion of activity concentration was made.

II.1.1.b Generation of ^{18}F-FDG Time Activity Curves

To generate ^{18}F-FDG time-activity curves (TACs) for different organs and tumors, we first calculated the input function (IF), which represents the amount of ^{18}F-FDG in the blood.

The calculation was performed using the parametric function proposed by Feng [FEN93][FEN96]. The mathematical expression of this model is given as follows:

$$C_p(t) = (A_1 t - A_2 - A_3)e^{\lambda_1 t} + A_2 e^{\lambda_2 t} + A_3 e^{\lambda_3 t} \qquad \text{(II.1)}$$

With:

- λ_1 (min^{-1}), λ_2 (min^{-1}) and λ_3 (min^{-1}) are the eigenvalues of the model.
- A_1 (µCi/ml/min), A_2 (µCi/ml) and A_3 (µCi/ml) are the coefficients of the model.

The values of $\lambda_{1\to3}$ and $A_{1\to3}$ are reported in **Table I.1**.

A_1 (µCi/ml/min)	A_2 (µCi/ml)	A_3 (µCi/ml)	λ_1 (min^{-1})	λ_2 (min^{-1})	λ_3 (min^{-1})
851.1225	21.8798	20.8113	-4.1339	-0.1191	-0.0104

Table II.1. Parameters of the IF used in this study.

Once the IF was obtained, we calculated the TAC's of the organs/tissues listed in **Table II.1** using **a** standard 3-compartment model [SOK77]. A descriptive schema of this model is illustrated in Figure II.6.

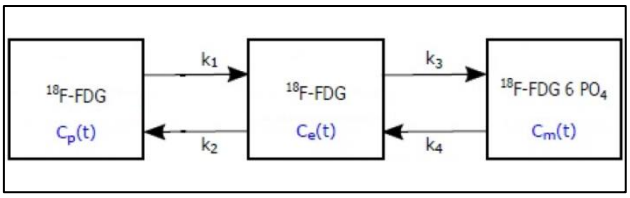

Figure II.6: Diagram showing the three-compartment model of ^{18}F-FDG uptake used.

Table II.2. The 18F-FDG kinetic microparameters and effective blood plasma volume V_p used for the different organs.

organs	k_1 (ml/min/ml)	k_2 (min^{-1})	k_3 (min^{-1})	k_4 (min^{-1})	V_p
kidney	0.2630	0.2990	0.0000	0.0000	0.4380
spleen	1.2070	1.9090	0.0080	0.0140	0.0000
liver	1.2560	1.3290	0.0020	0.0020	0.1650
marrow	0.4250	1.0550	0.0230	0.0130	0.0400
myocardium	0.1960	1.0220	0.1490	0.0100	0.5450
lung	0.1080	0.7350	0.0160	0.0130	0.0170
aorta	0.0000	0.0000	0.0000	0.0000	1.0000
soft tissue	0.0470	0.3250	0.0840	0.0000	0.0190
ventricle	0.0000	0.0000	0.0000	0.0000	1.0000
stomach	0.6140	1.8850	0.0710	0.0310	0.0630
tumor	0.1860	0.4380	0.3360	0.0000	0.0800

In the model used, $C_p(t)$ is the IF, which was already calculated; $C_e(t)$ and $C_m(t)$ are the concentrations of unmetabolized, metabolized and trapped ^{18}F-FDG in tumor cells, respectively, expressed in kBq/mL.

$k_{1\rightarrow4}$ are ^{18}F-FDG kinetic microparameters that describe the exchanges between the compartments.

- k_1 (min^{-1}) and k_2 (min^{-1}) represent the reversible exchanges of FGD between the blood and tissue compartments;
- k_3 (min^{-1}) represents the phosphorylation of the FDG ^{18}FDG-6-P_{O4};
- k_4 (min^{-1}) represents the effect of possible dephosphorylation of FDG-6-PO_4 to ^{18}F-FDG.

The values of these parameters, as reported in the literature, are presented in **Table II.2** [QIA11][DIM06].

The ^{18}F-FDG kinetics are described by the following differential equations:

$$\frac{dC_e(t)}{dt} = k_1 C_p(t) - (k_2 + k_3) C_e(t) + k_4 C_m(t) \quad \text{(II.1)}$$

$$\frac{dC_m(t)}{dt} = k_3 C_e(t) - k_4 C_m(t) \quad \text{(II.2)}$$

$$C_{FDG}(t) = C_e(t) + C_m(t) + V_p C_p(t) \quad \text{(II.3)}$$

$C_{FDG}(t)$ is the total concentration of ^{18}F-FDG in a region of interest (ROI). V_p represents the effective blood plasma volume contained in the ROI.

The activity concentrations of ^{18}F-FDG in each organ/tissue were calculated using a script implemented in the MATLAB environment.

II.1.1.c Frames generation

In this study, frames were defined as time series of the activity maps concerning the ^{18}F-FDG distribution in organs/tissues. To generate the frames, a real acquisition protocol was adopted. This protocol consists of 28 frames recorded during 55 min with the following repartition: 9x10s, 3x30s, 4x60s, 4x120s and 8x300s [WIEN02]. The procedure of frame generation, illustrated in Figure II.7**,** involves the following steps:

1. The ^{18}F-FDG activity concentration, C, was calculated from the TAC according to each frame time interval as follows:

$$C = \int_{frame\ start}^{frame\ end} \mathrm{C_{FDG}(t)}\, dt \qquad \text{(II.4)}$$

2. The activity concentration corresponding to the voxel volume was calculated.

3. The activity concentration was assigned for the voxels of each organ/tissue of the 4D-XCAT phantom.

The number and time of each frame are given in Table II.3. An in-house script implemented in the MATLAB environment was used to generate all the frames for all the ograns/tissues. All the frames generated are shown in Figure II.8.

Table II.3 Frame duration.

Frame number	Frame start (s)	Frame end (s)	Frame duration (s)
1	0	10	10
2	10	20	10
3	20	30	10
4	30	40	10
5	40	50	10
6	50	60	10
7	60	70	10
8	70	80	10
9	80	90	10
10	90	120	30
11	120	150	30
12	150	180	30
13	180	240	60
14	240	300	60
15	300	360	60
16	360	420	60
17	420	540	120
18	540	660	120
19	660	780	120
20	780	900	120
21	900	1200	300
22	1200	1500	300
23	1500	1800	300
24	1800	2100	300
25	2100	2400	300
26	2400	2700	300
27	2700	3000	300
28	3000	3300	300

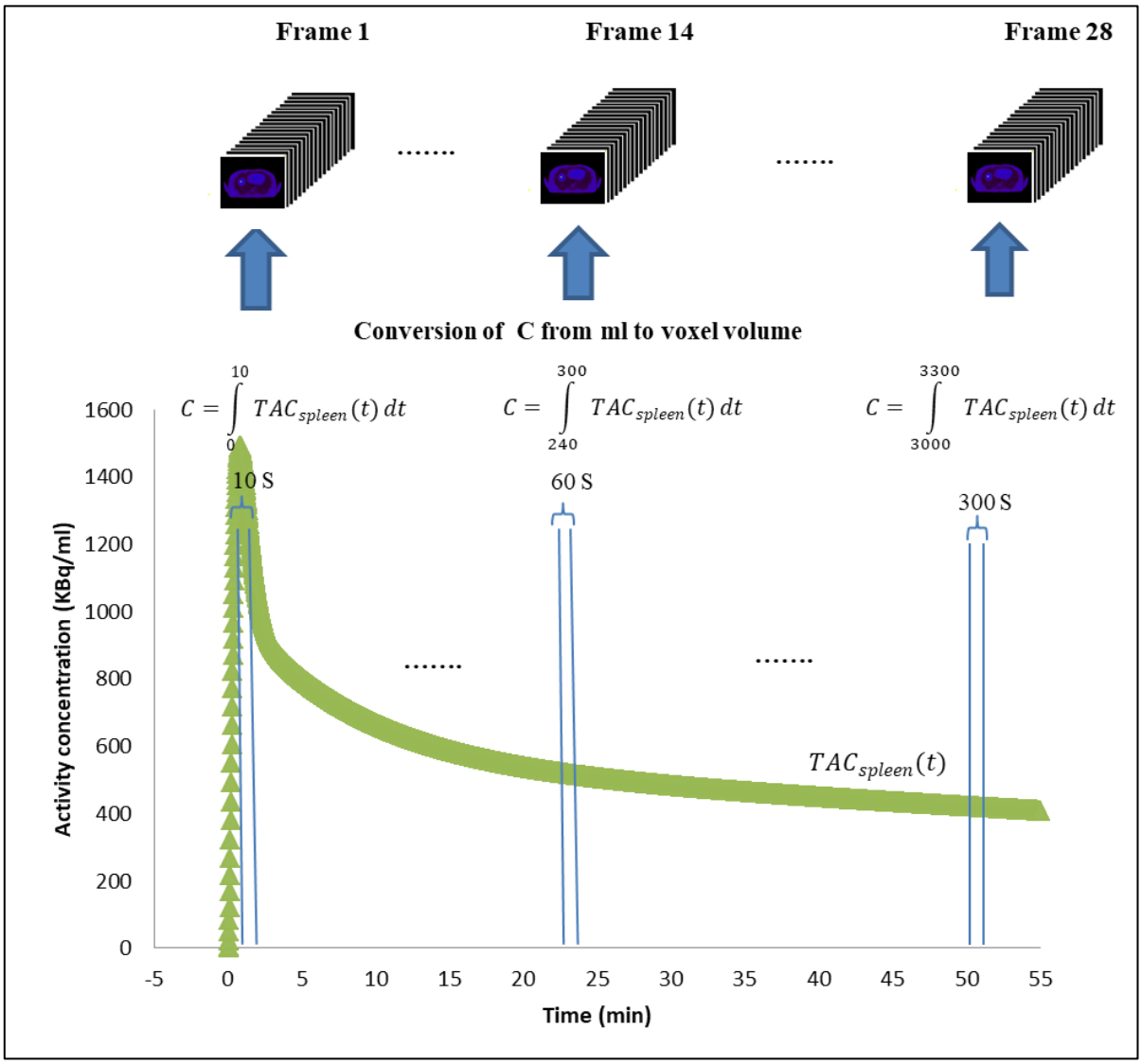

Figure II.7: Diagram showing the calculation and insertion of the ^{18}F-FDG activity concentrations in spleen voxels.

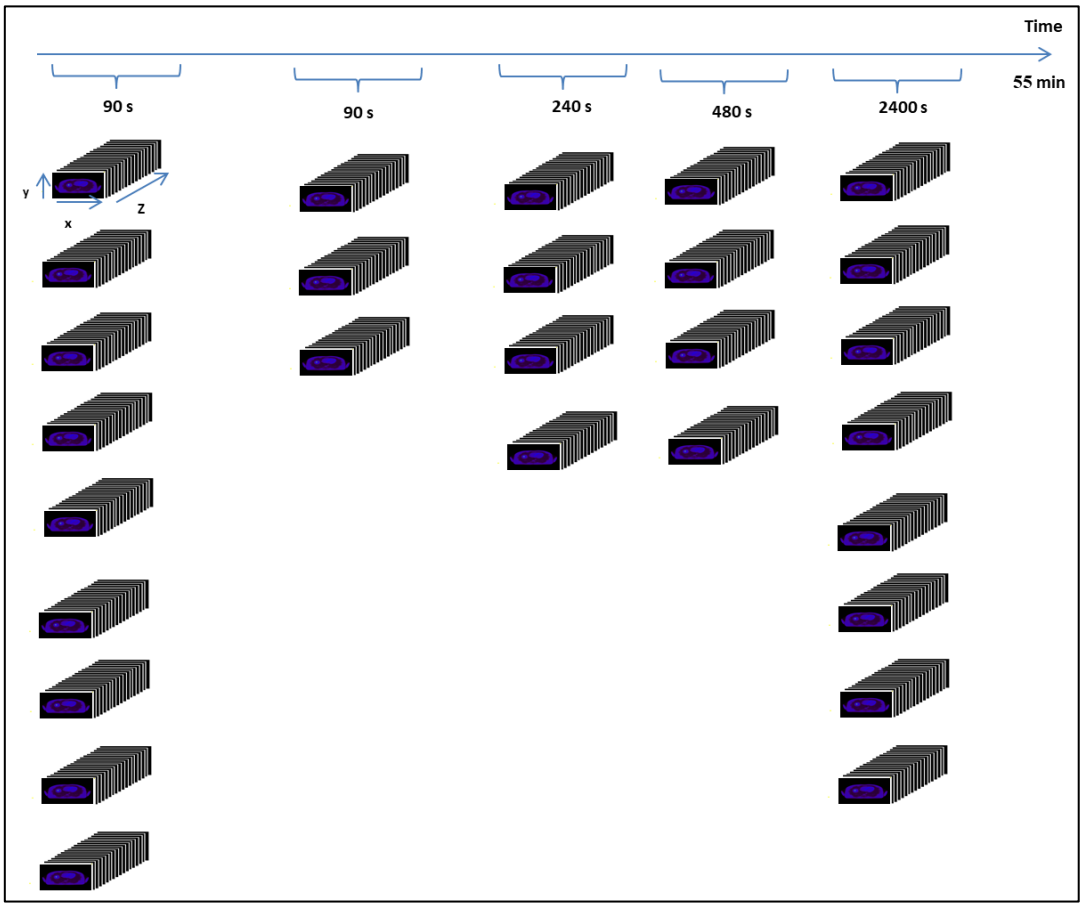

Figure II.8: Number of frames created at each time points.

Each frame was then forward projected and reconstructed using STIR reconstruction software.

II.1.2 Scanner geometry and image reconstruction procedure

The General Electric (GE) Discovery PET/CT 710 scanner model, implemented in STIR software [THI12], was considered in this study. The characteristics of the scanner considered are given in Table II.4 [YOO15].

Table II.4. Characteristics of GE Discovery PET/CT 710.

Number of rings	24
Number of detectors per ring	576
Inner ring diameter (cm)	81.02
Average depth of interaction (cm)	0.94
Distance between rings (cm)	0.654
Number of blocks per bucket in transaxial direction	2
Number of blocks per bucket in axial direction	4
Number of crystals per block in axial direction	6
Number of crystals per block in transaxial direction	9
Number of detector layers	1
Number of crystals per singles unit in axial direction	1
Number of crystals per singles unit in transaxial direction	1

For the reconstruction procedure, we used STIR version 4.0.0-alpha software. The STIR ray-tracing technique was utilized to perform forward projection of the activity maps to generate free-noise sinograms using parameters that define the geometry of the scanner, as cited in **Table II.4**. The generated free-noise sinograms were corrected for attenuation effects using attenuation coefficients calculated from the 4D-XCAT attenuation map. Subsequently, Poisson noise was added to obtain noisy sinograms that were reconstructed using Ordered Subsets-Maximum A posteriori Probability-One Step Late (OSMAPOSL) algorithm with 35 iterations and 1 subset. The same reconstruction procedure was applied to all frames, resulting in a total of 28 frames simulating single-bed dynamic ^{18}F-FDG PET images. The reconstructed image matrix was 256 × 256 pixels, and the voxel size was 2.5 × 2.5 × 2.5 mm^3. The number of slices covering the liver region is 81 slices.

The steps of the reconstruction procedure are shown in Figure II.9.

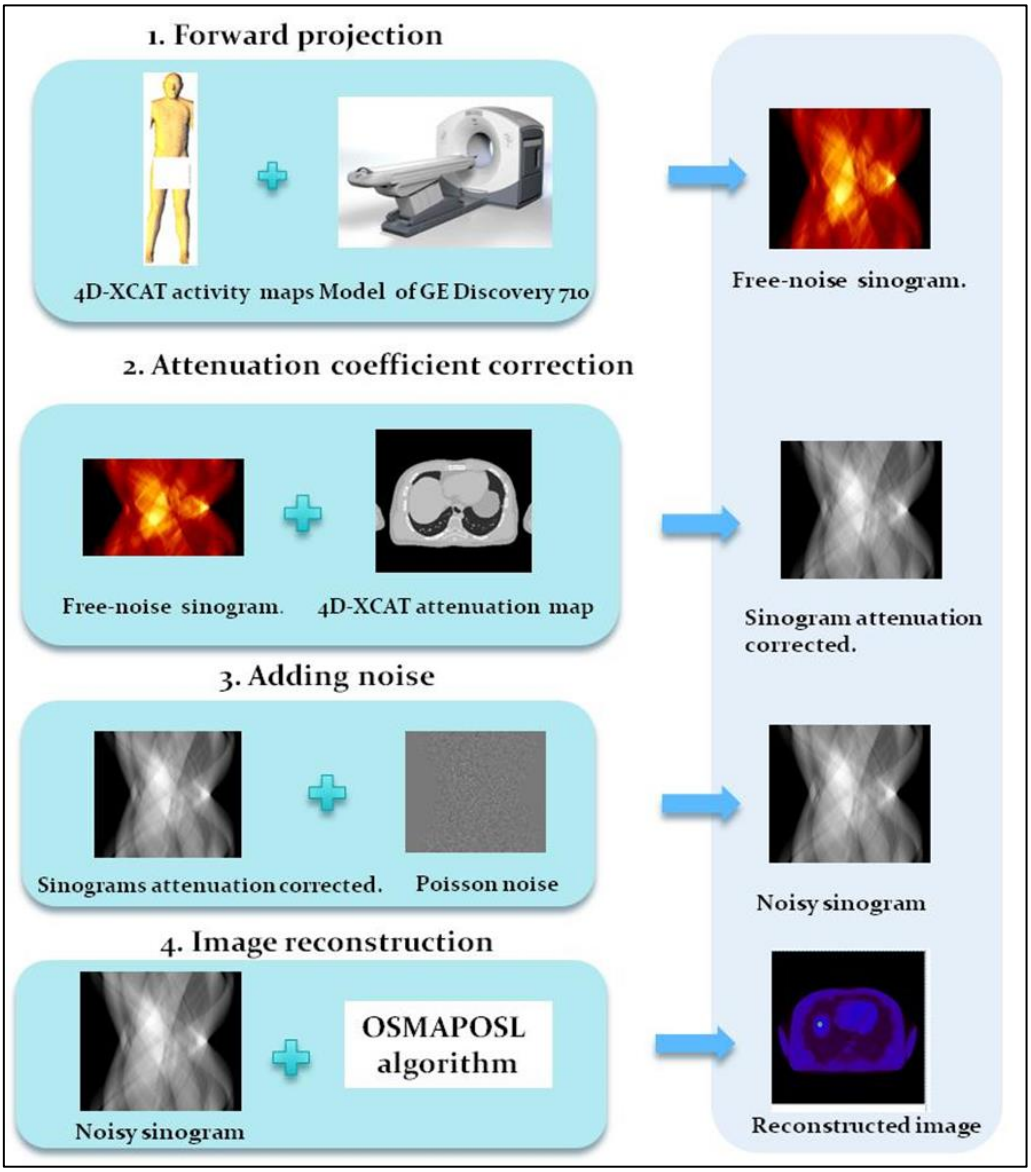

Figure II.9: Workflow showing the steps followed in the reconstruction procedure.

We implemented and used a MATLAB script to handle and connect all the STIR functions and executable files (.exe), from the forward projection to the reconstruction. The script was run on a HP Z8 64 workstation in parallel computing using the PARFOR loop. The workstation used, powered with Windows 10, is equipped with 20 physical CPUs, an Intel© Xeon© Silver 4210 CPU @2.20 GHz, 64 GB of RAM, and an NVIDIA Quadro P400 graphics card with 2 GB of RAM.

The qualitative and quantitative evaluations of the reconstructed images were performed using 3D slicer open source software.

II.2 Results

II.2.1 Calculation of the input Function and time activity curves

The input function obtained using equation II.1 and the parameters values reported in Table II.1, is given in Figures II-10. The TAC of 11 tissues modeled in the 4D-XCAT phantom were generated, assuming the standard 3-compartment model, the calculated input function and kinetic physiological parameters of the ^{18}F-FDG. The generated TAC's are illustrated in Figure II-11.

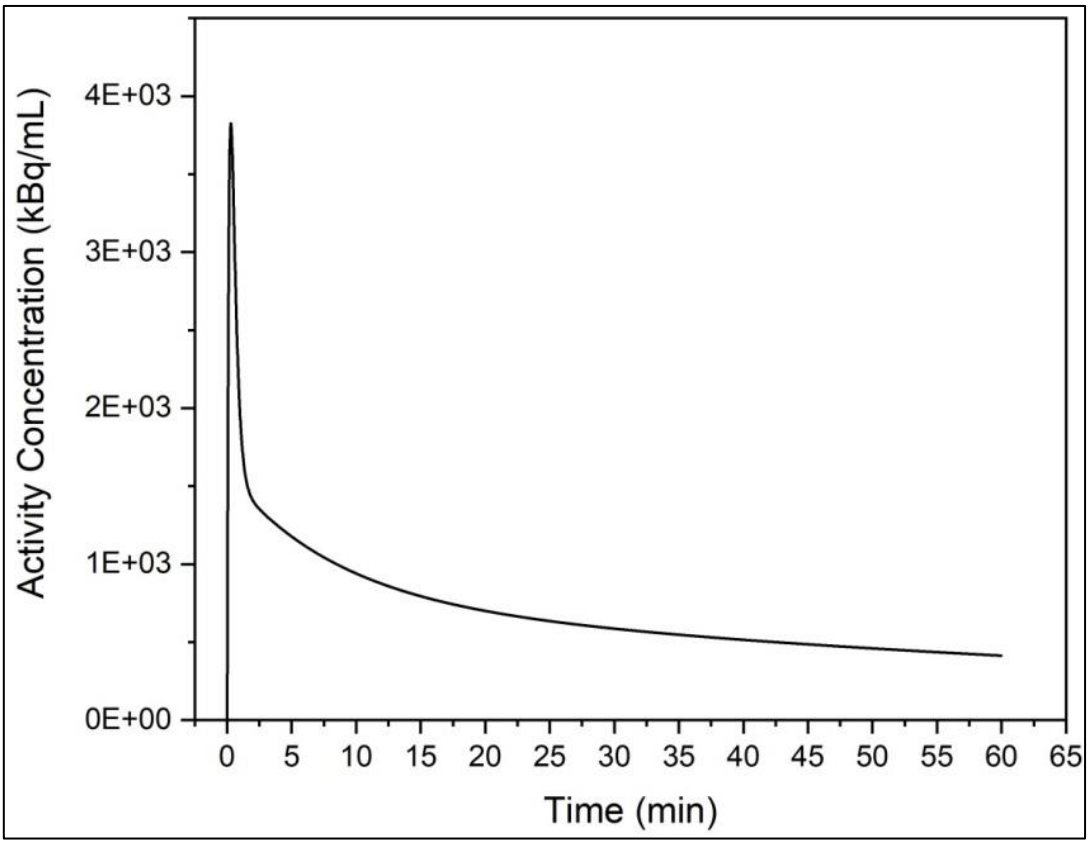

Figure II-10: ^{18}F-FDG input function used in this study.

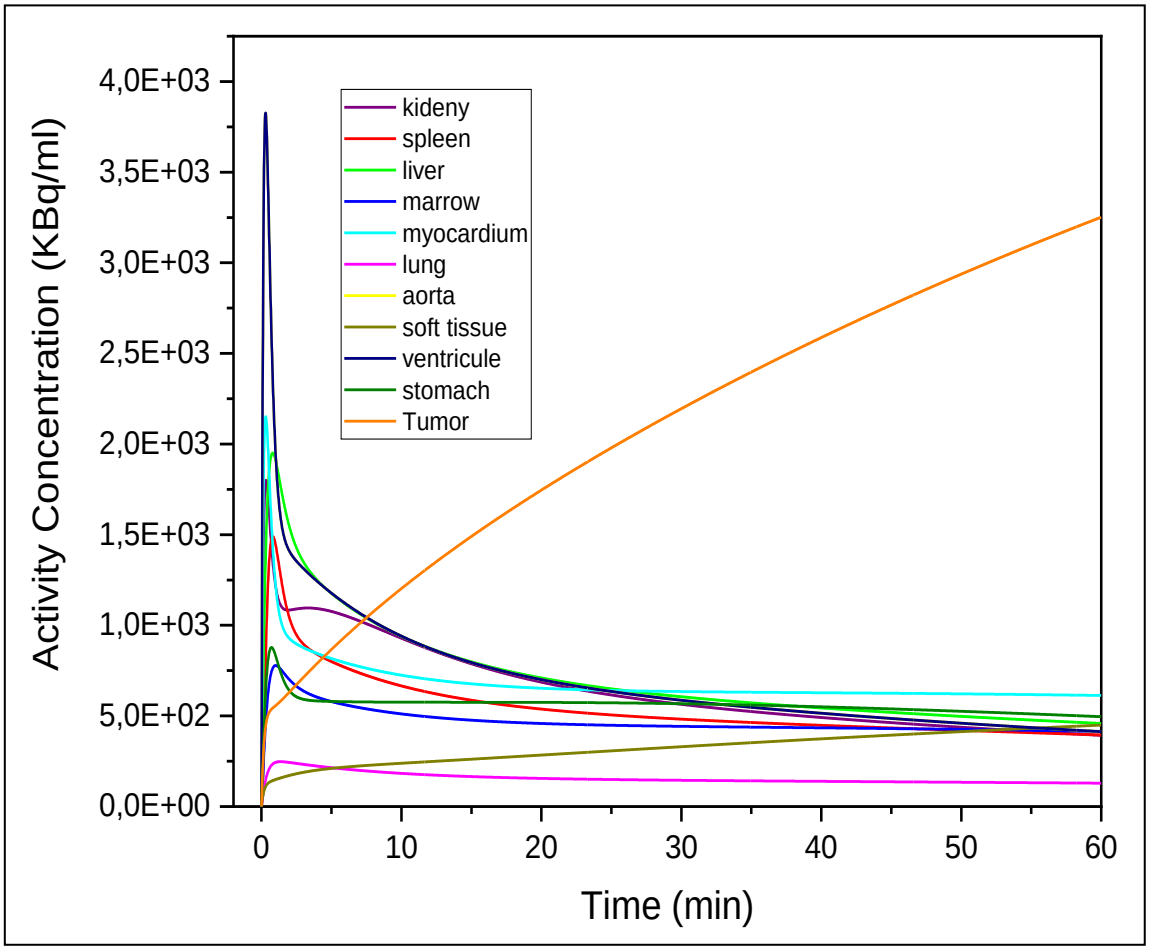

Figure II-11: TAC's of ^{18}F-FDG generated in different tissues.

In Figure II.11, the simulated TAC's curves of the phantom tissues clearly show tracer uptake and clearance, while the TAC of the tumor reveals continuous tracer trapping. This behavior is correlated with the constant values k_3 and k_4 , as deduced from Table II.2. The TAC's derived for the ventricles and the aorta are similar and evidently, reproduce the behavior of the IF since all the kinetic microparameters of these organs are equal to zero and the effective blood plasma volume is equal to one. A comparison of the calculated TAC's to those published [KAR11] showed good agreement.

The TAC's obtained were subsequently used to generate ^{18}F-FDG dynamic activity maps.

II.2.2 Generation of dynamic activity maps and attenuation map using TAC's calculated and the XCAT phantom

In Figure II-12, we illustrate selected transverse slices at the lesion level of all the frames of the dynamic activity maps. For more details, transverse, coronal and sagittal slices selected from the 1st, 17th and 28th frames of the ^{18}F-FDG activity maps are shown in Figure

II-13. These slices were selected to show the effect of the reconstruction procedure when the activity concentration in the lesion was lower than, equal to or greater than that in the background (liver). The attenuation map, which contains the attenuation coefficients of the XCAT tissues for gamma rays of ^{18}F-FDG, is given in Figure II-14.

Figure II.12 shows the distribution of the ^{18}F-FDG concentration in different tissues and at different time points. For more details, in Figure II.13, as expected, the activity is highest in the ventricles and the aorta, as shown in the images of frame 1. The lesion appears as a cold spot because at this step, the tumor has lower activity than the surrounding tissue. In the case of the image selected from frame 17, the lesion could not be recognized because the activities in the tumor and in the liver were almost the same. However, the tumor can be accurately detected in frame 28, where ^{18}F-FDG trapping is high and irreversible.

II.2.3 Generation of dynamic ^{18}F-FDG PET images

The whole generated frames of activity maps were forward projected and reconstructed using an in-house script connecting STIR functions. An example of the projection data of frame 28 is shown in figure II-15**.**

The reconstructed images of those shown in figure II-13 and II-14 are displayed in figure II-16 and II-17, respectively. Each frame contained 47 slices.

Figure II.13 and Figure II.17 show that the qualitative comparisons reveal that the images before and after reconstruction are very similar. However, the lesion not clearly apparent in frame 17 since the lesion and liver activity values were close, can be not seen in the corresponding reconstructed image. This is due to the technical limitations of the scanner model used in this study.

II.2.4 Quantitative and qualitative analysis

The quantitative analysis of the reconstructed images was performed via the calculation of the profiles line traced on a transverse slice at the lesion level of the images illustrated in Figures II-13 and II-17. Figure II-18 shows the line profiles obtained.

In Figure II.18, we can observe that the voxel intensities of the transverse images before and after the reconstruction procedure are almost the same. The qualitative and quantitative comparisons demonstrated the efficiency of the reconstruction procedure performed in the present study.

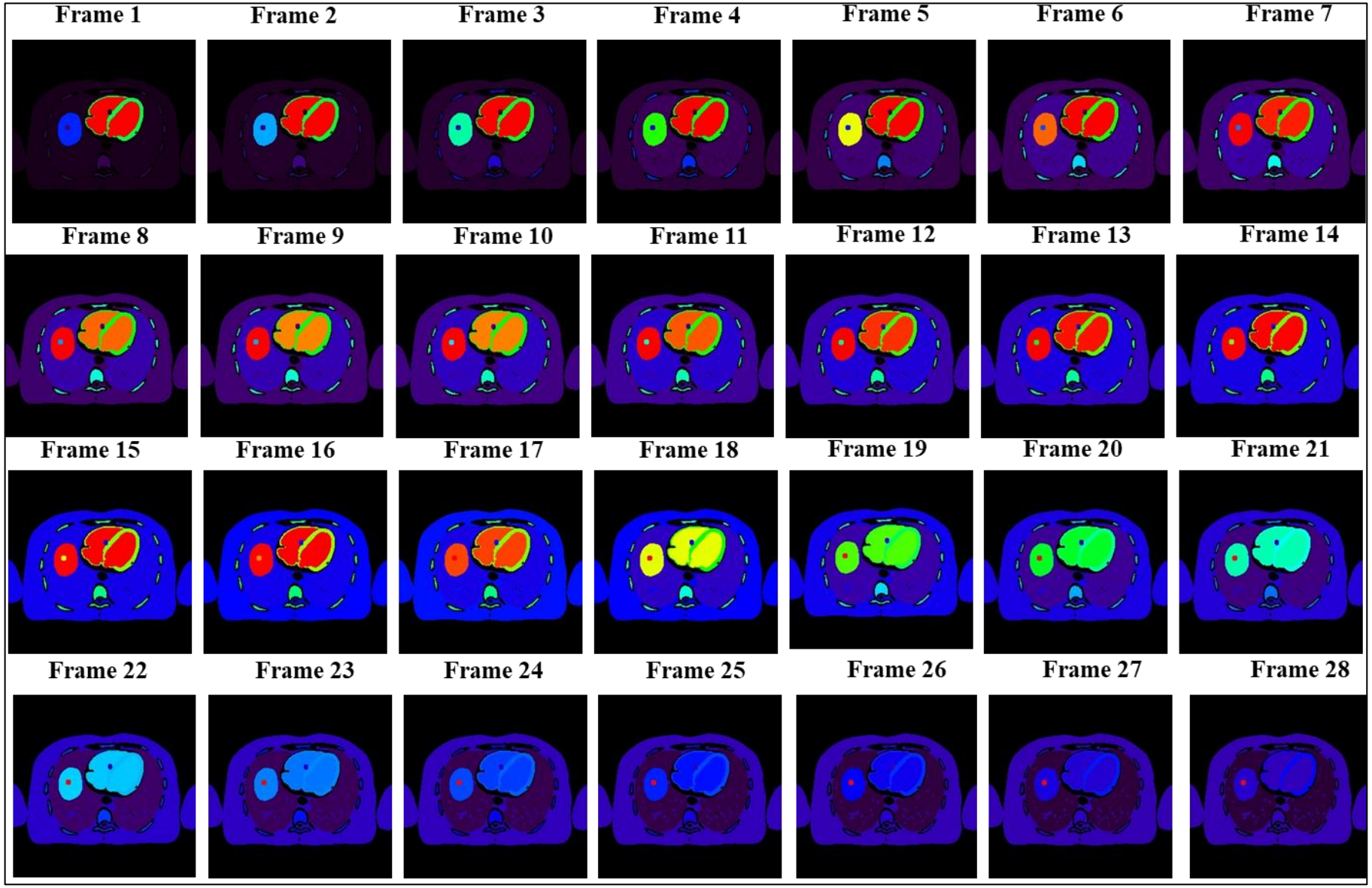

Figure II.12: Transverse slices at the liver level selected from all frames of the activity maps showing the distribution of the concentration of ^{18}F-FDG in the lesion and other tissues.

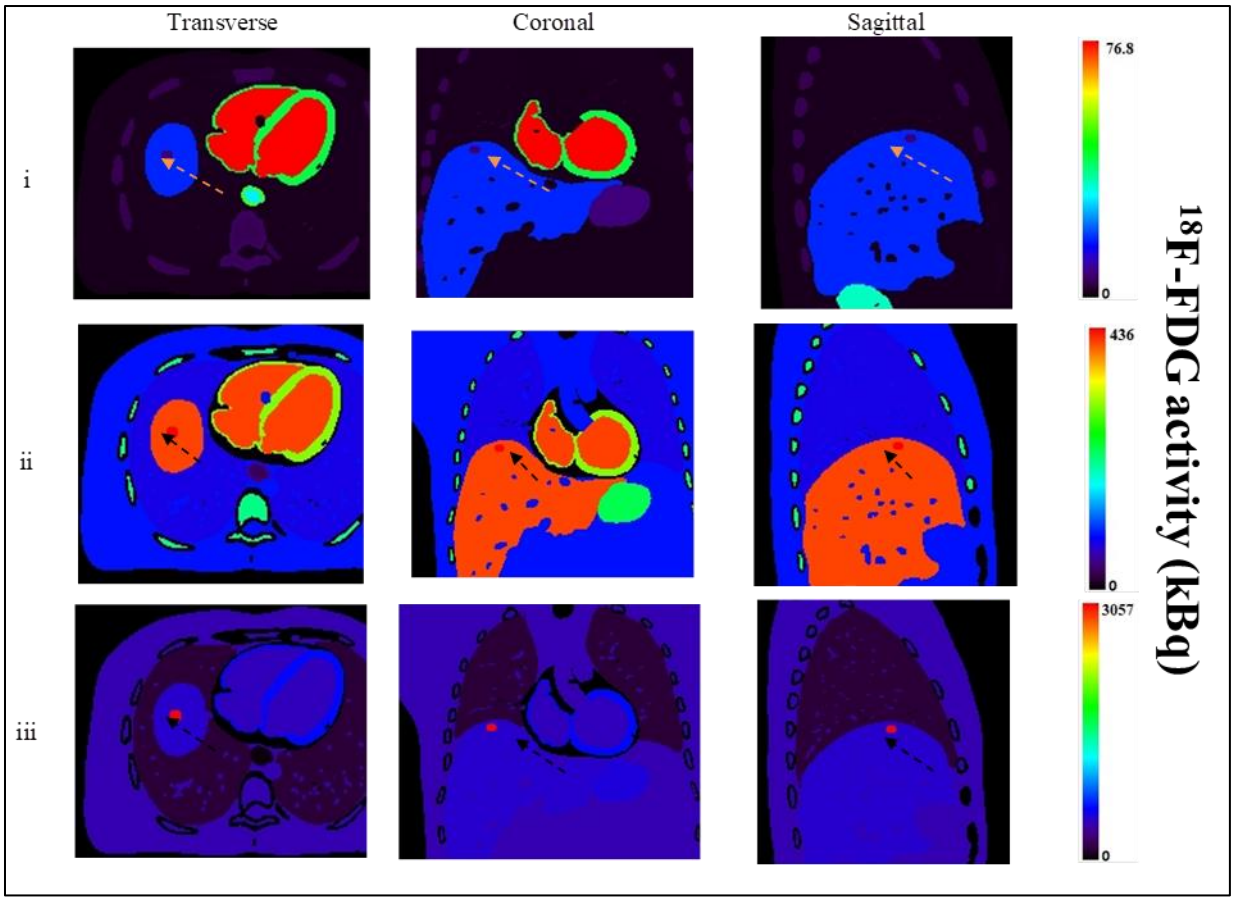

Figure. II-13: Transverse, coronal and sagittal images of ^{18}F-FDG activity maps taken at 3 different time points corresponding to : i = frame 1, ii = frame 17 and iii = frame 28. The arrow shows the lesion inserted in the liver.

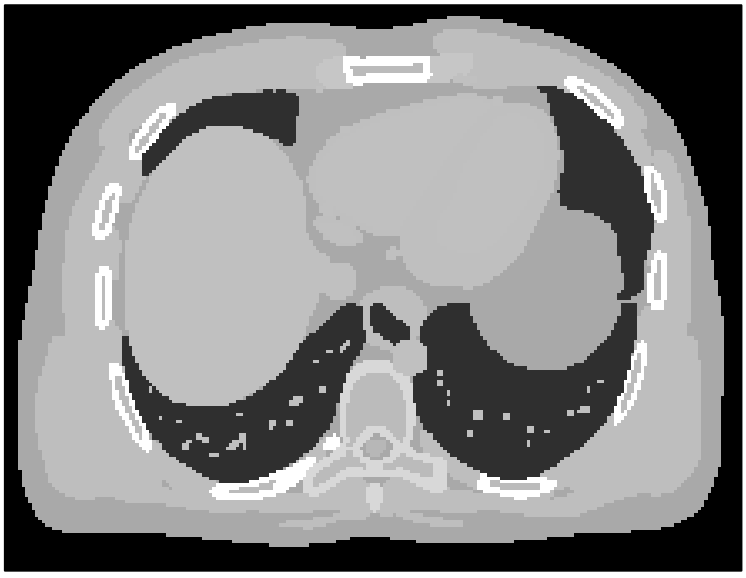

Figure II-14: Transverse slice of the attenuation map of the XCAT phantom for ^{18}F-FDG.

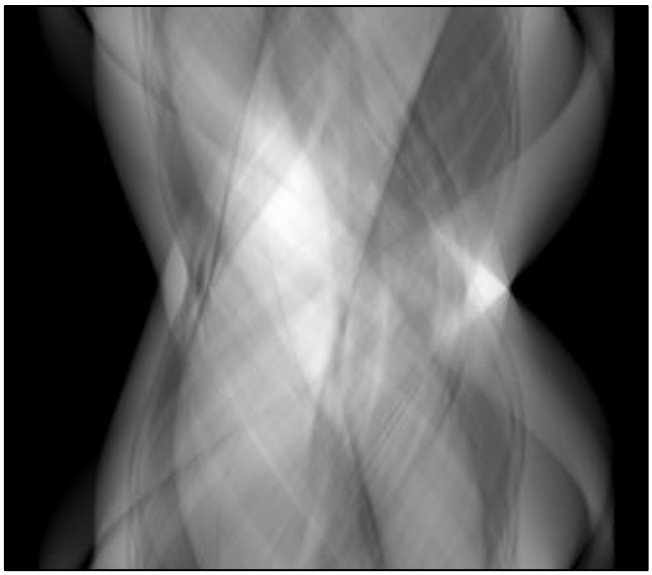

Figure II.15: A sinogram of the activity map of frame 28 obtained during the forward projection step using the Discovery PET/CT 710 scanner model.

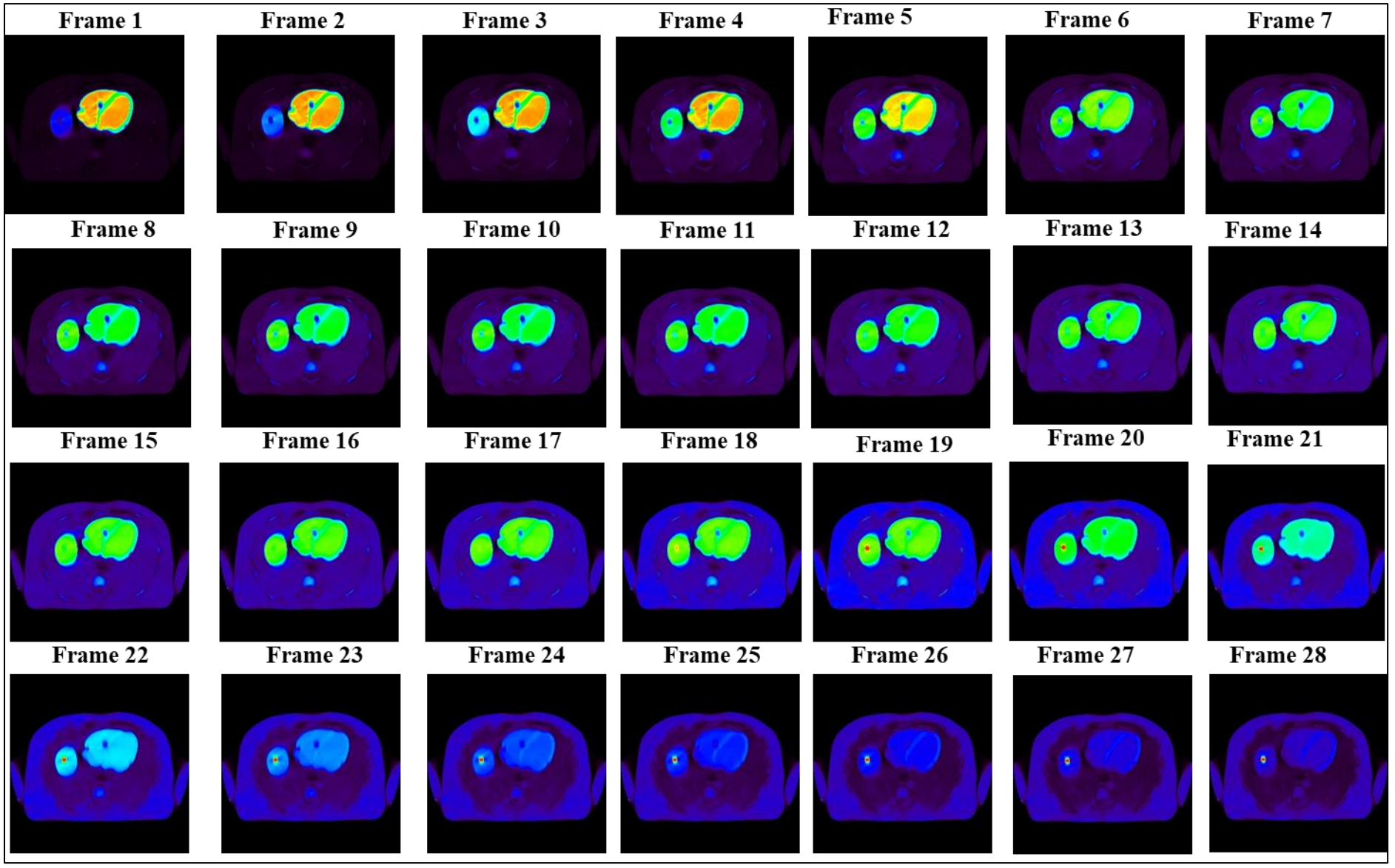

Figure II.16: Reconstructed transverse slices of all the frames of the activity maps showing the lesion in the liver.

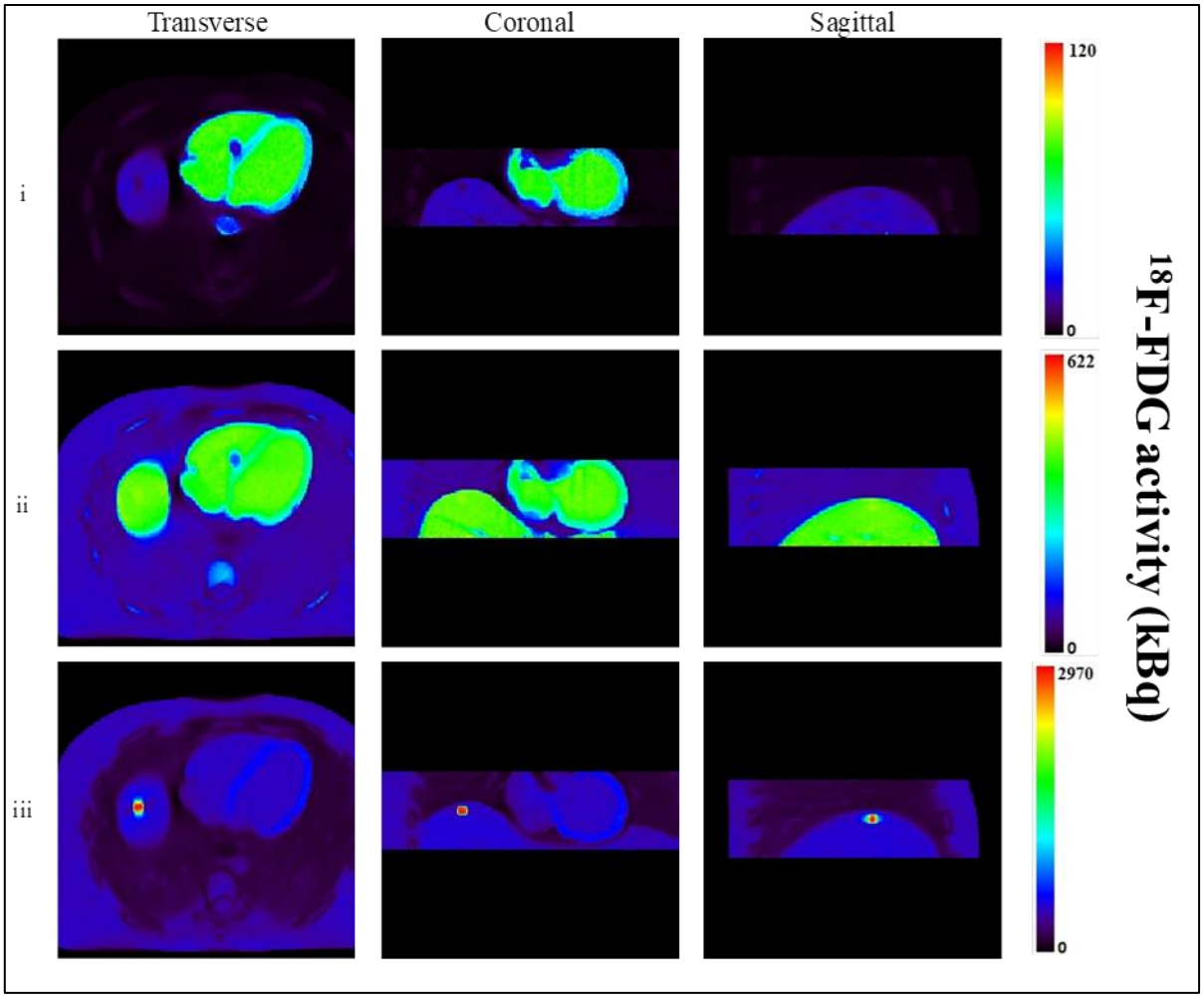

Figure II.17: Transverse, coronal and sagittal reconstructed ^{18}F-FDG PET images taken at 3 different time points corresponding to i = frame 1, ii = frame 17 and iii = frame 28.

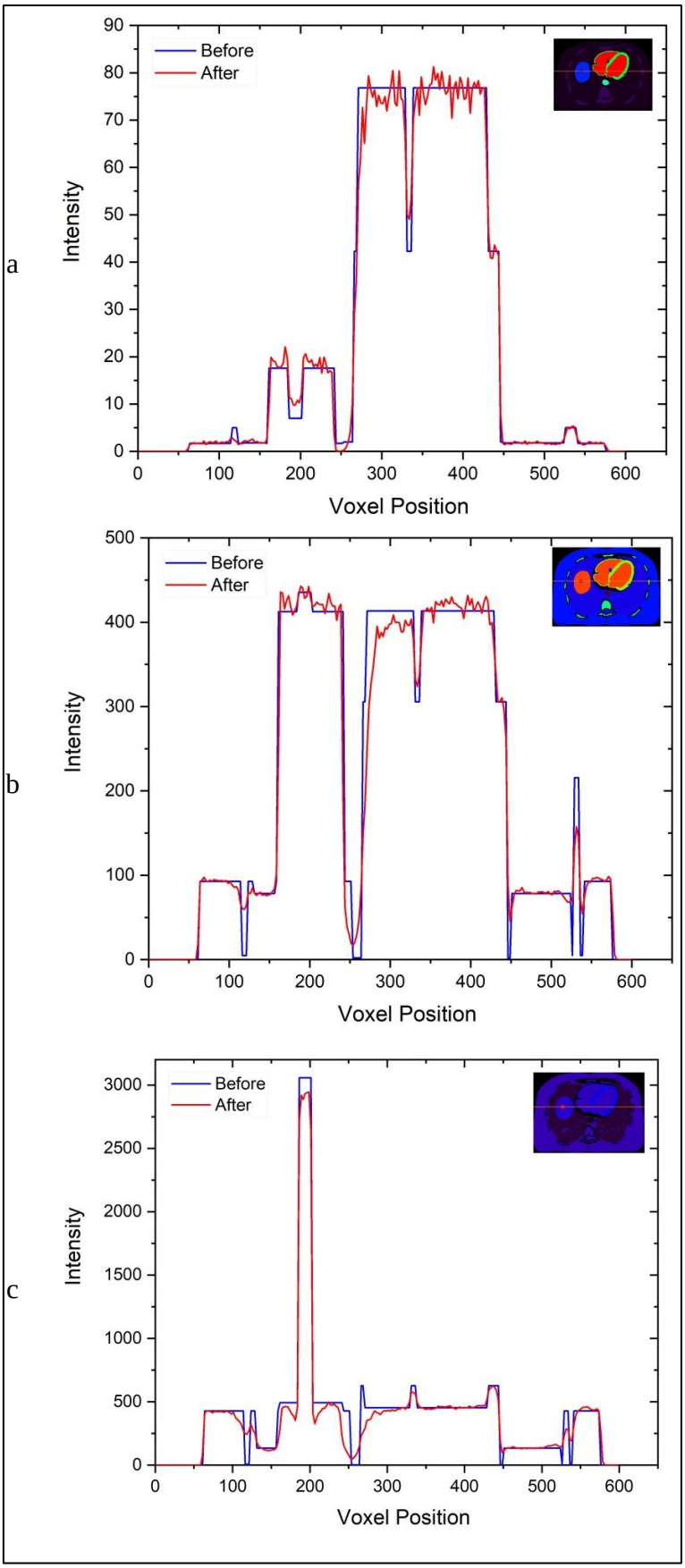

Figure II.18: Line profiles through a transverse slice of the 4D-XCAT phantom before and after reconstruction: (a) frame 1, (b) frame 17, and (c) frame 28.

In the following paragraphs, we demonstrate the application of the PCA to improve lesion detectability in ^{18}F-FDG PET images and reduce the data acquisition time.

II.3 Discussion

Notably, dynamic ^{18}F-FDG PET image simulation using a 4D-XCAT phantom with kinetic modeling and real patient clinical data differ in several ways. First, images from the 4D-XCAT phantom and kinetic modeling simulations aim to replicate realistic human anatomy and physiology, but they are still computer-generated and may not fully capture the complexity of real patient data. Real patient data are obtained from actual patient scans and thus reflect the variability and diversity of real-world patients. Second, simulation methods can control the level and type of noise and artifacts present in images, whereas real patient data may contain various types of noise and artifacts due to patient motion, scanner hardware, or other factors. Patient-specific characteristics such as age, body size, and comorbidities can significantly affect the results of PET imaging. Simulation methods may not fully replicate these characteristics and the associated variability that is present in real patient data. Finally, the experimental conditions for the 4D-XCAT phantom and kinetic modeling simulation were controlled and standardized, whereas real patient data may vary in terms of the radiotracer dose, uptake time, and imaging parameters.

Despite these differences, 4D-XCAT phantom and kinetic modeling simulations can be useful for understanding the underlying physics and limitations of PET imaging and for developing and testing imaging algorithms and techniques. Real patient data, on the other hand, are essential for clinical decision-making and patient care and provide a more comprehensive understanding of the disease process and the effects of treatment.

Many studies were recently undertaken on the interest of dynamic ^{18}F-FDG PET simulation and kinetic modeling such as that of Dimitrakopoulou-Strauss et al. [DIM21-a]. This last study focused on the use of kinetic modeling and parametric imaging with dynamic PET for oncological applications, which is a broader topic than just lesion detectability investigations. Our work reinforces and supports the main findings of Dimitrakopoulou-Strauss et al. study and resolves some mentioned problems such as the problem of time-consuming. Indeed, Dimitrakopoulou-Strauss et al. reported that kinetic modeling and parametric imaging can be used to improve lesion detectability in oncological PET imaging. Similarly, both the 4D-XCAT phantom and kinetic modeling approaches have been shown to

be effective at detecting lesions in dynamic ^{18}F-FDG PET images. In terms of quantitative accuracy, Dimitrakopoulou-Strauss et al. emphasized the importance of quantitative accuracy in oncological PET imaging. Dimitrakopoulou-Strauss et al. also discussed the computational complexity of kinetic modeling, which can be time-consuming and require significant computing resources. Similarly, the 4D-XCAT phantom approach can be computationally intensive.

The comparison between research works as our actual one on dynamic ^{18}F-FDG PET images simulation using 4D-XCAT phantom and kinetic modeling for lesion detectability investigation is more focused on a specific application of some simulation and kinetics methods. However, all undertaken studies highlight the importance of quantitative accuracy and the computational complexity of these approaches. Indeed, different used methods have been shown to be effective in detecting lesions, with some studies reporting similar lesion detectability. However, there have been some reports of differences in lesion detectability depending on factors such as lesion size and location.

The data generated through this work can be used to study the reduction of the total duration of data acquisition in dPET while preserving the detectability of lesions by applying multivariate image analysis techniques such as principal component analysis (PCA). This could be investigated by extracting relevant images from the simulated dynamic imaging sequences that provide a lesion detectability level similar to that of the usual static images acquired at 35 min postinjection. Full-length and shorter dynamic sequences can be analyzed both qualitatively and quantitatively to demonstrate the potential of the proposed methodology. Other methods for reducing the total duration of dynamic PET imaging with ^{18}F-FDG include sparse sampling schemes, multiparametric image reconstruction, and deep learning-based techniques. However, these methods are still in the early stages of development and require further validation before they can be routinely used in clinical practice.

Even though we considered in this work only one lesion in the liver, the findings could be easily extended to include lesions with different shapes and concentrations in various locations. The effect of respiratory motion on the reconstructed images will also be considered.

Conclusion

The methodology outlined in this chapter provides a comprehensive framework for the simulation of dynamic ^{18}F-FDG PET images. The subsequent sections offer detailed implementation steps, from the calculation of the IF to the generation of ^{18}F-FDG PET images. We demonstrated the use of a 4D-XCAT phantom and kinetic modeling is central to generating these dynamic images.

Furthermore, in this chapter, we provided findings concerning the calculation of IF and time-activity curves (TACs), the generation of dynamic activity maps and the simulation of ^{18}FDG-PET images. We also presented our results on comparisons between activity maps and ^{18}F-FDG-PET images to evaluate the reconstruction procedure adopted in this study.

The results obtained were used in the following chapter to evaluate the potential enhancements that can be achieved by using the PCA method in terms of lesion detectability and scanning time.

The findings of this chapter were published in [BEZ23].

Chapter III:
Enhancement of lesion detectability and optimization of scanning time

Introduction

This chapter delved into the generation of images using principal component analysis (PCA) and SUM methods from reconstructed frames of dynamic ^{18}F-FDG PET images. The generated images were investigated to study the enhancement of lesion detectability and scanning time optimization.

The following sections detail the generation of the images and discuss the results of the application of PCA to simulated dynamic ^{18}F-FDG PET images.

III.1 Generation of PCIs and SUM images

III.1.1 Principal component analysis

As defined in chapter I, PCA serves as a method for examining the variance–covariance or correlation structure within a multivariate dataset, aiming to simplify and condense its dimensions. This process involves computing transformation vectors known as Principal Components (PCs), which define the directions of the maximum variance within the multifeature space.

In this study, we applied the PCA method to the reconstructed frames of dynamic ^{18}F-FDG PET images to generate Principal Component Iimages (PCIs). The calculation process is based on several steps, as illustrated in Figure III.1.

First, we arranged the intensities of the voxels of each image of the same frame in the rows of the matrix Z. The rows are the variables of the matrix. In the example shown in Figure III.1**,** m, which represents the number of frames, equals 28, and n is the number of voxels in each frame (n=256x256x47). The voxel intensities represent the activity concentrations of ^{18}F-FDG.

$$Z = \begin{bmatrix} z_{1,1} & \cdots & z_{1,n} \\ \vdots & \ddots & \vdots \\ z_{m,1} & \cdots & z_{m,n} \end{bmatrix} \qquad \text{(III.1)}$$

Then, before the application of PCA, we preprocessed the data contained in matrix Z to transform these data into a more suitable form for analysis. We performed two types of preprocessing on the data: “scaling to unit variance” and “mean centering”.

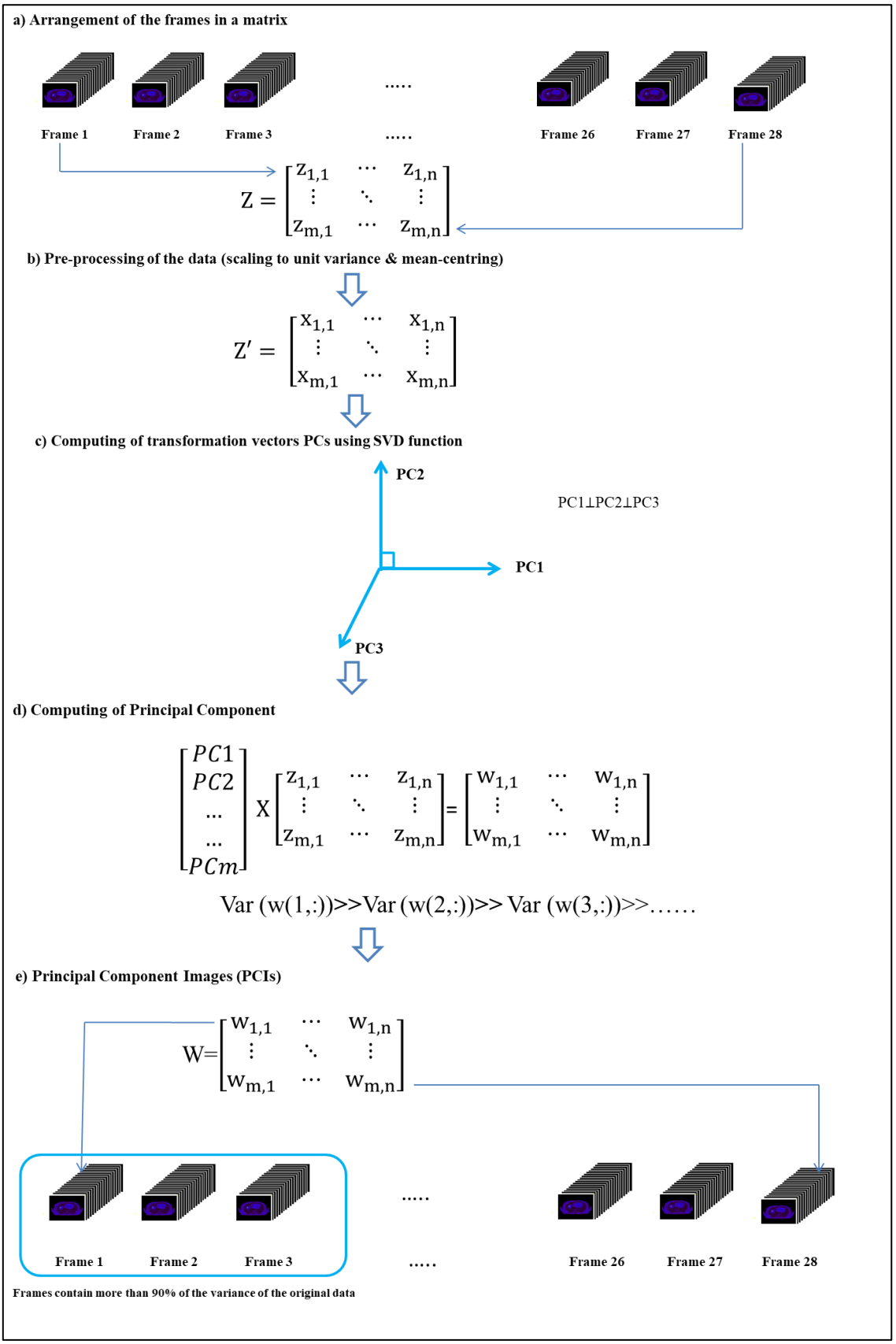

Figure III.1: Flowchart showing how to create principal component images.

In the scaling to unit variance, we normalize the magnitude of variance present in the variables. The reason is that the variables often possess notably varied ranges, and the PCA could be influenced more by the variable that has the largest range. In the second preprocessing step, mean-centering, we adjusted the rescaled dataset to create a new dataset where the mean value of each variable became zero. We used the following expression to preprocess the data:

$$x_{ij} = (z_{ij} - \bar{z}_j)/s_j \qquad \text{(III.2)}$$

where

- z_{ij} and x_{ij} are the original and final values of voxel i (i=1...n) of frame j (j=1...,m), respectively.
- $\bar{z}_j$ and s_j are the mean and the standard deviation of the jth row of the original data Z matrix, respectively.

In the new preprocessed data, no variable dominates over the others, and the matrix Z becomes

$$Z' = \begin{bmatrix} x_{1,1} & \cdots & x_{1,n} \\ \vdots & \ddots & \vdots \\ x_{m,1} & \cdots & x_{m,n} \end{bmatrix} \qquad \text{(III.3)}$$

Once the data were preprocessed, we calculated the transformation vectors or the principal component axes (PCs) using the SVD function. The PCs obtained are orthogonal since the condition Cov (PC(i), PC(j)) = 0, with i≠j, is verified. The PCs explain the magnitude of the variance in decreasing order, as shown in Figure III.1. We found that 100% of the total variance in the original data can be accounted for by the first three principal component axes, as shown in Figure III.2. Therefore, the remaining components are rejected without loss of useful information. Hence, in this work, we considered only the first three principal components.

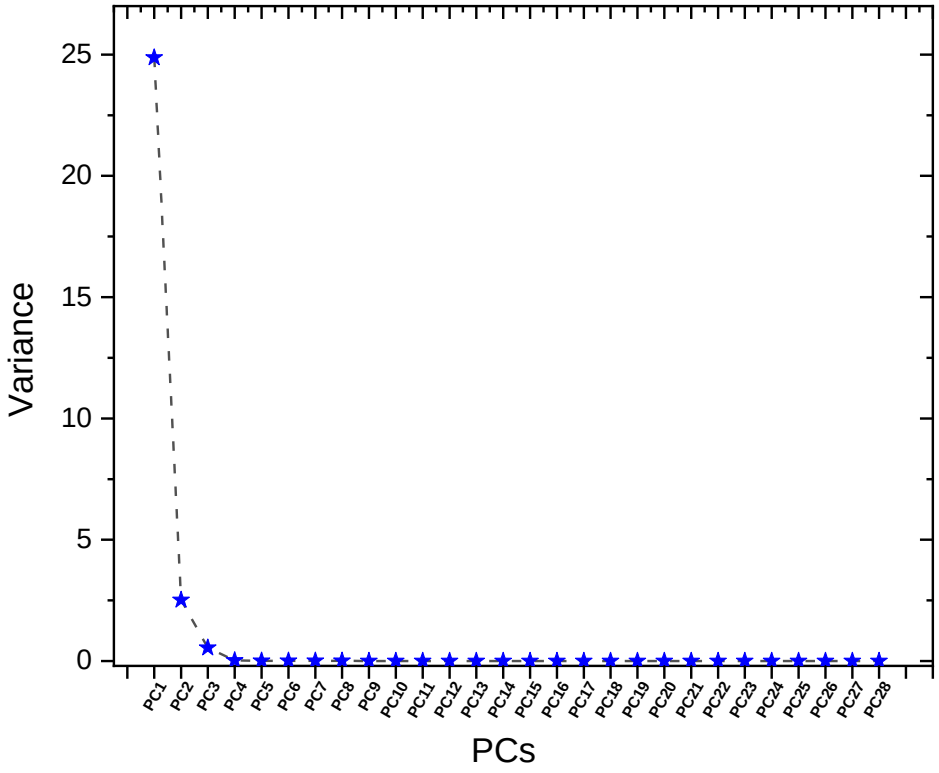

Figure III.2: Variance accounted for the PCIs.

Each element within the PCs is utilized as a weight factor to create a principal component, with Var (w(1,:))>>Var (w(2,:))>> Var (w(3,:))>>……

Var (w(i,:)): the variance of Principal Component number I, with i=1:28.

In this example, Var (w(1,:)) = 24.87, Var (w(2,:)) = 2.52, Var (w(3,:)) = 0.5, and

Var (w(i,:)) <<0, with i = 4:28.

Finally, the principal component created can be visualized as images. We call the generated images; Principal Component Images (PCIs).

For comparison purposes, we also applied the summation method to the same reconstructed dynamic ^{18}F-FDG PET images at t=35-55 min. The intensity of each the generated images represent the sum of the activity concentration of the ^{18}F-FDG during the period considered (t=35-55 min). The generated images were called SUM (SUMmed images). We used the SUM images as reference images since these images are used in routine clinical practice.

III.1.2 Normalization

For comparison purposes and to remove the negative values in PCIs, all PCIs generated were normalized to the SUM images using the proposed mathematical expression:

$$I_{new}(PCI(i)) = Q_i \frac{I_{max}(SUM\ images)}{I_{min}(Q_i)} \quad \text{(III.4)}$$

$$Q_i = I(PCI(i)) - I_{max}(PCI(i)) \quad \text{(III.5)}$$

where

- $PCI(i)$: is PCI1, PCI2 or PCI3,
- $I\big(PCI(i)\big)$: is the voxel intensity of the PCI(i),
- $I_{new}(PCI(i))$ is the new voxel intensity of the PCI(i),
- $I_{max}(SUM\ images)$ is the maximum voxel intensity of the SUM images generated in the interval 35-55 min.

Normalization was performed using (III.4) and (III.5) to transform the pixel intensities of the PC images with range (Min_PC, Max_PC) into a new range (newMin_PC, newMax_PC). (newMin_PC, newMax_PC) is equal to the (Min_SUM, Max_SUM) of the SUM images obtained in the time interval 35-55 min. The values of (newMin_PC, newMax_PC) are (0, 13050). To do so, we have followed these steps:

1. Calculation of the Max_PC;
2. Substraction of the Max_PC from the pixel intensities of the PC images.
3. Calculation of the Min_PC obtained from step 2.
4. The ratio was calculated as w=Max_SUM/Min_PC.
5. Multiplication of the pixel intensities of the PC images by the ratio w.

Example: PCI1 generated in the interval 0.-13 min with (Min_PC, Max_PC) = (-2.09, 22.66)

1. Max_PC = 22.66.
2. Substraction of the Max_PC from the pixel intensities of the PC images. Therefore, (Min_PC, Max_PC) became (-24.74, 0).

3. Calculation of the Min_PC obtained from step 2. Min_PC = -24.74.
4. The ratio was calculated as w=Max_SUM/Min_PC. w = 13050/-24.74.
5. The pixel intensities of the PC images are multiplied by the ratio w. (Min_PC, Max_PC) (0, 13050).

III.2 Quantitative analysis of PCIs and SUM images

To quantify lesion detectability on PCIs and SUM images, the TBR metric and activity profile lines (APLs) were utilized. For this purpose, a cylindrical Volume of Interests (VOIs) and line profiles were drawn at the level of the liver lesion on both PCIs and SUM transverse images using 3D slicer software [FED12]. The outlined VOIs are illustrated in Figure III.3.

The TBR scores were calculated using the following expression:

$$TBR = \frac{I_{tumor} - I_{background}}{I_{background}} \quad \textbf{(III.6)}$$

Where

I_{tumor} and $I_{backbround}$ are the mean pixel intensity values determined in VOIs for the tumor and the liver, respectively.

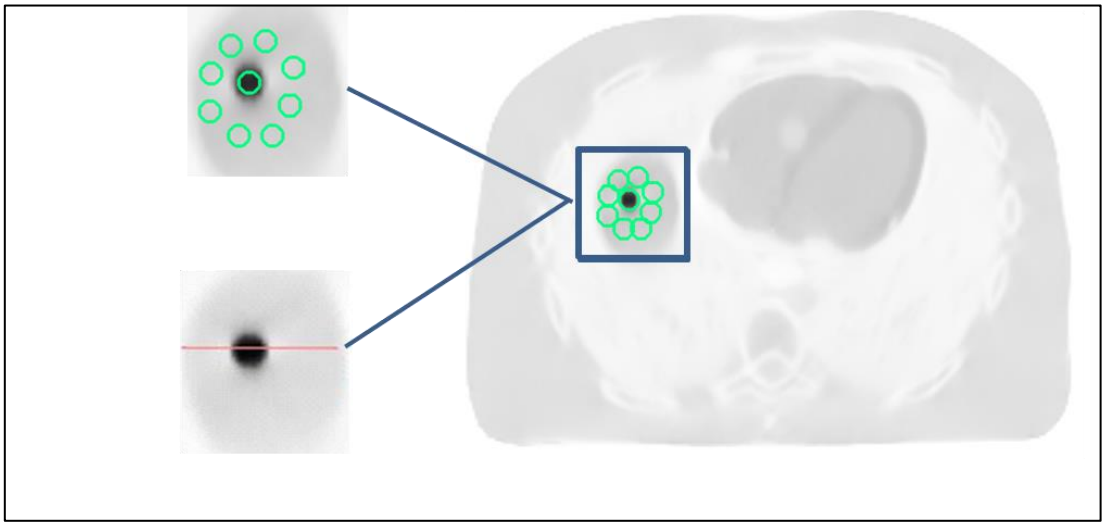

Figure III.3. VOIs placed in the tumor and background (in the liver) and ALPs used in the calculation of the TBR.

In the following sections, we investigated the improvement of lesion detectability and optimization of scanning time using the PCA method.

III.3 Improvement in lesion detectability

To demonstrate the improvement in the quality of the ^{18}F-FDG PET images, in terms of lesion detectability, which can be achieved using the PCA method, we applied the PCA method to the data at intervals of 35-55 min. The frames considered in this interval were frames 25 to 28. The summed method is also applied in the same interval. The process of generating the two types of images is illustrated in Figure III.4. The generated PCI1, PCI2, and PCI3 images were normalized according to the normalization procedure explained in § **III.1.2.**

The transverse slices at the lesion level of the generated images (PCI1, PCI2, PCI3 and SUM images) are illustrated in Figure III.5. The obtained PCI1, PCI2, and PCI3 were compared to the reference images (SUM images generated at T = 35-55 min) qualitatively and quantitatively by calculating the TBR and ALPs.

III.3.1 Qualitative analysis

Figure III.5 clearly shows that the lesion was successfully detected in the PCI2 and SUM images with high activity in the lesion, while no qualitative diagnostic information could be deduced from the PCI3 image. We can see also that the lesion can be detected in PCI1 with lower activity in the lesion than in the liver. This observation is in accordance with the fact that the PCA method generates images with decreasing amounts of variance. The variance in PCI3 is approximately zero since the total variance in the original data (frames 25 to 28) is small and the maximum amount of this variance was captured by the PCI1 then PCI2.

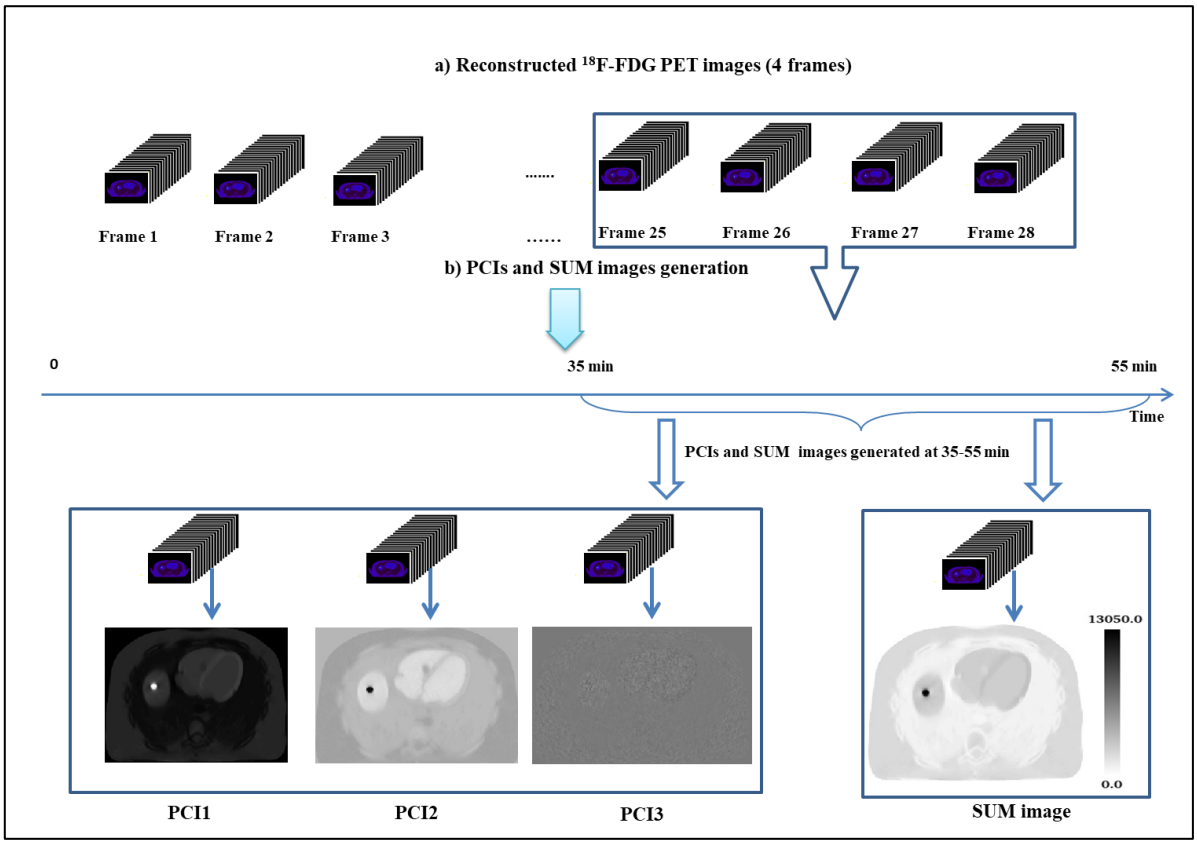

Figure III.4: Flowchart demonstrating the generation procedure of PCIs and SUM images at 35-55 min post injection, for lesion detectability enhancement purposes.

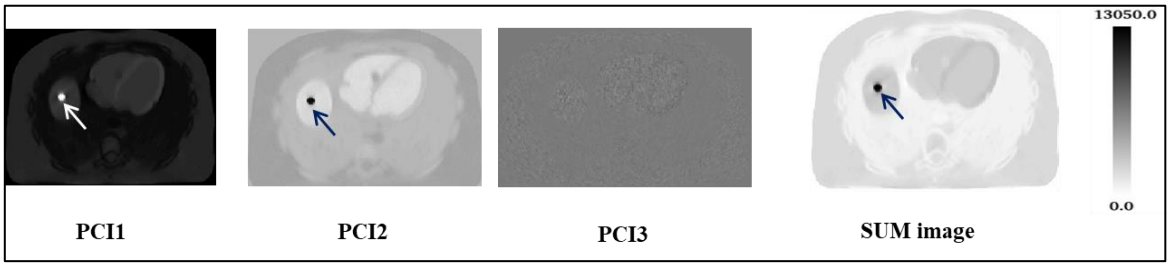

Figure III-5: Comparison of transverse slices obtained by the PCA and summed methods at T = 35-55 min post injection. The arrow shows the lesion in the liver.

III.3.2 Quantitative analysis

III.3.2.1 TBR and ALP calculation

We calculated the TBR on PCIs and SUM images to evaluate quantitatively the performance of the applied method in terms of lesion detectability. The TBR values obtained from the PCI1, PCI2 and SUM images were -0.78 ± 0.01, 4.05 ± 0.5 and 3.09 ± 0.50, respectively. As expected, the TBR of the PCI1 was negative since the activity in the liver was greater than that in the lesion.

We also calculated ALP curves at the lesion level on the PCI1, PCI2, PCI3, and SUM images. The ALP curves are given in Figure III-6. The results revealed that the APLs of the PCI2 and SUM images are close to each other, whereas the APL of the PCI3 seemed to be almost a line since the voxel intensities are almost around the same value. The ALPs of PCI1, compared to the ALP of SUM images, showed that the lesion voxel intensities were lower than those of the liver.

Qualitative and quantitative analyses using TBR and ALP curves demonstrated that PCI2 could provide superior lesion detectability than SUM images.

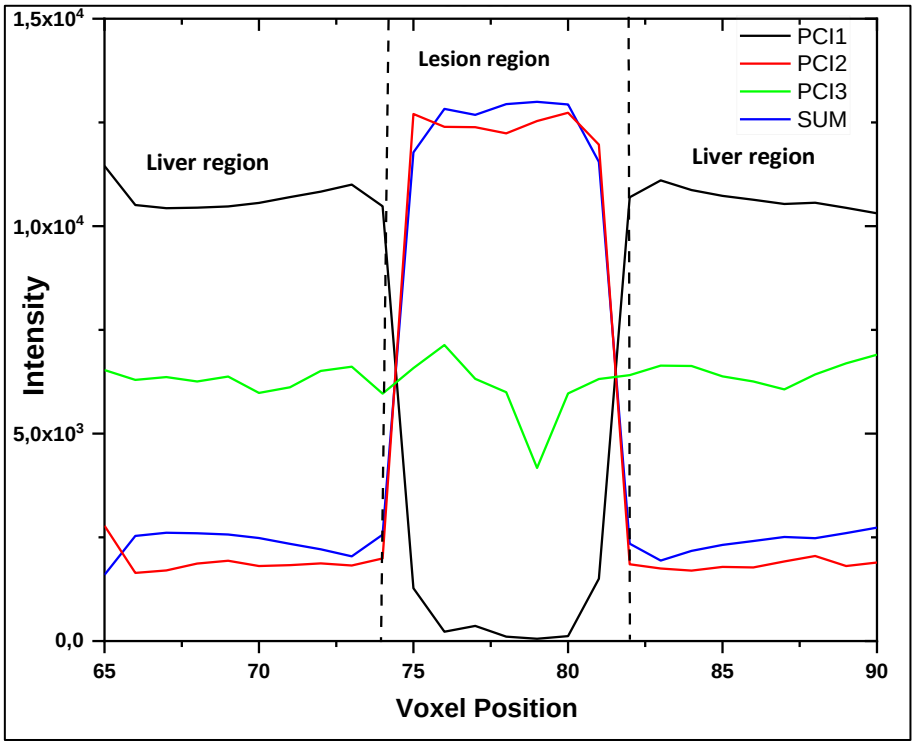

Figure III-6: Activity lines profile (ALPs) drawn at the lesion level on PCI1, PCI2, PCI3, and SUM images generated at T=35-55 min post injection.

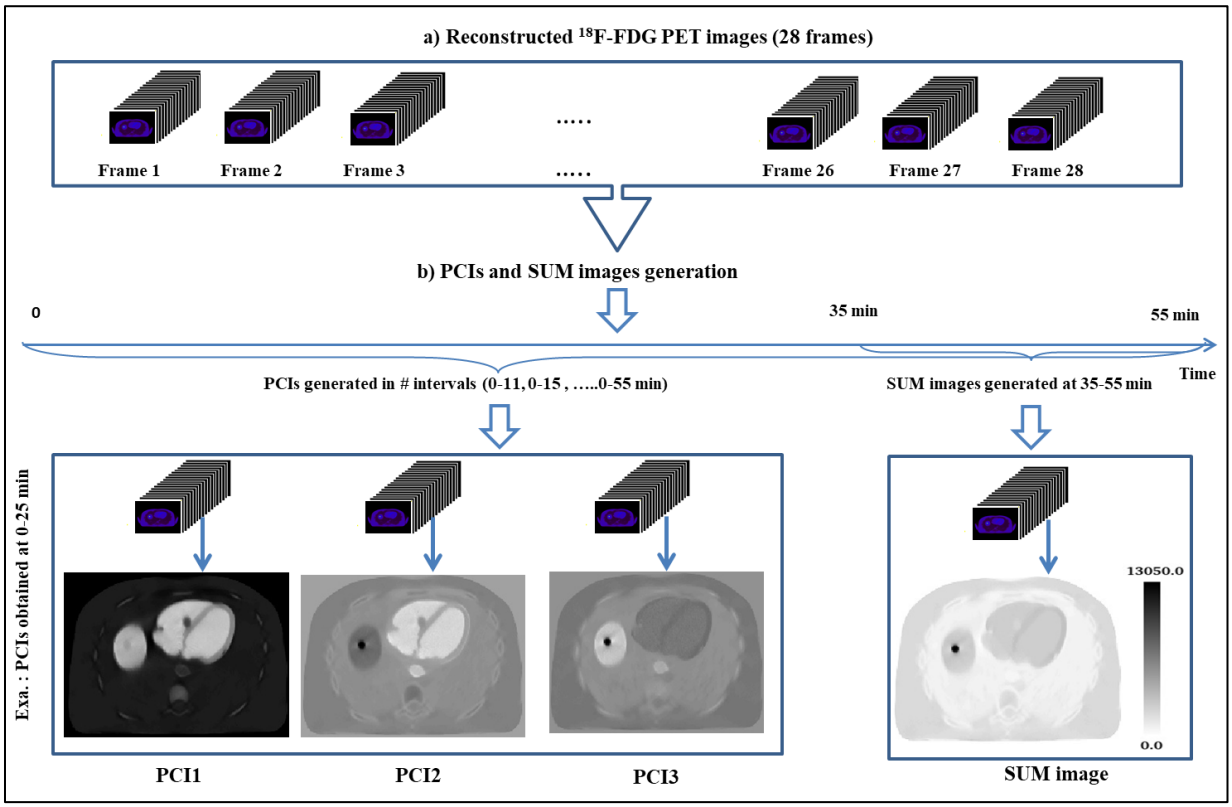

Figure III.7: Flowchart demonstrating the generation procedure of PCIs and SUM images at different intervals for scanning time reduction purposes.

III.4 Scan time optimization

We also used PCA to investigate the effect of the time duration on the dPET images and shorten PET dynamic scans. The objective was to reduce the scanning time while preserving lesion detectability. For this purpose, we generated PCIs at 11, 13, 15, 20, 25, 30, 35, 40, 45, 50 and 55 min, starting from the zero time point after ^{18}F-FDG injection. The frames considered in each time interval are given in Table III.1. The generation process is illustrated in Figure III-7. The generated PCI1, PCI2, and PCI3 images were also normalized according to the normalization procedure explained in § III.1.2.

We compared the obtained PCI1, PCI2, and PCI3 in each time interval to the reference images (SUM images generated at T = 35-55 min) qualitatively and quantitatively by calculating the TBR and APLs. All the obtained images are illustrated in Figures III-8.a, b, and c. The TBR and APL calculated as function of scanning time on PCI1, PCI2 and PCI3 are illustrated in Figures III-9.

Table III.1: Time intervals with the corresponding frames.

Time interval (min)	Frames
0-11	1-18
0-13	1-19
0-15	1-20
0-20	1-21
0-25	1-22
0-30	1-23
0-35	1-24
0-40	1-25
0-45	1-26
0-50	1-27
0-55	1-28

III.4.1 Qualitative analysis

Qualitatively, from Figure III-8.a, b, c, the comparison with the SUM images demonstrated that for the PCI3, the lesion was clearly detectable regardless of the scanning time. However, for T > 40 min, the activity in the lesion was lower than that in the liver. In the case of PCI2, the lesion could not be detected at T = 11 min and was hardly detectable at T=13 min. However, the lesion could be easily detected elsewhere. For the PCI1, the lesion could not be detected at T = 25 min, T = 30 min and T = 25 min and was slightly detectable at the remaining intervals, with lower activity in the lesion than in the liver at T > 40 min.

III.4.2 Quantitative analysis

III.4.2.1 TBR and APL calculation

The calculated TBRs are shown in Figure III-9 for all the time intervals. In general, the TBR estimated on PCI3 was the closest to the SUM images (2.49±0.72 on PCI3 versus 3.08±0.49 on SUM images) and was greater than the PCI1 and PCI2 from 11 to 35 min. With regard to PCI2, the TBR increased with increasing scanning time (maximum of 3.87 ± 1.11 at T = 55 min). The TBR derived from the PCI1 decreased with increasing scanning time, with a maximum of 0.53± 0.11 at T=11 min.

Considering only visual assessment and TBR measurements, PCI2 is the closest to the SUM image at 25 and 35 mins, whereas PCI3 looks closest to the SUM image at 15, 20 and 25 mins.

To have better insights on the ^{18}F-FDG uptake within the liver lesion and ease the selection of the best time timing to achieve the aim of this study (shortening the total scanning duration while preserving the detectability of the tumor lesion), The APL s were calculated and illustrated in Figure III-10.a, b, c.

The ALPs demonstrated nearly similar uptake on the PCI3 compared to the SUM image at timing 15, 20, 25 , 25 and 30 mins, whereas PCI2 comparable uptake to SUM image at timing 40, 45, and 50 mins.

To summarize and take into account the visual appearance of the 3 PCIs, the TBR measurements and ALP analysis revealed that the PCI3 at timing 20 min was the closest qualitatively and quantitively to the SUM image and could be used for lesion detectability on the basis of the present study's analysis.

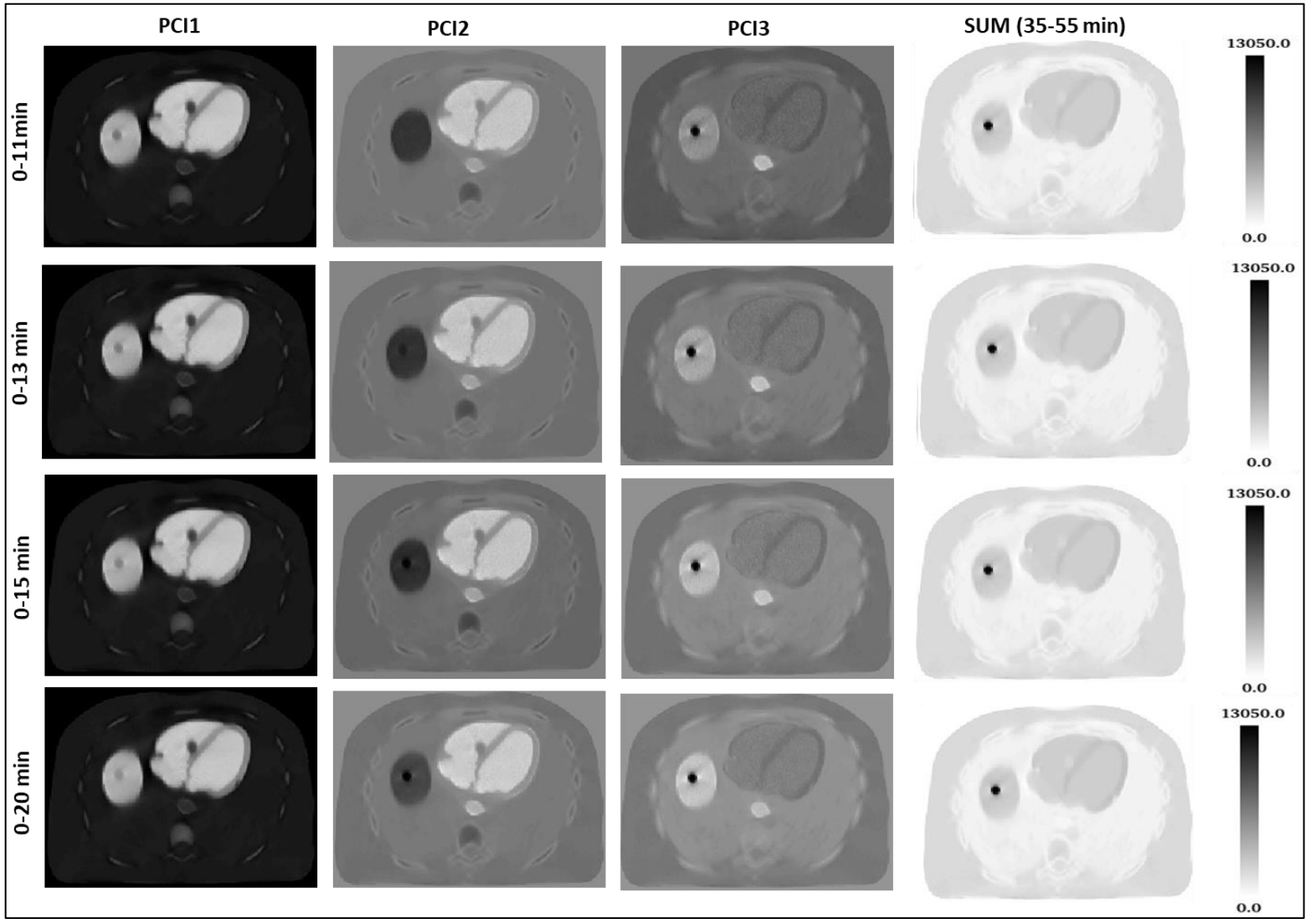

Figure III-8.a Transverse slices obtained by the PCA method at 0-11, 0-13, 0-15 and 0-20 time intervals showing ^{18}F-FDG uptake in lesions and other tissues. The SUM images were generated at 35-55 min intervals as described above.

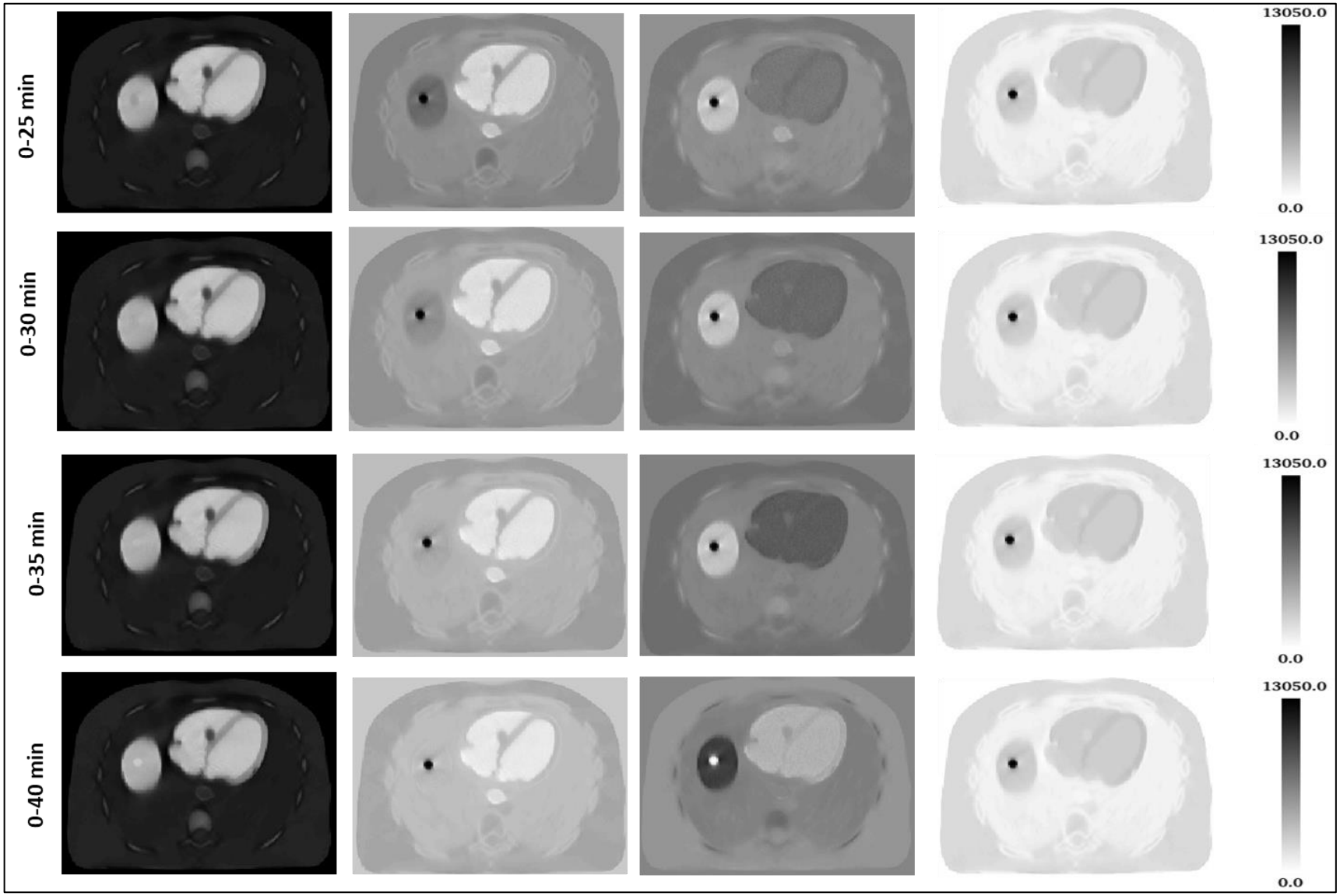

Figure III-8.b Transverse slices obtained by the PCA method at 0-25, 0-30, 0-35 and 0-40 time intervals showing ^{18}F-FDG uptake in lesions and other tissues. The SUM images were generated at 35-55 min intervals as described above.

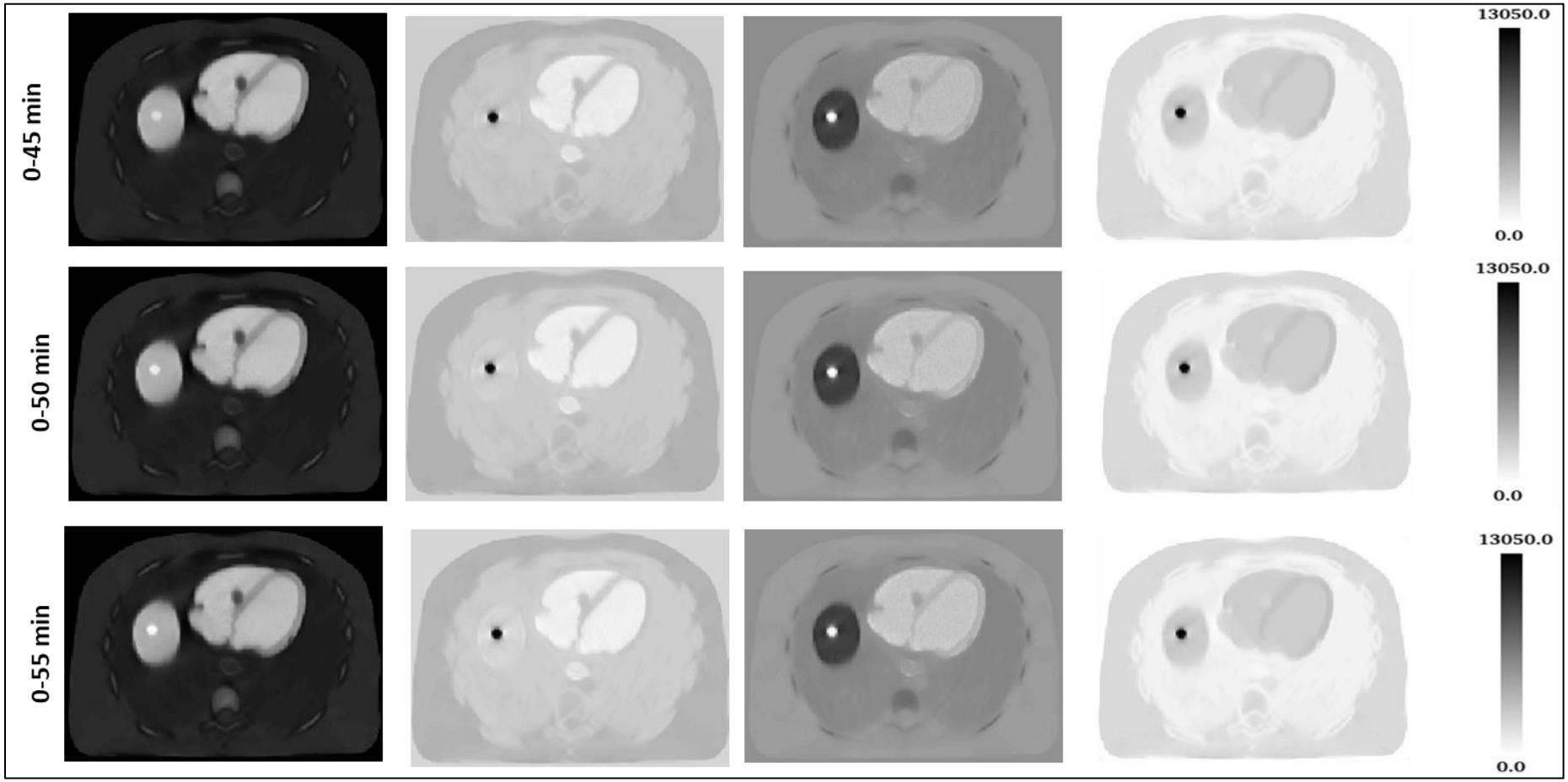

Figure III-8.c Transverse slices obtained by the PCA method at 0-45, 0-50 and 0-55 time intervals showing ^{18}F-FDG uptake in lesions and other tissues. The SUM images were generated at 35-55 min intervals as described above.

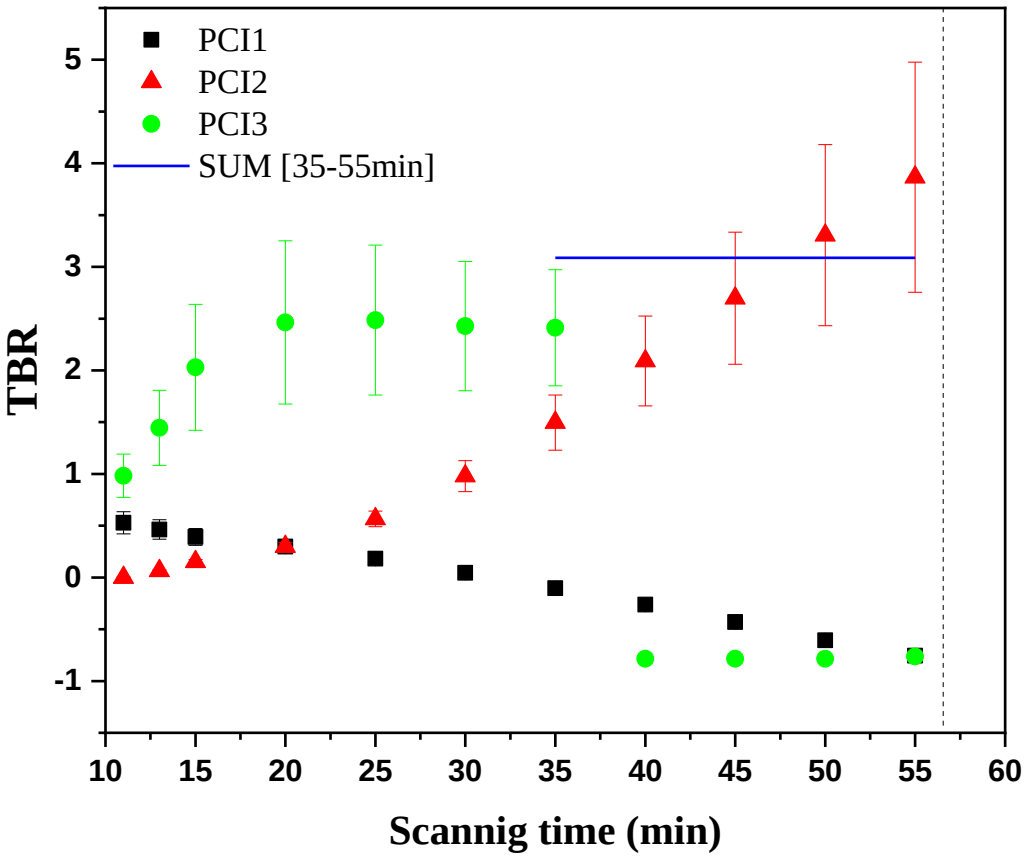

Figure III-9: TBR calculated from PCI1, PCI2, PCI3 and SUM images as a function of scanning time.

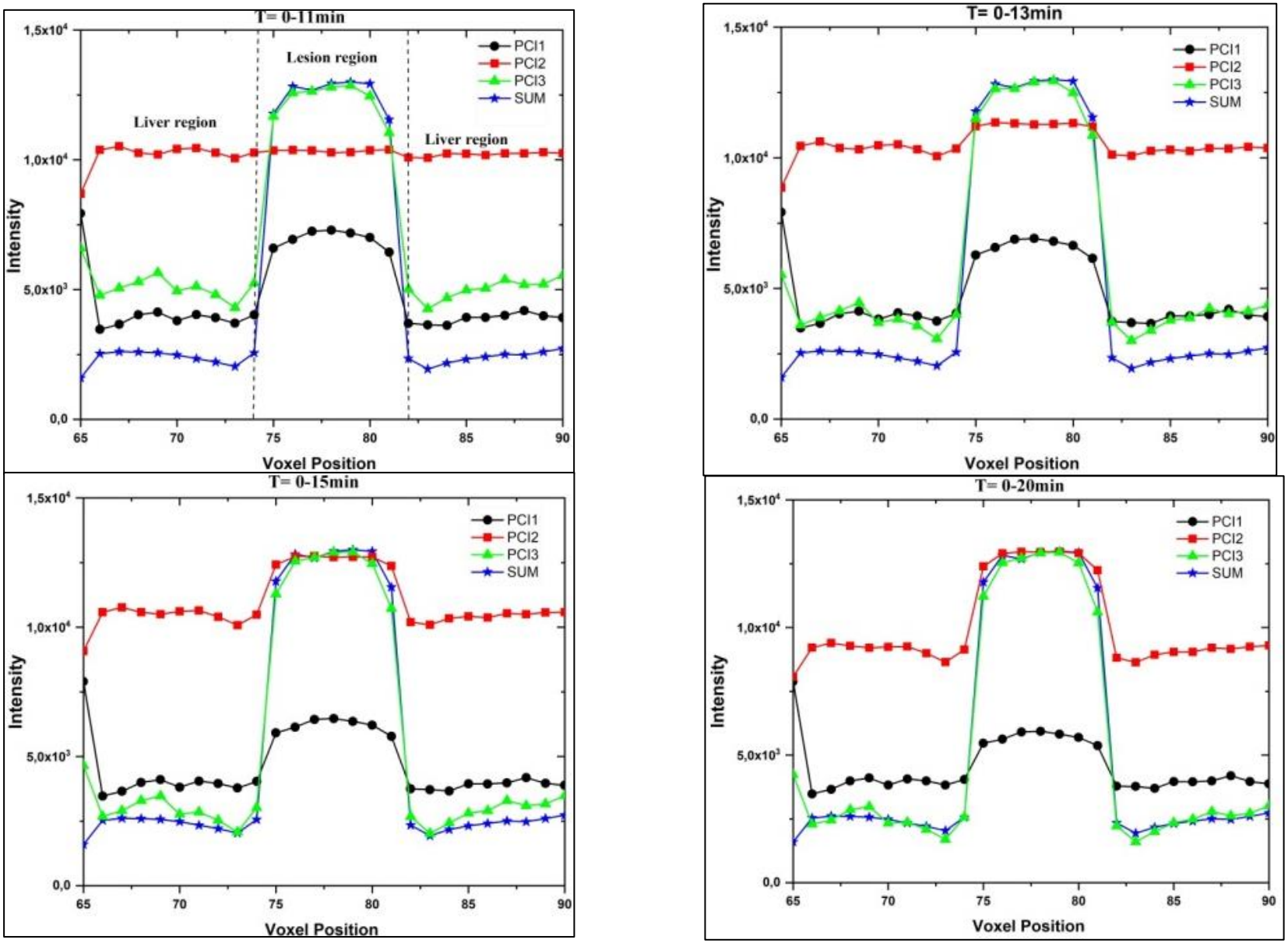

Figure III-10.a: Activity Lines Profiles (ALPs), as a function of scanning time (0-11, 0-13, 0-15, 0-20), of PCI1, PCI2, PCI3 and SUM images.

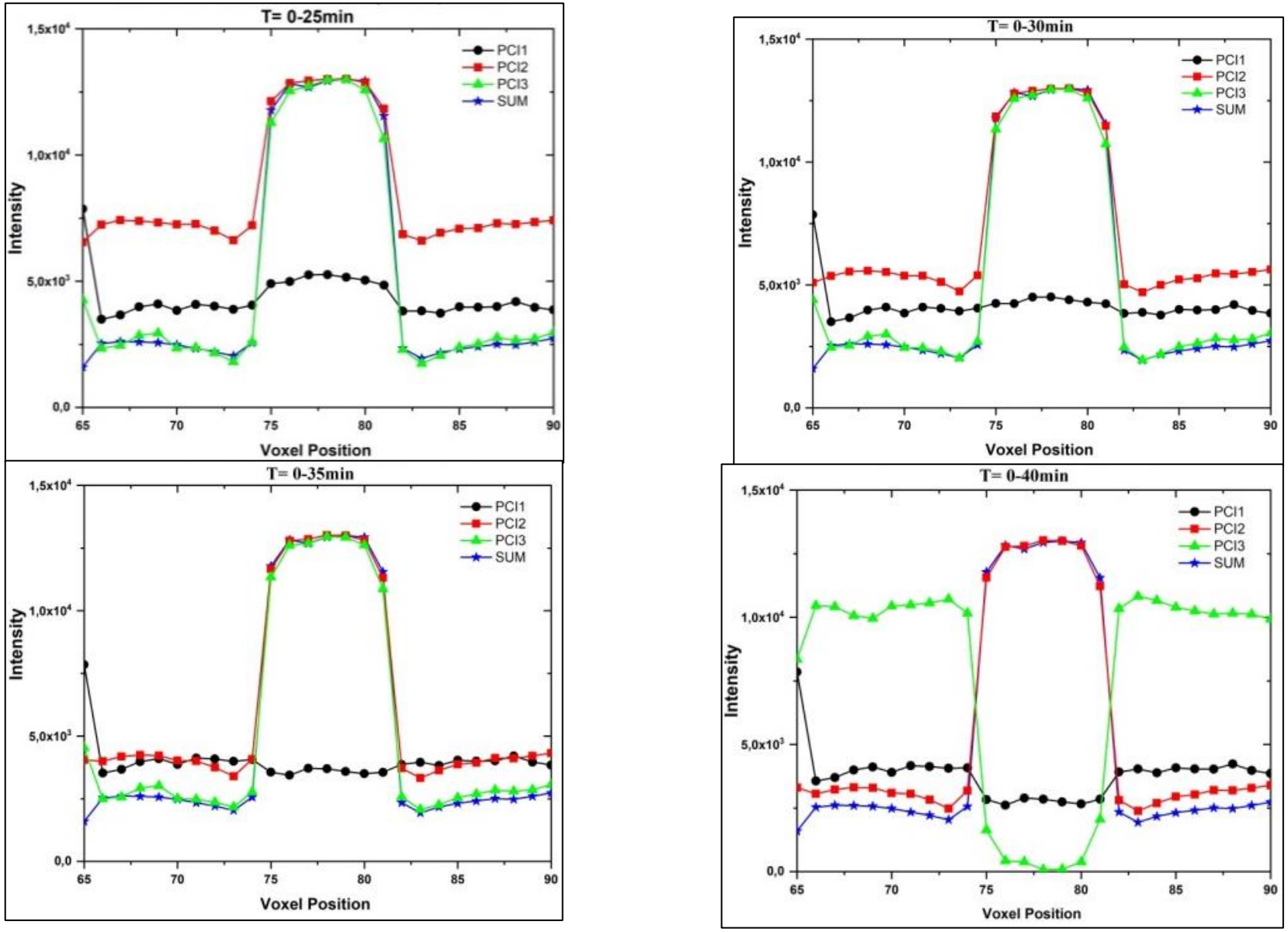

Figure III-10.b: Activity Lines Profiles (ALPs), as a function of scanning time (0-25, 0-30, 0-35, 0-40), of PCI1, PCI2, PCI3 and SUM images.

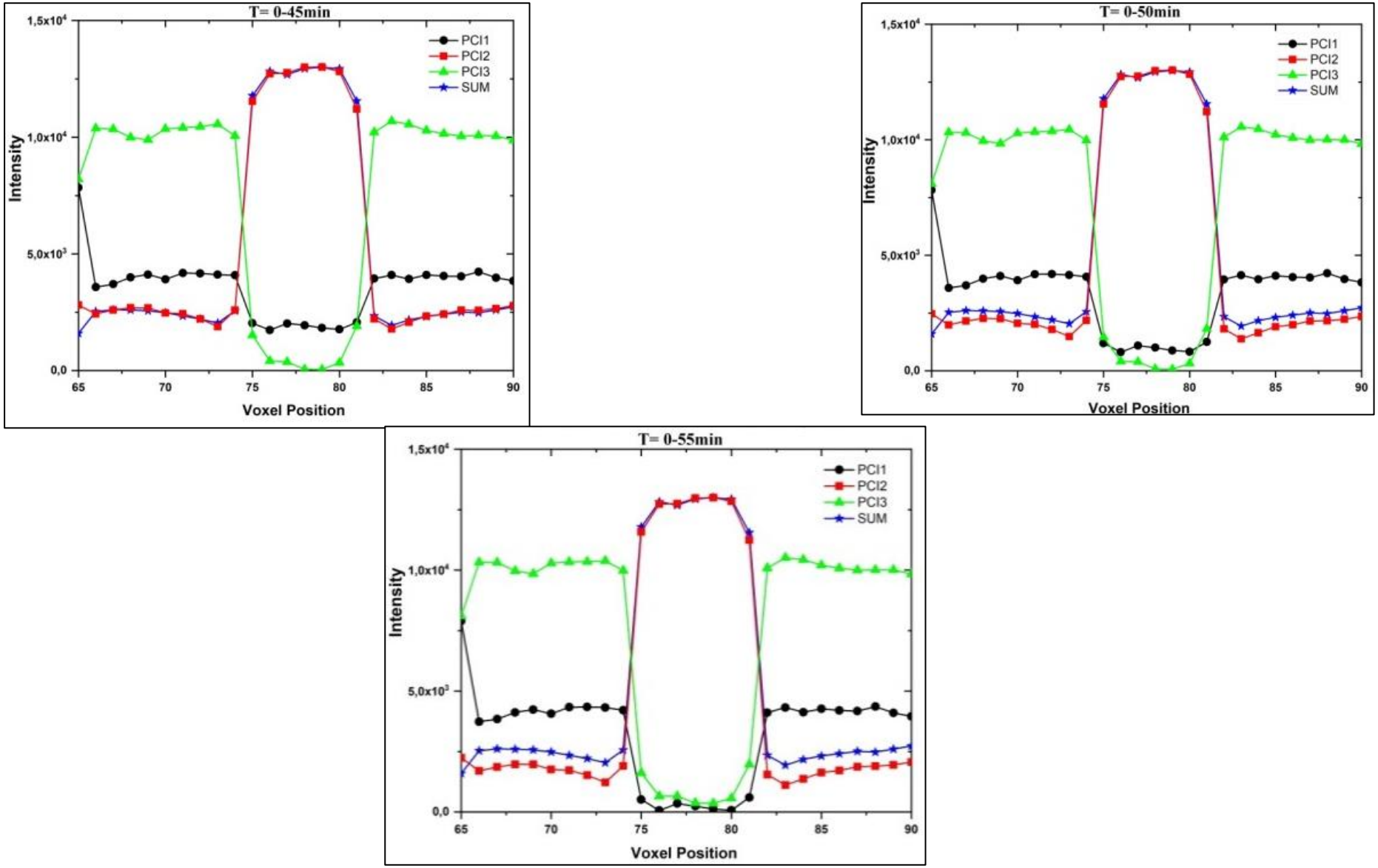

Figure III-10.c: Activity Lines Profiles (ALPs), as a function of scanning time (0-45, 0-50, 0-55), of PCI1, PCI2, PCI3 and SUM images.

III.5 Discussion

In this chapter, we aimed to shorten the dPET study and enhance lesion detectability by applying PCA to the dynamic ^{18}F-FDG series generated using the XCAT phantom in combination with the three-compartment model and a simulated input function and TACs of different tissues. The visual inspection and quantitative assessment of different time interval sequences guided us to select the most suitable time interval sequence to shorten the duration of the dPET study, which was found to be 20 minutes.

Several studies have been performed to optimize the acquisition time in dPET. Grkovski et al. [GRK17] showed that the acquisition time could be reduced to 20 min in the case of head and neck cancers using 120 patients' scans. The method used in this work was based on the comparison of metrics (TBR and pharmacokinetic parameters) calculated from the dataset with those derived from the full dataset. Additionally, the kinetic parameters obtained were rather equivalent in a comparison study carried out by Torizuka et al. [TOR00]. The latter used 20 patient scans, where all scans duration was 30 min and 60 min acquisition protocols. The authors reported that the 30 min kinetic parameters were similar to the 60 min parameters. Elsewhere, the study by Visser and coauthors [VIS08] used a population of 13 patients with non-small cell lung carcinoma and reported agreement between 30 min and 50 min acquisition protocols.

Although previous studies used patient data acquired using commercially available PET/CT protocols, our XCAT phantom-based approach offers an interesting option that could be used to shorten PET studies while preserving lesion detectability with a total scanning duration of 20 minutes, hence improving patient image reconstruction in dynamic frames. The use of more sophisticated reconstruction methods, such as OSEM iterative reconstruction, which incorporates time-of-flight information and point spread function modeling (OSEM-TOF-PSF), or regularization-based reconstruction methods [STR11] could help further the shortening of scanting time while improving lesion appearance and radiotracer uptake, hence enhancing further lesion visibility.

The authors recognize the lack of patient data in the study and emphasize that the simulated dynamic series can be considered clinically realistic, according to Lee and colleagues [LEE14], if a validated PET imaging system combined with a realistic model of the human body and an actual ^{18}F-FDG activity distribution are used. The single lesion model used in this study can also be extended to include multiple tumor lesions of different sizes and in different locations within the liver. The authors consider the outcome of this study

compelling enough support for its application and validation in a large patient population.

It worth nothing that even in the case of total body PET scanners [CHE18] (above 120 cm, extended FOV, increased sensitivity, and eased extraction of TACs), dynamic acquisitions still last for 55-60 mins, hence the use of such method (PCA) is of high interest to shorten acquisition time while preserving lesion detectability [HUA23].

Conclusion

Chapter III presents a comprehensive exploration of image generation techniques, focusing on PCA and SUM methods applied to dynamic ^{18}F-FDG PET images. Through PCA, principal component images are produced. The normalization process enhances the comparability of these images with SUM images used in clinical routine. Quantitative analysis involving TBR metrics and activity profile lines (ALPs) demonstrates the potential of PCA-generated images, particularly PCI2, in enhancing lesion detectability compared to SUM images. Additionally, the study investigated the impact of scanning time on image quality, suggesting that PCI3 at 20 min may offer optimal lesion detectability while reducing the total scanning duration.

Overall, this chapter elucidates the value of the PCA in image generation and its potential implications for clinical imaging.

General Conclusion

General conclusion and Perspectives

dPET remains limited to research since it suffers from noisy images and long durations of data acquisition. Despite several efforts in dPET [SAM20][GRK17][STR11], the long-time data acquisition is still hampering the clinical use of this technique.

This work aimed to enhance lesion detectability and shorten the duration of dPET by applying PCA to the simulated dynamic ^{18}F-FDG series due to the unavailability of clinical data and the absence of a gold standard. The simulated dynamic ^{18}F-FDG series were generated using an XCAT phantom in combination with the three-compartment model and a simulated IF and TAC of different tissues. A 9 mm diameter lesion mimicking the tumor lesion was inserted within the liver. The widely used STIR reconstruction software was employed to reconstruct the dynamic frames. We used an in-house script developed to generate different tissues TAC's, manipulate the 4D-XCAT phantom and handle all STIR functionalities, such as forward projection, attenuation correction, adding noise to the sinograms and image reconstruction. The reconstruction computation time was 8.76 min/frame.

We qualitatively and quantitatively demonstrated the improvement in the detectability of the considered liver lesions when the PCA method was applied at 35-55 min post injection on simulated dynamic ^{18}F-FDG-PET images.

Regarding the scan time reduction, we have demonstrated qualitatively and quantitatively the possibility to reduce the total duration of data acquisition in dPET while preserving the detectability of lesions on simulated dynamic ^{18}F-FDG PET images. The findings suggest that the third principal component could be used to obtain images in the first 20 min post injection with a lesion detectability level similar to that of usual static images acquired 35 min postinjection.

The use of a 4D-XCAT phantom and kinetic modeling simulation in dynamic ^{18}F-FDG PET imaging can aid in lesion detectability investigations and scan time reduction, thus providing better patient care and improving the efficiency of clinical PET imaging. However, it is important to note that simulation results should always be validated against real patient data before being applied in clinical practice.

The findings of this work demonstrate that PCA can play a key role in tumor detection and reduce scanning time, thereby increasing patient comfort and minimizing patient motion.

The present work has raised the research perspective of the use of artificial intelligence approaches to predict and generate SUM images in the desired time interval to normalize the PCIs estimated early after injection.

List of publications

International journals (2023)

1. Dynamic ^{18}F-FDG PET images simulation using 4D-XCAT phantom and kinetic modeling for lesion detectability investigation and scan time reduction purpose. Iranian Journal of Medical Physics, 2023 - ijmp.mums.ac.ir. (DOI 10.22038/IJMP.2023.69200.2216).

   Fethi Bezoubiri, Tahar Zidi, Fayçal Kharfi.

2. Optimization of scanning time in dynamic ^{18}F-FDG-PET for lesion detectability using principal component analysis: a feasibility study". Submitted for publication (2023).

Fethi Bezoubiri, Yassine Bouchareb, Asma Alem-Bezoubiri, Tahar Zidi, Fayçal Kharfi.

International conferences

3. Optimization of scanning time in dynamic ^{18}F-FDG PET images using principal component analysis. Middle East Federation of Organizations of Medical Physics (MEFOMP), 19 to 22 May 2023.

   F. Bezoubiri, Y. Bouchareb, T. Zidi, F. Kharfi,

   .

4. Simulation of dynamic ^{18}F-FDG PET images for lesion detectability investigation using kinetic modeling and the XCAT phantom. 1st International Conference and School on Radiation Imaging (ICSRI-2021), 26-30 September 2021, Setif, Algeria.

   F. Bezoubiri, T. Zidi, F. Kharfi

Additional Contribution (Other studies performed and published during the thesis period)

International journals

5. Evaluation of a neutron spectrum from Bonner spheres measurements using a Bayesian parameter estimation combined with the traditional unfolding methods. Radiation Physics and Chemistry, 148, 33-42. doi.org/10.1016/j.radphyschem.2018.02.014

   Mazrou, H., & **Bezoubiri, F**. (2018).

International conference proceedings

6. Investigation and improvement of the solution neutron spectrum around an 241Am-Be based neutron irradiator using the traditional unfolding procedure. In AIP Conference Proceedings (Vol. 1994, No. 1). AIP Publishing https://doi.org/10.1063/1.5048163

Bezoubiri, F & Mazrou, H. (2018).

.

7. Monte Carlo modeling of the head of Varian Clinac 2100C linear accelerator operating in 18 MV utilizing GATE/GEANT4. In AIP Conference Proceedings (Vol. 1994, No. 1). AIP Publishing. https://doi.org/10.1063/1.5048162

Bezoubiri, F., Alem-Bezoubiri, A., Khoudri, S., & Arib, M. (2018).

References

References

[ALE20]: Al-Enezi, M. S., & Bentourkia, M. H. (2020). Kinetic Modeling of Dynamic PET-^{18}F-FDG Atherosclerosis Without Blood Sampling. IEEE Transactions on Radiation and Plasma Medical Sciences, 4(6), 729-734.

[BAI05]: Bai, B., Laforest, R., Smith, A. M., and Leahy, R. M. (2005). Evaluation of MAP Image Reconstruction with Positron Range Modeling for 3D PET. Nuclear Science Symposium Conference Record., page 2686–2689.

[BEN05]:Bentourkia, M. (2005). Kinetic modeling of PET data without blood sampling. IEEE transactions on nuclear science, 52(3), 697-702.

[BEN07]: Bentourkia M, Zaidi H (2007) Tracer kinetic modeling in PET. PET Clin 2:267–277.

[BES20]: Besson, F. L., Fernandez, B., Faure, S., Mercier, O., Seferian, A., Mignard, X., ... & Durand, E. (2020). ^{18}F-FDG PET and DCE kinetic modeling and their correlations in primary NSCLC: First voxel-wise correlative analysis of human simultaneous [18F] FDG PET-MRI data. EJNMMI research, 10(1), 1-13.

[BEZ23]: Bezoubiri, F., ZIDI, T., & Kharfi, F. (2023). Dynamic ^{18}F-FDG PET images simulation using 4D-XCAT phantom and kinetic modeling for lesion detectability investigation and scan time reduction purpose. Iranian Journal of Medical Physics.

[BIS02]: Bischof, D. (2002). Progress in the diagnosis and treatment of disease by nuclear medicine and molecular imaging. Highlights of the European Association of Nuclear Medicine Congress, Naples 2001. European journal of nuclear medicine and molecular imaging, 29(1), 139-159.

[BOE11]: Boellaard R (2011) Need for standardization of ^{18}F-FDG PET/CT for treatment response assessments. J Nucl Med 52(Suppl 2):93S–100S.

[BOE15]: Boellaard, R., Delgado-Bolton, R., Oyen, W. J., Giammarile, F., Tatsch, K., Eschner, W & Krause, B. J. (2015). FDG PET/CT: EANM procedure guidelines for tumour imaging: version 2.0. European journal of nuclear medicine and molecular imaging, 42(2), 328-354.

[BOE15]: Boellaard, R., Delgado-Bolton, R., Oyen, W. J., Giammarile, F., Tatsch, K., Eschner, W., ... & Krause, B. J. (2015). FDG PET/CT: EANM procedure guidelines for tumour imaging: version 2.0. European journal of nuclear medicine and molecular imaging, 42(2), 328-354.

[BOU23]: Bouchareb, Y., Tag, N., Sulaiman, H., Al-Riyami, K., Jawa, Z., & Al-Dhuhli, H. (2023). Optimization of BMI-Based Images for Overweight and Obese Patients—Implications on Image Quality, Quantification, and Radiation Dose in Whole Body ^{18}F-FDG PET/CT Imaging. Nuclear Medicine and Molecular Imaging, 1-14.

[BOU99]: Bouchareb, Y., Frouin, F., DeCesare, A., Merlet, P., Frouin, V., & Gregoire, M. C. (1999). Régularisation de l'Analyse Factorielle des Séquences d'Images Médicales (AFSIM). Application aux études de perfusion myocardique à l'eau marquée en TEP. Innovation et technologie en biologie et médecine, 20(2), 93-100.

[BRO69]: Brownell, G. L., Burnham, C. A., Wilensky, S., Arnonow, S., Kaemi, H., and Strieder, D.

[CHE07]: Chen, K., Chen, X., Renaut, R., Alexander, G. E., Bandy, D., Guo, H., & Reiman, E. M. (2007). Characterization of the image-derived carotid artery input function using independent component analysis for the quantitation of [18F] fluorodeoxyglucose positron emission tomography images. Physics in Medicine & Biology, 52(23), 7055.

[CHE12]: Cherry, S. R., Sorenson, J. A., & Phelps, M. E. (2012). Physics in Nuclear Medicine (4th ed.). Philadelphia, PA: Elsevier Saunders.

[CHE18]: Cherry, S. R., Jones, T., Karp, J. S., Qi, J., Moses, W. W., & Badawi, R. D. (2018). Total-body PET: maximizing sensitivity to create new opportunities for clinical research and patient care. Journal of Nuclear Medicine, 59(1), 3-12.

[CHER05]: Cherry, S., Sorenson, J., and Phelps, M. (2005). Physics in nuclear medicine, 3rd ed. Radiology, 234(3), 878.

[CRI87]: Cristy, M., Eckerman, K.F., 1987. Specific Absorbed Fractions of Energy at Various Ages from Internal Photon Sources: 3, Five-Year-Old (No. ORNL/TM-8381/V3). Oak Ridge National Lab., TN (USA).

[CUT92]: Cutler, P. D., Cherry, S. R., Hoffman, E. J., Digby, W. M., and Phelps, M. E. (1992). Design features and performance of a PET system for animal research. Journal of Nuclear Medicine, 33 :595–604.

[CZE06]: Czernin J, Allen-Auerbach M, Schelbert HR (2007) Improvements in cancer staging with PET/CT: literature-based evidence as of September 2006. J Nucl Med 48:78S–788S.

[DAH02]: Dahlbom, M. (2002). Estimation of Image Noise in PET Using the Bootstrap Method.IEEE Transactions on Nuclear Science, 49(5) :2062–2066.

[DAH92]: Dahlbom, M., Hoffman, E., and Hoh, C. (1992). Whole-body positron emission tomography. 1. methods and performance characteristics. Journal of Nuclear Medicine, 33 :1191–1199.

[DEG]: De Geus-Oei, L. F., Visser, E. P., Krabbe, P. F., van Hoorn, B. A., Koenders, E. B., Willemsen, A. T., ... & Oyen, W. J. (2006). Comparison of image-derived and arterial input functions for estimating the rate of glucose metabolism in therapy-monitoring ^{18}F-FDG PET studies. Journal of Nuclear Medicine, 47(6), 945-949.

[DIM06]: Dimitrakopoulou-Strauss, A., Georgoulias, V., Eisenhut, M., Herth, F., Koukouraki, S., Mäcke, H. R., ... & Strauss, L. G. (2006). Quantitative assessment of SSTR2 expression in patients with non-small cell lung cancer using 68 Ga-DOTATOC PET and comparison with ^{18}F-FDG PET. European journal of nuclear medicine and molecular imaging, 33(7), 823-830.

[DIM21-a]: Dimitrakopoulou-Strauss, A., Pan, L., & Sachpekidis, C. (2021a). Kinetic modeling and parametric imaging with dynamic PET for oncological applications: general considerations, current clinical applications, and future perspectives. European Journal of Nuclear Medicine and Molecular Imaging, 48(1), 21-39.

[DIM21-b]: Dimitrakopoulou-Strauss, A., Pan, L., & Sachpekidis, C. (2021b, November). Parametric Imaging With Dynamic PET for Oncological Applications: Protocols, Interpretation, Current Applications and Limitations for Clinical Use. In Seminars in Nuclear Medicine. WB Saunders.

[ELA10] : Elad, M. (2010). Sparse and Redundant Representations: From Theory to Applications in Signal and Image Processing. *Springer Science & Business Media*.

[FAH19]:Fahrni, G., Karakatsanis, N. A., Di Domenicantonio, G., Garibotto, V., & Zaidi, H. (2019). Does whole-body Patlak ^{18}F-FDG PET imaging improve lesion detectability in clinical oncology?. European radiology, 29(9), 4812-4821.

[FED12]: Fedorov A., Beichel R., Kalpathy-Cramer J., Finet J., Fillion-Robin J-C., Pujol S., Bauer C., Jennings D., Fennessy F.M., Sonka M., Buatti J., Aylward S.R., Miller J.V., Pieper S., Kikinis R. 3D Slicer as an Image Computing Platform for the Quantitative Imaging Network. Magnetic Resonance Imaging. 2012 Nov;30(9):1323-41. PMID: 22770690. PMCID: PMC3466397.

[FEN93]: Feng, D., Huang, S. C., & Wang, X. (1993). Models for computer simulation studies of input functions for tracer kinetic modeling with positron emission tomography. International journal of bio-medical computing, 32(2), 95-110.

[FEN96]: Feng D, Wang X. A computer simulation study on the effects of input function measurement noise in tracer kinetic modeling with positron emission tomography (PET). Computers in biology and medicine. 1993 Jan 1;23(1):57-68.

[FES20]: Fessler, J. A. (2020). *Model-Based Image Reconstruction for MRI*. New York: Cambridge University Press.

[FRI93]: Friston, K. J., Frith, C. D., Liddle, P. F., & Frackowiak, R. S. (1993). Functional connectivity: the principal-component analysis of large (PET) data sets. Journal of Cerebral Blood Flow & Metabolism, 13(1), 5-14.

[FRI93]: Friston, K. J., Frith, C. D., Liddle, P. F., & Frackowiak, R. S. (1993). Functional connectivity: the principal-component analysis of large (PET) data sets. Journal of Cerebral Blood Flow & Metabolism, 13(1), 5-14.

[FRO01]: Frouin F, Merlet P, Bouchareb Y, Frouin V, Dubois-Randé JL, De Cesare A, Herment A, Syrota A, Todd-Pokropek A. Validation of myocardial perfusion reserve measurements using regularized factor images of H(2)(15)O dynamic PET scans. J Nucl Med. 2001 Dec; 42(12):1737-46.

[GAG92]: Gagnon, D., Laperrière, L., Pouliot, N., de Vries, D. J., and Moore, S. C. (1992). Monte carlo analysis of camera-induced spectral contamination for different primary energies. Physics in Medicine and Biology, 37 :1725–1739.

[GAM02]: Gambhir SS (2002) Molecular imaging of cancer with positron emission tomography. Nat Rev Cancer 2:683–693

[GHA91]: Ghanem, R. and Spanos, P. (1991) Stochastic Finite Elements: A Spectral Approach, Springer-Verlag, New York.

[GRK17] : Grkovski, M., Schöder, H., Lee, N. Y., Carlin, S. D., Beattie, B. J., Riaz, N., ... & Humm, J. L. (2017). Multiparametric imaging of tumor hypoxia and perfusion with 18F-fluoromisonidazole dynamic PET in head and neck cancer. Journal of Nuclear Medicine, 58(7), 1072-1080.

[HAB08] : Habeck, C., Foster, N. L., Perneczky, R., Kurz, A., Alexopoulos, P., Koeppe, R. A., Drzezga, A. & Stern, Y. (2008). Multivariate and univariate neuroimaging biomarkers of Alzheimer's disease, NeuroImage 40(4): 1503–1515.

[HAM94]: Hamamatsu (1994). Photomultiplier tube : Principal to application. Hamamatsu Photonics K.K.

[HER88]: Herholz, K., Ziffling, P., Staffen, W., Pawlik, G., Wagner, R., Wienhard, K., & Heiss, W. D. (1988). Uncoupling of hexose transport and phosphorylation in human gliomas demonstrated by PET. European Journal of Cancer and Clinical Oncology, 24(7), 1139-1150.

[HOF76]: Hoffman, E., Phelps, M., Mullani, N., Higgins, C., and Ter Pogossian, M. (1976). Design and performance-characteristics of a whole-body positron transaxial tomograph. Journal of Nuclear Medicine, 17 :493–502.

[HOT33]: Hotelling, H. (1933) 'Analysis of a complex of statistical variables into principal components', Journal of Educational Psychology, Vol. 24, No. 6, pp.417–441.

[HUA11]: Huang SC (2000) Anatomy of SUV. Standardized uptake value. Nucl Med Biol 27:643–646.

[HUA23]: Huang, Y., Wang, M., Jiang, L., Wang, L., Chen, L., Wang, Q., ... & Han, Y. (2023). Optimal clinical protocols for total-body ^{18}F-FDG PET/CT examination under different activity administration plans. EJNMMI physics, 10(1), 14.

[ICR92]: ICRU, Measurement of Dose Equivalents from External Photon and Electron Radiations. International Commission on Radiation Units and Measurements, Bethesda, MD, 1992. Report No. 47.

[KAK01]: Kak, A. C., & Slaney, M. (2001). Principles of Computerized Tomographic Imaging. Philadelphia, PA: Society for Industrial and Applied Mathematics (SIAM).

[KAR11]: Karakatsanis, N. A., Lodge, M. A., Zhou, Y., Mhlanga, J., Chaudhry, M. A., Tahari, A. K., ... & Rahmim, A. (2011, October). Dynamic multi-bed FDG PET imaging: feasibility and optimization. In 2011 IEEE nuclear science symposium conference record (pp. 3863-3870). IEEE.

[KEY95]: Keyes, J. W. (1995). SUV: standard uptake or silly useless value?. Journal of Nuclear Medicine, 36(10), 1836-1839.

[KIM09]: Kimura, N., Yamamoto, Y., Kameyama, R., Hatakeyama, T., Kawai, N., & Nishiyama, Y. (2009). Diagnostic value of kinetic analysis using dynamic ^{18}F-FDG-PET in patients with malignant primary brain tumor. Nuclear Medicine Communications, 30(8), 602-609.

[KLE19]: Klein, O. and Nishina, T. (1929). Über die streuung von strahlung durch freie elektronen nach der neuen relativistischen quantendynamik von dirac. Zeitschrift für Physik, 52(11-12).

[KNO12]:. Knowles, S. and Wu, A. (2012). Advances in immuno-positron emission tomography : antibodies for molecular imaging in oncology. J. Clin. Oncol., 30 :3884–3892.

[KNO99]: Radiation detection and mesurement. 3rd ed. Wiley.

[KRA03]: Kramer, R., Vieira, J. W., Khoury, H. J., Lima, F. R. A., & Fuelle, D. (2003). All about MAX: a male adult voxel phantom for Monte Carlo calculations in radiation protection dosimetry. Physics in Medicine & Biology, 48(10), 1239.

[KUH16]: Kuhnert, G., Boellaard, R., Sterzer, S., Kahraman, D., Scheffler, M., Wolf, J., ... & Kobe, C. (2016). Impact of PET/CT image reconstruction methods and liver uptake normalization strategies on quantitative image analysis. European journal of nuclear medicine and molecular imaging, 43, 249-258.

[KUH62]: Kuhl, D. (1962). Image separation radioisotope scanning. Radiology, 80 :2388–2392.

[LAV15]: S. Lavisse et al. “Optimized quantification of translocator protein radioligand 18F-DPA-714 uptake in the brain of genotyped healthy volunteers”. In: J. Nuc. Med. 56.7 (2015), pp. 1048–1054 (cit. on p. 20).

[LEE05]: Lee, C., Williams, J. L., Lee, C., & Bolch, W. E. (2005). The UF series of tomographic computational phantoms of pediatric patients. Medical physics, 32(12), 3537-3548.

[LEE06]: Lee, C., Lee, C., & Bolch, W. E. (2006). Age-dependent organ and effective dose coefficients for external photons: a comparison of stylized and voxel-based paediatric phantoms. Physics in Medicine & Biology, 51(18), 4663.

[LEE14]: Lee C. Monte carlo calculations in nuclear medicine second edition: Applications in diagnostic imaging. (2014): 431-432.

[MOR19]: Moreau, M. (2019). Introduction à l'imagerie par Tomographie d'Émission de Positons: définitions, approches de reconstruction et initiation aux isotopes complexes.

[MUZ12]: M. Muzi et al. “Quantitative assessment of dynamic PET imaging data in cancer imaging”. In: Magn. Resonance Imag. 30.9 (Nov. 2012), pp. 1203–1215

[NCR96]: NCRP, Dosimetry of X-Ray and Gamma-Ray Beams for Radiation Therapy in the Energy Range 10 keV to 50 MeV. National Council on Radiation Protection and Measurements Report, Bethesda, MD,

[NOZ15]: Nozawa, A., Rivandi, A. H., Kanematsu, M., Hoshi, H., Piccioni, D., Kesari, S., & Hoh, C. K. (2015). Glucose-corrected standardized uptake value in the differentiation of high-grade glioma versus post-treatment changes. Nuclear medicine communications, 36(6), 573.

[PAT85]: Patlak CS, Blasberg RG (1985) Graphical evaluation of blood-tobrain transfer constants from multiple-time uptake data. Generalizations. J Cereb Blood Flow Metab 5:584–590.

[PEA01]: Pearson, K. (1901). LIII. On lines and planes of closest fit to systems of points in space. The London, Edinburgh, and Dublin philosophical magazine and journal of science, 2(11), 559-572.

[PEA01]: Pearson, K. (1901). LIII. On lines and planes of closest fit to systems of points in space. The London, Edinburgh, and Dublin philosophical magazine and journal of science, 2(11), 559-572.

[PED94]: Pedersen, F., Bergströme, M., Bengtsson, E., & Långström, B. (1994). Principal component analysis of dynamic positron emission tomography images. European journal of nuclear medicine, 21(12), 1285-1292.

[PED94]: Pedersen, F., Bergströme, M., Bengtsson, E., & Långström, B. (1994). Principal component analysis of dynamic positron emission tomography images. European journal of nuclear medicine, 21(12), 1285-1292.

[PHE06]: Phelps, M., Cherry, S., and Dalhbom, M. (2006). PET : Physcis, instrumentation, and scanners. Springer Ed.

[PHE75]: Phelps, M., Hoffman, E., Mullani, N., and Ter Pogossian, M. (1975). Application of annihilation coincidence detection to transaxial reconstruction tomography. Journal of Nuclear Medicine, 16 :210–224.

[QIA11]: Qiao, H., & Bai, J. (2011, May). Dynamic simulation of FDG-PET image based on VHP datasets. In The 2011 IEEE/ICME International Conference on Complex Medical Engineering (pp. 154-158). IEEE.

[RAH09]: Rahmim, A., Tang, J., & Zaidi, H. (2009). Four-dimensional (4D) image reconstruction strategies in dynamic PET: beyond conventional independent frame reconstruction. Medical physics, 36(8), 3654-3670.

[REN02]: Renker, D. (2002). Properties of avalanche photodiodes for applications in high energy physics, astrophysics and medical imaging. Nuclear Instrumental Method, A486 :164–169.

[RUS13]: Rusten, E., Rødal, J., Bruland, Ø. S., & Malinen, E. (2013). Biologic targets identified from dynamic 18FDG-PET and implications for image-guided therapy. Acta Oncologica, 52(7), 1378-1383.

[SAM20]: Samimi, R., Kamali-Asl, A., Geramifar, P., van den Hoff, J., & Rahmim, A. (2020). Short-duration dynamic ^{18}F-FDG PET imaging: optimization and clinical application. Physica Medica, 80, 193-200.

[SCA04] : Scarmeas, N., Habeck, C. G., Zarahn, E., Anderson, K. E., Park, A., Hilton, J., Pelton, G. H., Tabert, M. H., Honig, L. S., Moeller, J. R., Devanand, D. P. & Stern, Y. (2004). Covariance PET patterns in early Alzheimer's disease and subjects with cognitive impairment but no dementia: utility in group discrimination and correlations with functional performance, NeuroImage 23(1): 35 – 45.

[SCH08]: Schaart, D., van Dam, H., Seifert, S., Vinke, R., P., D., Löhner, H., and Beekman, F. (2008). SiPM-array based PET detectors with depth-of-interaction correction. 2008 IEEE Nucl. Sci. Symp. Conf. Record., page 3581–3585.

[SEG01]: Segars, W. P. (2001). Development and application of the new dynamic NURBS-based cardiac-torso (NCAT) phantom. The University of North Carolina at Chapel Hill.

[SEG02]: Segars, W. P., & Tsui, B. M. (2002). Study of the efficacy of respiratory gating in myocardial SPECT using the new 4-D NCAT phantom. IEEE Transactions on Nuclear Science, 49(3), 675-679.

[SEG04]: Segars, W. P., Tsui, B. M., Frey, E. C., Johnson, G. A., & Berr, S. S. (2004). Development of a 4-D digital mouse phantom for molecular imaging research. Molecular Imaging & Biology, 6(3), 149-159.

[SEG09]: Segars WP, Sturgeon G, Mendonca S, Grimes J, Tsui BM. 4D XCAT phantom for multimodality imaging research. Medical physics. 2010 Sep;37(9):4902-15.

[SEG09]: Segars WP, Tsui BM. MCAT to XCAT: The evolution of 4-D computerized phantoms for imaging research. Proceedings of the IEEE. 2009 Nov 17;97(12):1954-68.

[SEG10]: Segars, W. P., Sturgeon, G., Mendonca, S., Grimes, J., & Tsui, B. M. (2010). 4D XCAT phantom for multimodality imaging research. Medical physics, 37(9), 4902-4915.

[SEG17]: Segars, W. P., Tsui, B. M., Cai, J., Yin, F. F., Fung, G. S., & Samei, E. (2017). Application of the 4-D XCAT phantoms in biomedical imaging and beyond. IEEE transactions on medical imaging, 37(3), 680-692.

[SHE17]: Shekari, M., Ghafarian, P., Ahangari, S., & Ay, M. R. (2017). Quantification of the impact of TOF and PSF on PET images using the noise-matching concept: clinical and phantom study. Nuclear Science and Techniques, 28, 1-8.

[SHE82] Shepp, L. A., & Vardi, Y. (1982). Maximum likelihood reconstruction for emission tomography. *IEEE Transactions on Medical Imaging*, 1(2), 113-122.

[STR11]: Strauss LG, Pan L, Cheng C, Haberkorn U, Dimitrakopoulou-Strauss A. Shortened acquisition protocols for the quantitative assessment of the 2-tissue-compartment model using dynamic PET/CT ^{18}F-FDG studies. J Nucl Med 2011;52:379–85.

[TAT03]: Tatsumi, M., Clark, P. A., Nakamoto, Y., & Wahl, R. L. (2003). Impact of body habitus on quantitative and qualitative image quality in whole-body FDG-PET. European journal of nuclear medicine and molecular imaging, 30, 40-45.

[THI03]: Thireou, T., Strauss, L. G., Dimitrakopoulou-Strauss, A., Kontaxakis, G., Pavlopoulos, S., & Santos, A. (2003). Performance evaluation of principal component analysis in dynamic FDG-PET studies of recurrent colorectal cancer. Computerized medical imaging and graphics, 27(1), 43-51.

[THI05]: Thireou T, Kontaxakis G, Strauss LG, et al: Feasibility study of the use of similarity maps in the evaluation of oncological dynamic positron emission tomography images. Med Biol Eng Comput 43:23-32, 2005.

[THI12] : Thielemans K, Tsoumpas C, Mustafovic S, Beisel T, Aguiar P, Dikaios N, Jacobson MW. STIR: software for tomographic image reconstruction release 2. Physics in Medicine & Biology. 2012 Jan 31;57(4):867.

[TOR00]: Torizuka, T., Nobezawa, S., Momiki, S., Kasamatsu, N., Kanno, T., Yoshikawa, E., ... & Ouchi, Y. (2000). Short dynamic FDG-PET imaging protocol for patients with lung cancer. European journal of nuclear medicine, 27(10), 1538-1542.

[VIJ15]: Vijayarajan, R., & Muttan, S. (2015). Discrete wavelet transform based principal component averaging fusion for medical images. AEU-International Journal of Electronics and Communications, 69(6), 896-902.

[VIS08] : Visser, E. P., Kienhorst, L. B., de Geus-Oei, L. F., & Oyen, W. J. (2008, October). Shortened dynamic FDG-PET protocol to determine the glucose metabolic rate in non-small cell lung carcinoma. In 2008 IEEE Nuclear Science Symposium Conference Record (pp. 4455-4458). IEEE.

[WIE02]: Wienhard K. (2002) Measurement of glucose consumption using [(18)F] fluorodeoxyglucose. Methods Methods, 27(3), 218-225.

[WU95]: Wu, H. M., Hoh, C. K., Choi, Y., Schelbert, H. R., Hawkins, R. A., Phelps, M. E., & Huang, S. C. (1995). Factor analysis for extraction of blood time-activity curves in dynamic FDG-PET studies. Journal of nuclear medicine: official publication, Society of Nuclear Medicine, 36(9), 1714-1722.

[WWW01]: http://www.ge.com.

[WWW02]: http://www.turkupetcentre.net/.

[WWW03]: https://stir.sourceforge.net/.

[XU00]: Xu, X. G., Chao, T. C., & Bozkurt, A. (2000). VIP-Man: an image-based whole-body adult male model constructed from color photographs of the Visible Human Project for multi-particle Monte Carlo calculations. Health Physics, 78(5), 476-486.

[XU05]: Xu, X. G., & Shi, C. (2005, April). Preliminary development of a 4D anatomical model for Monte Carlo simulations. In Monte Carlo 2005 Topical Meeting. The Monte Carlo method: versatility unbounded in a dynamic computing world [CD-ROM]. Chattanooga (TN): American Nuclear Society, LaGrange Park (IL).

[XU14]: Xu, X. G. (2014). An exponential growth of computational phantom research in radiation protection, imaging, and radiotherapy: a review of the fifty-year history. Physics in Medicine & Biology, 59(18), R233.

[YAO95]: Yao, W. J., Hoh, C. K., Hawkins, R. A., Glaspy, J. A., Weil, J. A., Lee, S. J., ... & Phelps, M. E. (1995). Quantitative PET imaging of bone marrow glucose metabolic response to hematopoietic cytokines. Journal of Nuclear Medicine, 36(5), 794-799.

[YOO] : Yoon, H. J., Jeong, Y. J., Son, H. J., Kang, D. Y., Hyun, K. Y., & Lee, M. K. (2015). Optimization of the spatial resolution for the GE discovery PET/CT 710 by using NEMA NU 2-2007 standards. Journal of the Korean Physical Society, 66, 287-294.

[ZEN10]: Zeng, G. L. (2010). *Medical Image Reconstruction: A Conceptual Tutorial*. Berlin: Springer.

[ZHA03]: Zhang, S. X., Liu, Z. J., & Tan, L. W. (2003). Dataset of first Chinese visible human female completed. Acta Academiae Medicinae Militaris Trertiae, 25(4), 371.

[ZHU18] : Zhu, B., Liu, J. Z., Cauley, S. F., Rosen, B. R., & Rosen, M. S. (2018). Image reconstruction by domain-transform manifold learning. *Nature*, 555(7697), 487-492.

[ZHU19] : Zhuang, M., Karakatsanis, N. A., Dierckx, R. A., & Zaidi, H. (2019). Impact of tissue classification in MRI-guided attenuation correction on whole-body Patlak PET/MRI. Molecular Imaging and Biology, 21(6), 1147-1156.

[ZUB92]: Zubal, I. G., & Harrell, C. R. (1992). Voxel based Monte Carlo calculations of nuclear medicine images and applied variance reduction techniques. Image and Vision Computing, 10(6), 342-348. 1996. 69.

[ZUE03]: Zuendorf, G., Kerrouche, N., Herholz, K., & Baron, J. C. (2003). Efficient principal component analysis for multivariate 3D voxel-based mapping of brain functional imaging data sets as applied to FDG-PET and normal aging. Human brain mapping, 18(1), 13-21.